Optical and structural properties of hematite for photoelectrochemical water splitting

By

Kelebogile Doreen Maabong

Submitted in partial fulfilment of the requirements for the degree of

DOCTOR OF PHILOSOPHY (PhD) IN PHYSICS

In the Faculty of Natural and Agricultural Sciences

University of Pretoria

Promoter: Prof Mmantsae M Diale

Co-promoter: Dr Augusto G. J Machatine

January 2018

Declaration

I, **Kelebogile Doreen Maabong**, declare that the thesis, which I hereby submit for the degree of Doctor of Philosophy in Physics at the University of Pretoria, is my own work and has not been previously submitted by me for a degree at this or any other tertiary institution.

Signature: …….

Date: …….

Optical and structural properties of hematite for photoelectrochemical water splitting

By

Kelebogile Doreen Maabong

Supervisors: Prof Mmantsae M. Diale & Dr. Augusto G.J Machatine

Abstract

The continuous energy and climate change issues has motivated the urgent need to explore and develop green and renewable energy technologies, worldwide. Photoelectrochemical (PEC) water splitting offers great potential to convert water into solar fuels using sunlight. Hematite is a prospective photoanode material for solar water oxidation half reaction because of its favorable optical energy band gap of 2.1 eV. However, its practical performance is greatly limited by low efficiencies, mainly due to rapid recombination of the photogenerated electron-hole pairs. To address the problem of high charge recombination, many research efforts have been adopted such as morphology control, doping and heterostructuring. Doping remains one of the effective strategies to suppress charge recombination through increasing conductivity and charge mobility. Among several investigated dopants, titanium substitution of Fe has been shown to effectively enhance the performance of hematite. In this study, we investigated Ti-doped hematite thin films prepared by a simple and cost effective chemical solution methods, varying the Ti concentration from 0.1 at% to 20 at%. A thin film photoanode produced by spin coating showed a significantly enhanced photoelectrochemical performance with increased photocurrent density and reduced current onset potentials compared to pristine hematite.

We also determined the effect of electrochemical oxidation (anodization) on microstructural properties at the surface of pristine hematite photoanode under PEC environment conditions. Anodization is considered an operational step in the functionality of a photoelectrochemical cell

and may have influence of functionality of the photoanode in a PEC cell. Hematite thin film were anodized at 500 and 700 mV *versus* Ag/AgCl in KOH under illumination, for various anodization times. XRD diffractometry revealed an increase in the average crystallite size upon anodization. Microscopic surface scanning analyses also revealed an increase in the average particle size at the surface upon anodization. The increased particle size, particularly at longer exposure times, could contribute to poor photoelectrochemical effect due to increased minority carrier diffusion distances. This dissertation is one of the first steps into an attempt to investigate the effect of anodization on the microstructural properties of hematite in a PEC cell, for solar energy conversion applications.

Dedication

To my dear husband

Lenna Tau

and

my son and my daughter(late)

Loago and Kaylar Tau

Acknowledgements

I would like to acknowledge the following people for their support and valuable contribution in the success of my study:

- My supervisor Prof Mmantsae M. Diale and co-supervisor Dr A. G. J. Machatine. The stimulating and critical discussions with my co-supervisor opened up many new aspects concerning the physics of semiconductor materials.
- Dr Artur Braun and his research team: Dr Debajeet Bora, Dr Rita Toth, Dr Yelin Hu and Dr Jianjun Wang. They supported this work on the experimental section as the experimental results presented and summarized here have been obtained at the Laboratory for High Performance Ceramics, Swiss Federal Laboratories for Materials Science and Technology, Empa, Dübendorf in Switzerland.
- Semiconductor research group for the support and encouragements.
- Physics Department staff and students for all their help, encouragement and moral support.
- Mrs Wiebke at Geology Department at XRD unit the technical staff at SEM unit for their training and guidance on the use of the respective equipment.
- University of Botswana, South African National Research Fund (NRF) and Swiss-South African Joint Research (SSAJR) Project IZLSZ2-149031 for financial support.
- My family: mostly my husband and my son, my parents, brothers and sisters, for the love and support throughout my studies.
- My friends for the support and encouragements.
- Lastly God Almighty for giving me the strength to pursue this study

List of abbreviations

PEC: Photoelectrochemical Cell

STH: Solar-to-Hydrogen

THF: Tetra Hydro Furan

FTO: Fluorine doped tin oxide

FESEM: Field Emission Scanning Electron Microscopy

RHE: Reversible Hydrogen Electrode.

AM 1.5: Air Mass

MoS_2: Molybdenum disulfide

Si: Silicon

TiO_2: Titanium oxide

SnO_2: Tin oxide

ZnO: Zinc oxide

$BiVO_4$: Bismuth vanadate

Cu_2O, Cupper (ii) oxide

CuO- Cupper oxide

$SrTiO_3$: Strontium titanate

TaON: Tantalum oxide

NiO: Nickel oxide

WO_3: Tungsten oxide

Cu_2S/CdS:

Cu(In, Ga)Se_2 (CIGS): copper indium gallium selenide

Ti: Titanium

Ge: Germanium

Al: Aluminium

Cr: Chromium

Mn: Manganese

α: absorption coefficient

E_g: optical energy band gap

List of Figures

List of Tables

Table of Contents

Chapter 1

Introduction

In view of global climate change and high energy demand, the worldwide quest for alternative clean and renewable energy sources has been stimulated [1]. Currently, the world relies primarily on burning coal, oil, and natural gas as conventional sources of energy, which are non-renewable resources and so are depleted with a much faster rate than new reserves are created. Besides, conventional sources are carbon-rich, and so their combustion leads to emission of greenhouse and toxic gases that contribute largely to global warming [2-4]. Unlike traditional sources, renewable resources are unlimited and economically, socially and environmentally sustainable. Among them, solar energy comprises the most abundant available primary energy resource, with the solar energy flux reaching the earth in the order of Terawatts (TW) [5, 6]. The critical technological challenge, however, lies in how this energy is harnessed and stored for future use.

The science and technology of solar cells have undergone revolutionary development since its discovery in 1954 [7]. Although the number of possible technologies and materials investigated is quite large, by far conventional silicon-based photovoltaic (PV) solar cells are the most dominant in solar technology owing to its excellent electronic properties [7]. However, due to a band gap of *ca.* 1.1 eV, most of the solar spectrum is not efficiently utilized as Si can only absorb in the far infrared region of the spectrum. In addition, energy storage in Si systems remains a challenge. In the course of developing new strategies capable of harnessing and storing a vast amount of solar radiation while controlling carbon emission, solar-driven splitting of water into solar fuels attracted

considerable attention as one of the attractive concepts to harvest sunlight and store energy in the form of chemical bonds, at minimal carbon emission [8, 9].

The photoelectrochemical (PEC) water splitting process utilizes synthetic photocatalytic compounds to mimic sunlight to generate hydrogen fuel from water, but the principle of energy conversion and storage is analogous to natural photosynthesis [9, 10]. Photoelectrochemical water splitting is an attractive process because of its potential high efficiency, up to 30% in principle, cost-effectiveness and environmental safety [11]. Semiconductors exhibit uniqueness to function as photocatalysts as these materials are capable of capturing sunlight, which generates charge carriers (electrons and holes) needed for the reactions to occur [12]. However, finding an ideal photocatalytic material that satisfies all specific physical requirements concerning semiconducting and electrochemical properties remain a challenge in this technology [8]. The majority of materials fail to fulfil the required combination of good absorption and stability [13]. Several materials, including MoS_2, TiO_2, ZnO, α-Fe_2O_3, $BiVO_4$, Cu_2O, $SrTiO_3$, TaON and WO_3 have been investigated [14-19]. Among them, α-Fe_2O_3, (hematite) emerged as a promising material owing to a combination of moderate bandgap (~ 2.1 eV) that can enable utilisation of most of the AM 1.5 global solar spectrum and outstanding stability in alkaline electrolytes under illumination and external bias [20, 21].

1.1 Motivation

Despite the attributes afore-mentioned, hematite is not yet an effective photoelectrode of photoelectrochemical water splitting due to rapid recombination of photogenerated electron-hole pairs [22]. Low electron mobility (10^{-2} $cm^2.V^{-1}.s^{-1}$), ultrashort hole diffusion length (2-4 nm), and extremely short excited lifetime (< 10ps) limit charge transportation and hole collection at the surface [8]. Also, despite the ideal bandgap, hematite absorbs poorly in the visible range of the

solar spectrum. Indeed, research efforts to alleviate the shortcomings have been in place including optimization of nanostructured morphologies of hematite to improve charge transport and collection efficiency, leading to significant progress in terms of enhancement in photocurrent. Despite the efforts, little attention has been given to the impact of electrochemical processes taking place under PEC environment on the surface of hematite photoanode in a PEC cell. The migration of ions during the reactions may alter properties of the photoelectrode at and near the surface, influencing the overall PEC performance of the electrode [12]. It is noted that the functionality of the photoelectrode material in contact with alkaline electrolyte depends profoundly on the surface and bulk properties, for solar energy conversion applications [23].

While detailed research on the effect of electrochemical oxidation (anodization) on the electronic properties of the hematite photoanode at the surface under PEC condition is available in literature [23-26], no experimental information exists on the effect of the anodizing conditions on the microstructural properties at the hematite surface in a PEC cell. Gajda-Schrantz e*t al.* reported ionization of Fe^{2+} states to Fe^{3+} at the hematite surface upon anodization [26]. They also suggested the formation of new electronic states upon anodization, suggestive of hole doping upon anodization. In another study, Braun *et al.* presumed that "with continuous exposure of hematite to anodizing potentials in PEC environment conditions, the newly created states may be preserved in the form of a thin film, the depth of which scaling with the exposure (anodization) time" [23, 26]. The findings of those studies suggested that not only the electronic structure at the surface, but also the microstructural properties may be altered upon anodization. Microstructural features of the photoelectrode such as crystallinity, surface defects, particle size, morphology, film thickness and texture have a detrimental effect on the functionality of photoelectrode in a PEC cell

[27, 28]. Thus, it is imperative to understand the effect of anodization on the surface of hematite under PEC environment conditions.

On the other hand, even though hematite is known as an n-type semiconductor due to naturally occurring oxygen vacancies in the bulk [29], its use in solar energy conversion application is adversely affected by its high intrinsic resistance (~10^5-10^6 Ω.cm) [30]. Charge transport and collection are hampered by rapid charge recombination (in the material and on the surface) which is one of the major obstacles for achieving the required efficiency for an efficient solar energy conversion device. One of many possible solutions to reduce recombination is elemental doping.

N-type doping with Ti [30, 31], Ge [32], Si [33, 34] and Zr [29] have been found attractive, demonstrating a similar effect of altering conductivity through increased carrier concentration. *Ab* initio calculations suggest that Zr, Si and Ge perform superior than Ti especially at low concentration levels [29]. The authors attributed the differing performance to the bonding nature of the dopants with oxygen. Ti-O make ionic bonds and thus the extra provided electron may localize on Ti in its empty 3d orbital, whereas in Si/Ge-O which makes strong covalent bonds of Si/Ge-O the electron would be forced to reside in the antibonding orbital which is strongly unfavorable, leading to the electron preferring to occupy Fe ion [29]. However, experimentally, Zhang *et al*. reported enhanced PEC activity with Ti and Si doping prepared by spray pyrolysis, with Ti being superior to Si [35]. Glasscock *et al*. also made similar observations with Ti and Si-doped hematite nanostructures prepared by reactive magnetron sputtering [36]. This information suggests that Ti should be pursued further for photoelectrode production in solar energy conversion applications, especially at high doping concentration levels which result in the formation of titanate phases such as Fe_2TiO_3 or Fe_2TiO_5 [37]. The formation of titanate phases on the surface of hematite is beneficial in increasing PEC performance of Ti-doped hematite photoanodes by enhancing

charge transport, charge transfer and optical absorption of hematite [38]. Besides, a predominant experimental suggestion is that dopants have similar electronic effects with the level of doping more critical than the dopant identity [30]. Liao *et al*. noted the solubility of Si in hematite as low as ~ 2.5 atomic percentage (at%) as compared to Ti which can be added continuously until titanate phases are formed [29].

While various techniques such as pulse laser deposition (PLD), hydrothermal, atomic layer deposition (ALD), dip coating, spray pyrolysis, reactive magnetron sputtering, in situ solid-state reaction method have been employed to establish a Ti-doped hematite film [30, 39-44], spin coating and dip coating methods have not been explored in depth. Furthermore, we note that the optimal doping level of Ti remains an open question. The reported results show dependence on material properties which in turn are greatly influenced by the synthetic procedure as demonstrated in Table 1.1. In this study, the effect of Ti doping to enhance the PEC performance of hematite grown by spin coating is reported. A comparison of photocurrent density of Ti-doped hematite photoanodes established by various synthetic methods is presented in Table 1.1 along with the one obtained during this study.

Table 1-1: A comparison of photocurrent density of Ti-doped hematite photoanodes prepared by various experimental techniques.

Synthesis method	Photocurrent density @1.23 V vs RHE (mA/cm^2)	Reference
Hydrothermal	1.91	Deng *et al.* [39]
Hydrothermal	1.58	Lv *et al.* [45]
Hydrothermal	1.4	Bassi *et al.* [46]
Atomic layer deposition	< 0.4	Zandi *et al.* [13]
Pulse laser deposition	1.64	Atabaev *et al.* [40]
Spray pyrolysis	1.3	Kumari *et al.* [47]
Ultrasonic spray pyrolysis	0.45	Zhang *et al.* [35]
Magnetron sputtering	< 0.2	Glasscock *et al.* [36]
Electrodeposition	1.5	Xie *et al.* [31]
Electrodeposition	1.5	Mirbagheri *et al.* [48]
Electrodeposition	1.0	Qui *et al.* [49]
In situ solid-state reaction	1.2	Miao *et al.* [43]
Dip coating	0.72	Maabong *et al.* [50], this study
Spin coating	1.84	This study

1.2 Research Objectives

The objectives of this thesis are twofold: firstly, to investigate the effect of electrochemical oxidation (anodization) on the microstructural features of hematite photoanode under photoelectrochemical water splitting environment conditions. For this, hematite thin films prepared by dip coating were anodized at 500 mV and 700 mV versus Ag/AgCl in KOH. X-ray diffraction (XRD), scanning electron microscopy (SEM), Raman and atomic force microscopy (AFM) were employed to analyse the surface morphology and crystallographic properties of hematite thin films after exposure to PEC environment and compared with the pristine hematite

film. The influence of exposure (anodization) time on the surface modifications observed on hematite upon anodization was also investigated. The findings of this work might provide a new set of information in addressing issues of poor PEC performance of hematite photoanode in a PEC solar cell.

Secondly, to use a simple, cost-effective and reproducible technique to synthesize Ti-doped hematite photoanodes and test those for photoelectrochemical water splitting application. Spin coating and dip coating techniques were used for the synthesis of samples. XRD, SEM, Raman and AFM were used to analyse surface morphology and crystallographic properties of the prepared Ti-doped hematite thin films and compared with the pure hematite films. Electrochemical impedance (EIS) and photoluminescence (PL) were used to understand the effect of doping on charge carrier transportation and transfer in the fabricated photoanodes.

1.3 Thesis layout

This thesis is further organized as follows:

Chapter 2 presents the theoretical aspects of the basic principles of photoelectrochemical water splitting with particular emphasis on α-Fe_2O_3, on which this study is based. The properties, application and challenges of hematite as the photoanode in PEC water splitting are also discussed.

Chapter 3 describes the experimental techniques employed to synthesize and characterize the samples used for the study. The structural and optoelectronic properties of the film were studied with SEM, AFM, XRD, Raman spectroscopy, ultraviolet/visible (UV/Vis) spectroscopy and electronic impedance spectroscopy (EIS).

Chapter 4 consists of 2 parts, discussing the results obtained during this study. The chapter focuses on the effect of electrochemical oxidation (anodization) on the microstructural properties

at the hematite surface under PEC conditions. The role of anodization time is also considered. The results presented in this chapter have been published in peer review journals.

Chapter 5 consists of 2 parts discussing PEC activity of nanostructured Ti-doped hematite photoanodes prepared by sol-gel methods and their photoelectrochemical water oxidation performance. The results presented in this chapter have been published in peer review journals and also developed as a manuscript for publication.

Chapter 6 summarizes the conclusions drawn from the study and proposes further research to be performed.

References

[1] Z. Liu, K. Wang, L. Xiao, X. Chen, X. Ren, J. Lu, L. Zhuang, A morphology effect of hematite photoanode for photoelectrochemical water oxidation, RSC Advances, 4 (2014) 37701.

[2] N. Chouhan, R.-S. Liu, J. Zhang, Photochemical Water Splitting: Materials and Applications, CRC Press2017.

[3] V.C. Nelson, K.L. Starcher, Introduction to renewable energy, CRC press2015.

[4] C. Rühl, P. Appleby, J. Fennema, A. Naumov, M. Schaffer, Economic development and the demand for energy: A historical perspective on the next 20 years, Energy Policy, 50 (2012) 109-116.

[5] D.A. Wheeler, G. Wang, Y. Ling, Y. Li, J.Z. Zhng, Nanostructured hematite: synthesis, characterization, charge carrier dynamics, and photoelectrochemical properties, Energy Environ. Sci., 5 (2012) 6682–6702.

[6] B. Klahr, S. Gimenez, F. Fabregat-Santiago, J. Bisquert, T.W. Hamann, Electrochemical and photoelectrochemical investigation of water oxidation with hematite electrodes, Energy & Environmental Science, 5 (2012) 7626.

[7] K. Chopra, P. Paulson, V. Dutta, Thin-film solar cells: an overview, Progress in Photovoltaics: Research and Applications, 12 (2004) 69-92.

[8] R.v.d. Krol, M. Gra¨tzel, Photoelectrochemical Hydrogen Production, Springer,, London New York, 2012.

[9] M. Grätzel, Photoelectrochemical cells, Nature, 414 (2001) 338-344.

[10] Z. Lin, J. Wang, Low-cost nanomaterials toward greener and more efficient energy applications, Springer, Verlag London, 2014.

[11] J.Z. Zhang, Metal oxide nanomaterials for solar hydrogen generation from photoelectrochemical water splitting, MRS Bulletin 336 (2011) 48-55.

[12] J. Joy, J. Mathew, S.C. George, Nanomaterials for photoelectrochemical water splitting–review, International Journal of Hydrogen Energy, DOI (2018).

[13] O. Zandi, B.M. Klahr, T.W. Hamann, Highly photoactive Ti-doped α-Fe2O3 thin film electrodes: resurrection of the dead layer, Energy & Environmental Science, 6 (2013) 634-642.

[14] K. Ding, B. Chen, Y. Li, Y. Zhang, Z. Chen, Comparative density functional theory study on the electronic and optical properties of BiMO4 (M = V, Nb, Ta), Journal of Materials Chemistry A, 2 (2014) 8294-8303.

[15] S. Chen, L.-W. Wang, Thermodynamic Oxidation and Reduction Potentials of Photocatalytic Semiconductors in Aqueous Solution, Chemistry of Materials, 24 (2012) 3659-3666.

[16] J. Pan, Z. Wang, Q. Chen, J. Hu, J. Wang, Band structure engineering of monolayer MoS2 by surface ligand functionalization for enhanced photoelectrochemical hydrogen production activity, Nanoscale, 6 (2014) 13565-13571.

[17] A. Paracchino, V. Laporte, K. Sivula, M. Grätzel, E. Thimsen, Highly active oxide photocathode for photoelectrochemical water reduction, Nature Materials, 10 (2011) 456.

[18] D.K. Bora, The photocathodic behavior of hierarchical ZnO/hematite hetero nanoarchitectures, Journal of Materials Research, 31 (2016) 1554-1564.

[19] P. Dias, T. Lopes, L. Meda, L. Andrade, A. Mendes, Photoelectrochemical water splitting using WO3 photoanodes: the substrate and temperature roles, Physical Chemistry Chemical Physics, 18 (2016) 5232-5243.

[20] D.K. Bora, A. Braun, E.C. Constable, “In rust we trust”. Hematite – the prospective inorganic backbone for artificial photosynthesis, Energy Environ. Sci., 6 (2013) 407-425.

[21] M.J. Katz, S.C. Riha, N.C. Jeong, A.B.F. Martinson, O.K. Farha, J.T. Hupp, Toward solar fuels Water splitting with sunlight and rust, Coordination Chemistry Reviews 256 (2012) 2521-2529.

[22] Y. Lin, G. Yuan, S. Sheehan, S. Zhou, D. Wang, Hematite-based solar water splitting: challenges and opportunities, Energy & Environmental Science, 4 (2011) 4862.

[23] A. Braun, Q. Chen, D. Flak, G. Fortunato, K. Gajda-Schrantz, M. Grätzel, T. Graule, J. Guo, T.W. Huang, Z. Liu, Iron resonant photoemission spectroscopy on anodized hematite points to electron hole doping during anodization, ChemPhysChem, 13 (2012) 2937-2944.

[24] A. Braun, K. Sivula, D.K. Bora, J. Zhu, L. Zhang, M. Grätzel, J. Guo, E.C. Constable, Direct Observation of Two Electron Holes in a Hematite Photoanode during Photoelectrochemical Water Splitting, The Journal of Physical Chemistry C, 116 (2012) 16870-16875.

[25] D.K. Bora, A. Braun, S. Erat, A.K. Ariffin, R. Löhnert, K. Sivula, J.r. Töpfer, M. Grätzel, R. Manzke, T. Graule, Evolution of an oxygen near-edge X-ray absorption fine structure transition in the upper Hubbard band in α-Fe2O3 upon electrochemical oxidation, The Journal of Physical Chemistry C, 115 (2011) 5619-5625.

[26] K. Gajda-Schrantz, S. Tymen, F. Boudoire, R. Toth, D.K. Bora, W. Calvet, M. Gratzel, E.C. Constable, A. Braun, Formation of an electron hole doped film in the alpha-Fe2O3 photoanode upon electrochemical oxidation, Phys Chem Chem Phys, 15 (2013) 1443-1451.

[27] M. Sugiyama, K. Fujii, S. Nakamura, Solar to Chemical Energy Conversion: Theory and Application, Springer2016.

[28] S. Heiroth, R. Frison, J.L. Rupp, T. Lippert, E.J.B. Meier, E.M. Gubler, M. Döbeli, K. Conder, A. Wokaun, L.J. Gauckler, Crystallization and grain growth characteristics of yttria-stabilized zirconia thin films grown by pulsed laser deposition, Solid State Ionics, 191 (2011) 12-23.

[29] P. Liao, M.C. Toroker, E.A. Carter, Electron transport in pure and doped hematite, Nano letters, 11 (2011) 1775-1781.

[30] S. Chatman, C.I. Pearce, R.K. M., Charge Transport at Ti-Doped Hematite (001)-Aqueous Interfaces, Chemistry of Materials, 27 (2015) 1665−1673.

[31] X. Xie, K. Li, W.-D. Zhang, Photoelectrochemical properties of Ti-doped hematite nanosheet arrays decorated with CdS nanoparticles, RSC Advances, 6 (2016) 74234-74240.

[32] S. Li, J. Cai, Y. Mei, Y. Ren, G. Qin, Thermal oxidation preparation of doped hematite thin films for photoelectrochemical water splitting, International Journal of Photoenergy, 2014 (2014).

[33] D.K. Bora, Fabrication of silicon doped hematite photoelectrode with enhanced photocurrent density via solution processing of an in-situ TEOS modified precursor, Materials Science in Semiconductor Processing, 31 (2015) 728-738.

[34] I. Cesar, K. Sivula, A. Kay, R. Zboril, M. Grätzel, Influence of feature size, film thickness, and silicon doping on the performance of nanostructured hematite photoanodes for solar water splitting, The Journal of Physical Chemistry C, 113 (2008) 772-782.

[35] M. Zhang, W. Luo, Z. Li, T. Yu, Z. Zou, Improved photoelectrochemical responses of Si and Ti codoped α-Fe 2 O 3 photoanode films, Applied Physics Letters, 97 (2010) 042105.

[36] J.A. Glasscock, P.R.F. Barnes, I.C. Plumb, N. Savvides, Enhancement of Photoelectrochemical Hydrogen Production from Hematite Thin Films by the Introduction of Ti and Si, The Journal of Physical Chemistry C, 111 (2007) 16477-16488.

[37] P.S. Bassi, R.P. Antony, P.P. Boix, Y. Fang, J. Barber, L.H. Wong, Crystalline Fe2O3/Fe2TiO5 heterojunction nanorods with efficient charge separation and hole injection as photoanode for solar water oxidation, Nano Energy, 22 (2016) 310-318.

[38] J. Deng, X. Lv, J. Liu, H. Zhang, K. Nie, C. Hong, J. Wang, X. Sun, J. Zhong, S.-T. Lee, Thin-Layer Fe2TiO5 on Hematite for Efficient Solar Water Oxidation, ACS Nano, 9 (2015) 5348-5356.

[39] J. Deng, J. Zhong, A. Pu, D. Zhang, M. Li, X. Sun, S.-T. Lee, Ti-doped hematite nanostructures for solar water splitting with high efficiency, J. Appl. Phys., 112 (2012) 084312.

[40] T.S. Atabaev, N.H. Hong, Y.-H. Hwang, M. Ajmal, H.-K. Kim, Ti-doped hematite thin films for efficient water splitting, Appl. Phys. A 118 (2015) 1539-1542.

[41] J.A. Glasscock, P.R. Barnes, I.C. Plumb, N. Savvides, Enhancement of photoelectrochemical hydrogen production from hematite thin films by the introduction of Ti and Si, The Journal of Physical Chemistry C, 111 (2007) 16477-16488.

[42] C.J. Sartoretti, M. Ulmann, B. Alexander, J. Augustynski, A. Weidenkaff, Photoelectrochemical oxidation of water at transparent ferric oxide film electrodes, Chemical Physics Letters, 376 (2003) 194-200.

[43] C. Miao, T. Shi, G. Xu, S. Ji, C. Ye, Photocurrent enhancement for Ti-doped Fe2O3 thin film photoanodes by an in situ solid-state reaction method, ACS applied materials & interfaces, 5 (2013) 1310-1316.

[44] O. Zandi, T.W. Hamann, The potential versus current state of water splitting with hematite, Physical Chemistry Chemical Physics, 17 (2015) 22485-22503.

[45] X. Lv, K. Nie, H. Lan, X. Li, Y. Li, X. Sun, J. Zhong, S.-T. Lee, Fe2TiO5-incorporated hematite with surface P-modification for high-efficiency solar water splitting, Nano Energy, 32 (2017) 526-532.

[46] P.S. Bassi, S.Y. Chiam, Gurudayal, J. Barber, L.H. Wong, Hydrothermal Grown Nanoporous Iron Based Titanate, Fe2TiO5 for Light Driven Water Splitting, ACS Applied Materials & Interfaces, 6 (2014) 22490-22495.

[47] S. Kumari, A.P. Singh, Sonal, D. Deva, R. Shrivastav, S. Dass, V.R. Satsangi, Spray pyrolytically deposited nanoporous Ti4+ doped hematite thin films for efficient photoelectrochemical splitting of water, Int. J. Hydrogen Energy, 35 (2010) 3985-3990.

[48] N. Mirbagheri, D. Wang, C. Peng, J. Wang, Q. Huang, C. Fan, E.E. Ferapontova, Visible Light Driven Photoelectrochemical Water Oxidation by Zn- and Ti-Doped Hematite Nanostructures, ACS Catalysis, 4 (2014) 2006-2015.

[49] W. Qiu, Y. Huang, B. Long, H. Li, Y. Tong, H. Ji, Enhanced Photoelectrochemical Oxygen Evolution Reaction Ability of Iron-Derived Hematite Photoanode with Titanium Modification, Chemistry–A European Journal, 21 (2015) 19250-19256.

[50] K. Maabong, A.G.J. Machatine, B.S. Mwankemwa, A. Braun, D.K. Bora, R. Toth, M. Diale, Nanostructured hematite thin films for photoelectrochemical water splitting, Physica B: Condensed Matter, 535 (2018) 67-71.

Chapter 2

Theoretical aspects of photoelctrochemical water splitting

2.1 Introduction

Hydrogen is considered one of the most attractive fuels of the future due to its high energy content per unit mass (120 J/g) compared to gasoline [1]. Its environmental friendliness has continued to stimulate interest in research and development in energy generation, storage, and usage. So far, the leading technology for hydrogen generation has been through steam reforming from fossil fuels such as natural gas. Consequently, these technologies lead to the emission of CO_2, contributing to global warming. On the other hand, hydrogen generation based on renewable energy is considered a non-polluting process. Photoelectrochemical water splitting is attractive because of its potential high efficiency, up to 30% in principle, cost-effectiveness and being environmentally benign [1].

2.2 The working principle

The basic principle behind PEC water splitting is the conversion of solar energy to molecular hydrogen by applying an external bias on to a photocatalytic material immersed in an electrolyte which contains a redox couple, exposed to sunlight and able to absorb light. Semiconductors exhibit uniqueness to function as photocatalysts as these materials are capable of capturing sunlight, which generates charge carriers (electrons and holes) for the reactions to occur [2]. A typical PEC system is illustrated in Figure 2-1. The platinum (Pt) metal is usually used as the counter electrode because it exhibits good catalytic activities towards the hydrogen evolution reaction [3]. The redox aqueous electrolyte regenerates the photoactive components of the electrodes. When placed in contact with the electrolyte, the electrons migrate from the semiconductor to the solution to equilibrate the electronic potential of the semiconductor with the

chemical potential of the electrolyte, inducing the formation of a space charge layer at the interface. The diffusion of electrons results in band bending in the semiconductor which facilitates charge separation in the space charge layer [4].

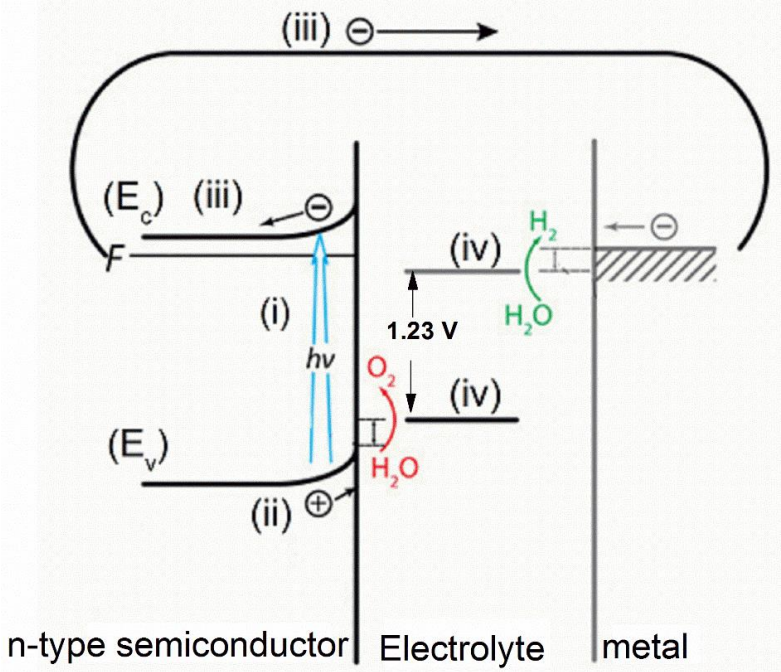

Figure 2-1: A simple schematic representation of n-type semiconductor-based solar photoelectrochemical water splitting process. Several essential steps involved in the process are illustrated; (i) light absorption, (ii) charge generation, (iii) charge transport and, (iv) surface chemical reactions. Redrawn from Ref. [5].

Upon illumination of the semiconductor with the global standard one sun spectral irradiance (AM 1.5 G, 100 mW/cm^2), the electrons are excited from the valence band to the conduction band, generating separable electron-hole pairs within the material. The photogenerated electron-hole pairs separated under the electric field in the space charge region. The photo holes migrate to the semiconductor-electrolyte interface to oxidize water into oxygen and protons according to Eq. 1.1a. Subsequently, the electrons diffuse to the cathode through an external circuit and react with protons to generate hydrogen as defined by Eq. 1.1b [6-8];

$$2H_2O + 4h^+ \rightarrow 4H^+ + O_2 \qquad E^0_{ox} = -1.23V \tag{1.1a}$$

$$4H^+ + 4e^- \rightarrow 2H_2 \qquad E^0_{red} = 0V \tag{1.1b}$$

Ideally, a minimum potential of 1.23 V is needed to drive chemical reactions. However, taking into consideration thermodynamic losses from the device and overpotentials required at various points in the system, the optimal energy required for water splitting is around 2.0 eV [8]. The most common parameter to evaluate the PEC water spitting performance of the photoelectrode is the photocurrent density directly corresponding to water oxidation, obtained under illumination at the minimum water splitting potential, 1.23 V measured against the reversible hydrogen electron (RHE) [8, 9]. The more photocurrent density (water oxidation) achieved, the more hydrogen fuel produced.

There are few physical requirements that the photoelectrode material must fulfil to attain efficient water splitting; (i) proper absorption in the visible region of the solar spectrum, (ii) efficient charge transport, (iii) high stability (aqueous and thermal) (iv) band edge positions straddling water oxidation and reduction potential levels and (v) be cost-effective and environmental benign [8, 9]. The overall solar-to-hydrogen (STH) efficiency and performance of the PEC water splitting process depend fundamentally on the efficiencies of (i) light absorption, (ii) charge generation and separation, (iii) charge transport and (iv) charge collection and transfer (reactions). The STH efficiency profoundly depends on the optoelectronic properties such as charge transport, mobility, conductivity and absorption of the photoanode material. The photoanode material in turn depends on the structural features like morphology, crystal size, shape, crystallinity and exposed crystallographic facets. These properties are determined by the synthesis procedure [1, 2, 10-13].

2.3 Semiconductor photoelectrodes

The first solar photoelectrochemical cell using a semiconductor material was developed by Fujishima and Honda in 1972, using titanium dioxide (TiO_2) [14]. Despite good charge transport properties, TiO_2 yielded low solar conversion efficiency mainly due to a large band gap of about 3.2 eV which respond only to the shortest wavelength in the ultraviolet (UV) light ($\lambda \leq 400$ nm) region [15]. UV light makes up less than 5% of the solar spectrum. Since then, a lot of research has been devoted to the development and design of alternative catalyst material with a broad spectral response throughout the visible range to improve hydrogen production efficiency. Various semiconductor materials including, MoS_2, TiO_2, SnO_2, ZnO, α-Fe_2O_3, $BiVO_4$, Cu_2O, CuO, $SrTiO_3$, TaON, NiO, WO_3 have been investigated [16-21]. However, finding an ideal sustainable material that satisfies all the physical requirements remains a significant challenge in solar fuel technology.

Figure 2-2 shows a schematic representation of band edges for some of the investigated semiconductors used in water reduction and oxidation potential levels as compared to those in an ideal photocatalyst for PEC water splitting [22]. It is quite clear from the figure that few materials fulfil the requirement of band edge positions relative to water reduction and oxidation potential levels. This common limitation can be overcome with the help of application of external bias in addition to illumination to assist the required reactions at the surface to occur. Besides, the majority of materials fail to fulfil the necessary combination of proper absorption and stability [23]. Materials such as TiO_2, SnO_2 and ZnO offer excellent durability in contact with aqueous solutions. However, these materials exhibit large band gaps (≥ 3 eV) that absorb UV and thus render them ineffective as practical water-splitting catalysts. On the other hand, the usefulness of narrow bandgap semiconductors such as WO_3, Cu_2O, TaON, $BiVO_4$ is limited by significant cathodic and anodic corrosion under aqueous environment [1]. Hematite (α-Fe_2O_3) is, in many respects, a

prospective photoanode material for water oxidation half-reaction of the water splitting process owing to a combination of outstanding electrochemical stability, a favorable energy band that enables sufficient visible light absorption and optimum valence band edge for water oxidation [24-32].

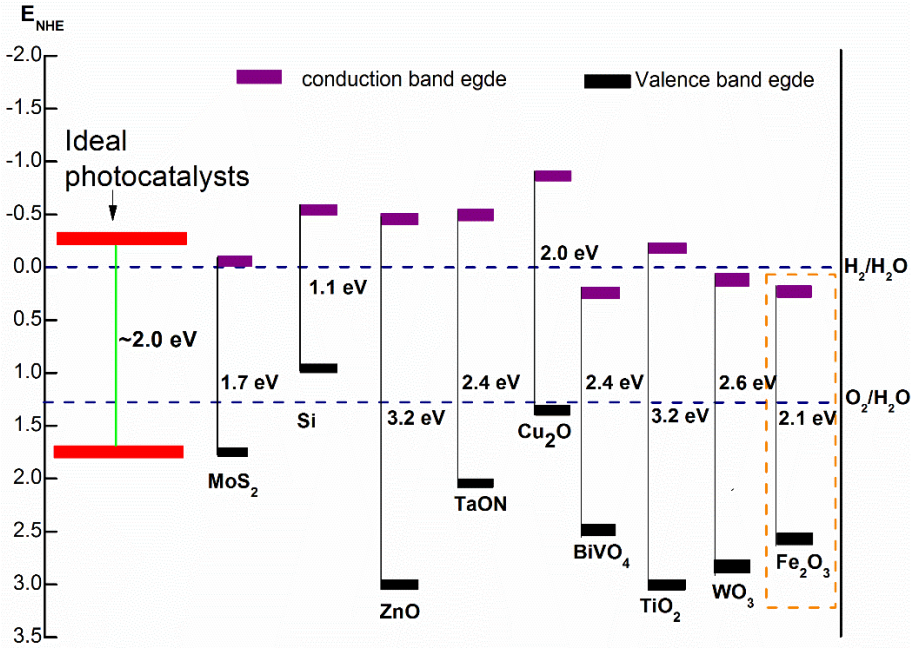

Figure 2-2: Schematic representation of band edge positions with respect to water reduction and oxidation potentials for various semiconductor materials. Bands for an ideal photocatalyst are also shown for reference. Adapted from Ref. [22].

2.4 Hematite as a promising photoelectrode

Hematite belongs to transition metal oxides (TMOs), a class of materials which find use in various scientific and nanotechnological applications owing to their ability to exist in several different valence states. Iron oxide is one of the most abundant TMOs in nature [33]. Among the most known iron oxides: iron (II) oxide (FeO), iron (III) oxide (Fe_2O_3), magnetite (Fe_3O_4); Fe_2O_3 is the most common, obtained in three polymorphs; α-, β-, and ϒ-Fe2O3. α-Fe_2O_3 (hematite) is the most thermodynamically stable polymorph of iron (iii) oxides in ambient conditions [34, 35]. From the

crystallographic point of view, hematite is isostructural with α-Al_2O_3, a corundum structure with trigonal symmetry and space group D_{3d}^6 $(R\bar{3}c)$ [36]. The structure is composed of two formulae units in the primitive rhombohedral unit cell, turned 180 ° to each other with respect to the z-axis [37]. The lattice constants of the rhombohedral unit cell are a = b = 5.032, c = 13.733; and an angle between vectors of α = 55.195°. The lattice is built on a slightly distorted framework of the hexagonal close-packed system with the O^{-2} anions occupying 2/3 of close-packed sites, and the metal cations fit into octahedral sites. The Fe atoms are ferromagnetically coupled within layers between hexagonally stacked close-packed oxygen planes and coupled anti-ferromagnetically between layers by a superexchange interaction, oriented perpendicular to the three-fold *c*-axis. [38].

2.4.1 Properties of hematite for water splitting

Hematite is a narrow bandgap n-type semiconductor. The energy band gap of ~ 2.1 eV is expected to allow absorption of ~ 40% of the visible light, leading to a maximum theoretical solar to hydrogen (STH) efficiency of about 13 % (i.e., 12.5 mA cm^{-2} at 1.23 V vs RHE) under AM 1.5 illumination [15, 39, 40]. In addition, α-Fe_2O_3 exhibits excellent electrochemical stability in alkaline solutions, under illumination and external bias. Hematite also exhibits a valence band edge thermodynamically favorable for water oxidation half reaction. It is inexpensive, abundant and non-toxic. All these attributes present hematite as a promising photoanode material for solar fuel production from direct solar water splitting. Experimentally, hematite can be synthesized with various techniques, including atomic layer deposition, hydrothermal, chemical vapor deposition (CVD), electrodeposition, pulse laser deposition, spray pyrolysis, molecular epitaxy, dip coating, spin coating and sputtering, on a wide range of support surfaces [38, 41-45]. Chemical solution-based deposition techniques are inexpensive and require low deposition temperatures. They also

provide precise control over deposition parameters. Though these methods produce thin film electrodes of lower quality than those prepared by sophisticated techniques (e.g., sputtering), the low cost and accessibility of these techniques make them attractive for solar energy conversion applications.

2.4.2 Challenges for solar water splitting with hematite

Despite the attractive characteristics aforementioned, hematite is not yet an effective material for water splitting to solar fuel. Its full capacity is adversely affected by intrinsic deficiencies. The slow oxygen evolution reaction kinetics at the surface is one of the major drawbacks. The slow water oxidation kinetics is a consequence of many factors including short hole diffusion distance (2-4 nm) compared to the long photon penetration depth of ~118 nm at 550 nm [8]. The majority of photons penetrate deeper, resulting in most of the electron-hole pairs being photogenerated out of the space charge region where they can be efficiently separated and driven towards the corresponding electrodes. Practically, only those holes that are generated within a few to several nanometers of the semiconductor/solution interface can reach the interface and be used for water oxidation, while the rest recombine with electrons and generate heat [46]. Other factors include short excited-state lifetime (< 10ps), poor electron conductivity and low charge carrier mobility ($0.1\text{-}10^{-2}$ $cm^2.V^{-1}.s^{-1}$) [3, 10, 47-52]. Collectively, these factors lead to rapid charge recombination which is one of the major obstacles limiting delivery of the photogenerated holes to the semiconductor/electrolyte interface for the required water oxidation reaction.

Another problem is that hematite exhibit a very low absorption coefficient [8]. Due to an indirect energy gap, where the band extrema occur at different momenta in the crystal Brillouin zone, absorption of the majority of photons is via phonon-assisted transitions [8]. The practical consequence is that the hematite electrode requires a thickness of a few hundred microns (μm) for

efficient absorption. As the photons have extended absorption depth, most charges are photogenerated outside the space charge region and travel long distances traversing through the material and eventually recombine with electrons. Moreover, as seen from Figure 2-2, the conduction band edge is thermodynamically unfavorable for unassisted water reduction, falling a few hundred millivolts short of what is required to drive the reduction of water to hydrogen. Potentials of over 1 V *versus* RHE are necessary to drive water splitting reactions.

Various strategies have been in place tackling the shortcomings such as morphology control or nanostructuring, doping and utilization of ultrathin electrodes etc., leading to significant progress in terms of water oxidation photocurrent as well as reduction of overpotentials [12, 47-52]. Recently, the coupling of hematite with binary and ternary metal oxides including WO_3/Fe_2O_3, Fe_2O_3/Cu_2O, Fe_2O_3/TiO_2, Fe_2O_3/Fe_2TiO_5 with n/n heterojunctions have sparked new interest to improve charge transport and collection at the hematite-solution interface [53-55]. Such material combinations can increase the efficiency in numerous ways such as by enhanced charge separation, charge transport and faster surface kinetics, prolonged carrier lifetime and modification of the electronic properties of the interface between both materials [53-55].

A combination of nanostructuring and elemental doping seems particularly attractive as a sustainable approach to modify surface and bulk properties of materials, which are not necessarily the same. Compared to bulk materials, nanomaterials provide minimized diffusion distances for the photogenerated charge carriers, which could facilitate efficient transport and charge separation at the surface. Also, the large interfacial contact area due to the increased surface area to volume ratio between the photoanode and the electrolyte facilitates charge transfer, thereby enabling high efficiencies [2, 11]. Most importantly, the quantum size confinement in nanomaterials can potentially be used to manipulate the bandgap energy of the semiconductor [56]. High efficiencies

have been achieved for nanostructured hematite electrodes of different nanoarchitecture such as worm-like nanostructures [57], nanosheets [58] and nanorods [59]. The detailed comparison of the features of different hematite nanostructures is given in Ref. [11].

On the other hand, elemental doping can alter electronic properties in numerous ways including by increasing charge density (electrons in the case of photoanode), leading to improved electron conductivity which determines the probability of photogenerated electrons-holes pairs inside the electrode moving to the surface [60, 61]. Other effects include reduced width of the space charge layer at the surface, reduced electron effective mass, prolonged charge carrier lifetime and increased electric field and degree of band bending in the space charge layer [1, 12, 62-66]. Depending upon the degree of doping and nanostructuring, and the magnitude of the applied anodic bias, the space charge layer can extend up to 10's of nanometers into the bulk of hematite films, enabling separation of a substantial number of photogenerated carriers to participate in water splitting reactions [67]. These doping-induced effects synergistically facilitate charge separation in the space charge layer, reducing charge recombination losses and hence increasing water oxidation efficiency. Doping is also found to affect other properties such as morphology, acting as structural directing agents to produce ideal nanostructured architectures [23, 68]. Thus, the synergism from the combination of nanostructuring and elemental doping would be very interesting and can be expected to improve the performance significantly.

Theoretical studies by quantum mechanics calculations have led experimental studies on suitable atoms to use to improve the band-properties of hematite [60, 61, 69-75]. Doping of hematite with different elements such as Ti [38, 76] , Ge [77], Al [78], Si [9, 79], Cr [80], Cu[81], Ta [74], Mn [59, 82] has been proved useful in improving the PEC performance of hematite. Ti is considered one of the attractive dopant element for α-Fe_2O_3 as evidenced by both experimental and theoretical

studies [38, 41-44, 74, 83]. Ti$(4s^2 3d^2)$ has 4 valence electrons and favors a Ti^{4+} charge state. In its stable state, substitution of Ti^{4+} in hematite (Fe^{3+}) act as majority charge carrier (electrons) provider, increasing density of free electrons in α-Fe_2O_3. Two *s* electrons and one *d* electron are accommodated by the O-2p orbital. Ti *d* levels are higher in energy with respect to O-2p non-bonding orbitals than the Fe atom leading Ti to donate the remaining 3d electron to the Fe atom, converting the $Fe^{3+}(d^5)$ to Fe^{2+} (d^6) [60, 84]. Under octahedral environment, the d^6 state is degenerate and experiences weak crystal splittings compared to d^5. Thus, enhanced charge transfer is expected for d^6 coupling between the ions Fe^{2+} and, Fe^{3+} and Ti^{4+} [84, 85].

References

[1] J.Z. Zhang, Metal oxide nanomaterials for solar hydrogen generation from photoelectrochemical water splitting, MRS Bulletin 336 (2011) 48-55.

[2] J. Joy, J. Mathew, S.C. George, Nanomaterials for photoelectrochemical water splitting–review, International Journal of Hydrogen Energy, DOI (2018).

[3] Z. Lin, J. Wang, Low-cost nanomaterials toward greener and more efficient energy applications, Springer, Verlag London, 2014.

[4] Cesar Ilkay, Sivula Kevin, Kay Andreas, Zboril Radek, G. Michael, Influence of Feature Size Film Thickness and Silicon Doping on the Perfomance of Nanostructured Hematite Photoanodes for Solar Water Splitting, J. Phys. Chem. C 113 (2009) 772-782.

[5] Y. LIn, G. Yuan, R. Liu, S. Zhou, S.W. Sheehan, D. Wang, Semiconductor nanostructure-based photoelectrochemical water splitting-A brief review, Chemical Physics Letters, 507 (2011) 209-215.

[6] J.Z. Zhang, Metal oxide nanomaterials for solar hydrogen generation from photoelectrochemical water splitting, MRS Bull., 36 (2011) 48-55.

[7] V.M. Arutyunyan, Physical properties of the semiconductor-electrolyte interface, Sov. Phys. Usp, 32 (1989) 521-540.

[8] R.v.d. Krol, M. Gra¨tzel, Photoelectrochemical Hydrogen Production, Springer,, London New York, 2012.

[9] I. Cesar, K. Sivula, A. Kay, R. Zboril, M. Grätzel, Influence of feature size, film thickness, and silicon doping on the performance of nanostructured hematite photoanodes for solar water splitting, The Journal of Physical Chemistry C, 113 (2008) 772-782.

[10] Y. Lin, G. Yuan, S. Sheehan, S. Zhou, D. Wang, Hematite-based solar water splitting: challenges and opportunities, Energy & Environmental Science, 4 (2011) 4862.

[11] A.G. Tamirat, J. Rick, A.A. Dubale, W.-N. Su, B.-J. Hwang, Using hematite for photoelectrochemical water splitting: a review of current progress and challenges, Nanoscale Horiz., 1 (2016) 243-267.

[12] O. Zandi, A.R. Schon, H. Hajibabaei, T.W. Hamann, Enhanced Charge Separation and Collection in High-Performance Electrodeposited Hematite Films, Chem. Mater., 28 (2015) 765−771.

[13] J.E. Thorne, S. Li, C. Du, G. Qin, D. Wang, Energetics at the Surface of Photoelectrodes and Its Influence on the Photoelectrochemical Properties, J. Phys. Chem. Lett. , 6 (2015) 4083−4088.

[14] A. Fujishima, K. Honda, Electrochemical photolysis of water at a semiconductor electrode, nature, 238 (1972) 37.

[15] R. Abe, Recent progress on photocatalytic and photoelectrochemical water splitting under visible light irradiation, Journal of Photochemistry and Photobiology C: Photochemistry Reviews 11 (2010) 179-209.

[16] K. Ding, B. Chen, Y. Li, Y. Zhang, Z. Chen, Comparative density functional theory study on the electronic and optical properties of BiMO4 (M = V, Nb, Ta), Journal of Materials Chemistry A, 2 (2014) 8294-8303.

[17] S. Chen, L.-W. Wang, Thermodynamic Oxidation and Reduction Potentials of Photocatalytic Semiconductors in Aqueous Solution, Chemistry of Materials, 24 (2012) 3659-3666.

[18] J. Pan, Z. Wang, Q. Chen, J. Hu, J. Wang, Band structure engineering of monolayer MoS2 by surface ligand functionalization for enhanced photoelectrochemical hydrogen production activity, Nanoscale, 6 (2014) 13565-13571.

[19] A. Paracchino, V. Laporte, K. Sivula, M. Grätzel, E. Thimsen, Highly active oxide photocathode for photoelectrochemical water reduction, Nature Materials, 10 (2011) 456.

[20] D.K. Bora, The photocathodic behavior of hierarchical ZnO/hematite hetero nanoarchitectures, Journal of Materials Research, 31 (2016) 1554-1564.

[21] P. Dias, T. Lopes, L. Meda, L. Andrade, A. Mendes, Photoelectrochemical water splitting using WO3 photoanodes: the substrate and temperature roles, Physical Chemistry Chemical Physics, 18 (2016) 5232-5243.

[22] A.G. Tamirat, J. Rick, A.A. Dubale, W.-N. Su, B.-J. Hwang, Using hematite for photoelectrochemical water splitting: a review of current progress and challenges, Nanoscale Horizons, 1 (2016) 243-267.

[23] O. Zandi, B.M. Klahr, T.W. Hamann, Highly photoactive Ti-doped α-Fe2O3 thin film electrodes: resurrection of the dead layer, Energy & Environmental Science, 6 (2013) 634-642.

[24] M. Grätzel, Photoelectrochemical cells, Nature, 414 (2001) 338-344.

[25] M.J. Katz, S.C. Riha, N.C. Jeong, A.B.F. Martinson, O.K. Farha, J.T. Hupp, Toward solar fuels: Water splitting with sunlight and "rust"?, Coordination Chemistry Reviews, 256 (2012) 2521-2529.

[26] A. Duret, M. Grätzel, Visible Light-Induced Water Oxidation on Mesoscopic α-Fe2O3 Films Made by Ultrasonic Spray Pyrolysis, The Journal of Physical Chemistry B, 109 (2005) 17184-17191.

[27] D.K. Bora, A. Braun, E.C. Constable, "In rust we trust". Hematite – the prospective inorganic backbone for artificial photosynthesis, Energy Environ. Sci., 6 (2013) 407-425.

[28] K. Sivula, F. Le Formal, M. Gratzel, Solar water splitting: progress using hematite (alpha-Fe(2) O(3)) photoelectrodes, ChemSusChem, 4 (2011) 432-449.

[29] D. Alexis, G. Michael, Visible Light-Induced Water Oxidation on Mesoscopic α-Fe2O3 Films Made by Ultrasonic Spray Pyrolysis, J. Phys. Chem. B 2005,, 109 (2005) 17184-17191.

[30] A. Braun, K. Sivula, D.K. Bora, J. Zhu, L. Zhang, M. Grätzel, J. Guo, E.C. Constable, Direct Observation of Two Electron Holes in a Hematite Photoanode during Photoelectrochemical Water Splitting, The Journal of Physical Chemistry C, 116 (2012) 16870-16875.

[31] H. Dotan, K. Sivula, M. Grätzel, A. Rothschild, S.C. Warren, Probing the photoelectrochemical properties of hematite (α-Fe2O3) electrodes using hydrogen peroxide as a hole scavenger, Energy Environ. Sci., 4 (2011) 958-964.

[32] F. Boudoire, R. Toth, J. Heier, A. Braun, E.C. Constable, Hematite nanostructuring using electrohydrodynamic lithography, Applied Surface Science, 305 (2014) 62-66.

[33] A. Zoppi, C. Lofrumento, E.M. Castellucci, P. Sciau, Al-for-Fe substitution in hematite: the effect of low Al concentrations in the Raman spectrum of Fe2O3, Journal of Raman Spectroscopy, 39 (2008) 40-46.

[34] M. Rochelle, R. Cornell, U. Schwertmann, The Iron Oxides: Structure, Properties, Reactions, Occurrences and Uses, Wiley-VCH: New York, 2003.

[35] M.N. Batin, V. Popescu, The influence of deposition time on optical properties of iron oxide films grown on glass substrate by Chemical Bath Deposition, Optoelectronics and advanced materials-rapid communications, 6 (2012) 727-729.

[36] C.S.G. Cousins, The corundum structure: internal strain tensors and cluster configurations under stress, Journal of Physics C: Solid State Physics, 14 (1981) 1585.

[37] H. Bialas, H. Stolz, Lattice dynamics of sapphire (corundum), Zeitschrift für Physik B Condensed Matter, 21 (1975) 319-324.

[38] S. Chatman, C.I. Pearce, R.K. M., Charge Transport at Ti-Doped Hematite (001)-Aqueous Interfaces, Chemistry of Materials, 27 (2015) 1665−1673.

[39] S. Kumari, A.P. Singh, D. Deva, R. Shrivastav, S. Dass, V.R. Satsangi, Spray pyrolytically deposited nanoporous Ti 4+ doped hematite thin films for efficient photoelectrochemical splitting of water, international journal of hydrogen energy, 35 (2010) 3985-3990.

[40] K. Sivula, F. Le Formal, M. Grätzel, Solar water splitting: progress using hematite (α-Fe2O3) photoelectrodes, ChemSusChem, 4 (2011) 432-449.

[41] J. Deng, J. Zhong, A. Pu, D. Zhang, M. Li, X. Sun, S.-T. Lee, Ti-doped hematite nanostructures for solar water splitting with high efficiency, J. Appl. Phys., 112 (2012) 084312.

[42] T.S. Atabaev, N.H. Hong, Y.-H. Hwang, M. Ajmal, H.-K. Kim, Ti-doped hematite thin films for efficient water splitting, Appl. Phys. A 118 (2015) 1539-1542.

[43] J.A. Glasscock, P.R. Barnes, I.C. Plumb, N. Savvides, Enhancement of photoelectrochemical hydrogen production from hematite thin films by the introduction of Ti and Si, The Journal of Physical Chemistry C, 111 (2007) 16477-16488.

[44] C.J. Sartoretti, M. Ulmann, B. Alexander, J. Augustynski, A. Weidenkaff, Photoelectrochemical oxidation of water at transparent ferric oxide film electrodes, Chemical Physics Letters, 376 (2003) 194-200.

[45] C. Miao, T. Shi, G. Xu, S. Ji, C. Ye, Photocurrent enhancement for Ti-doped Fe2O3 thin film photoanodes by an in situ solid-state reaction method, ACS applied materials & interfaces, 5 (2013) 1310-1316.

[46] M.J. Katz, S.C. Riha, N.C. Jeong, A.B.F. Martinson, O.K. Farha, J.T. Hupp, Toward solar fuels Water splitting with sunlight and rust, Coordination Chemistry Reviews 256 (2012) 2521-2529.

[47] O. Zandi, A.R. Schon, H. Hajibabaei, T.W. Hamann, Enhanced Charge Separation and Collection in High-Performance Electrodeposited Hematite Films, Chem. Mater. , 28 (2016) 765-771.

[48] O. Zandi, T.W. Hamann, Enhanced Water Splitting Efficiency Through Selective Surface State Removal, J Phys Chem Lett., 5 (2014) 1522-1526.

[49] K. Yu, J. Chen, Enhancing Solar Cell Efficiencies through 1-D Nanostructures, Nanoscale Res. Lett., 4 (2008) 1-10.

[50] J. Yang, C. Bao, T. Yu, Y. Hu, W. Luo, W. Zhu, G. Fu, Z. Li, H. Gao, F. Li, Z. Zou, Enhanced Performance of Photoelectrochemical Water Splitting with ITO@alpha-Fe2O3 Core-Shell Nanowire Array as Photoanode, ACS Appl. Mater. Interfaces., 7 (2015) 26482-26490.

[51] F. Meng, J. Li, S.K. Cushing, J. Bright, M. Zhi, J.D. Rowley, Z. Hong, A. Manivannan, A.D. Bristow, N. Wu, Photocatalytic Water Oxidation by Hematite/Reduced Graphene Oxide Composites, ACS Catal., 3 (2013) 746-751.

[52] J.Y. Kim, G. Magesh, D.H. Youn, J.W. Jang, J. Kubota, K. Domen, J.S. Lee, Single-crystalline, wormlike hematite photoanodes for efficient solar water splitting, Scientific reports, 3 (2013) 2681.

[53] P.S. Bassi, R.P. Antony, P.P. Boix, Y. Fang, J. Barber, L.H. Wong, Crystalline Fe2O3/Fe2TiO5 heterojunction nanorods with efficient charge separation and hole injection as photoanode for solar water oxidation, Nano Energy, 22 (2016) 310-318.

[54] M. Alexander, K. Ilina, F. Alena, F.-R. Dina, B. Thomas, S. Christina, Dual absorber Fe 2 O 3 /WO 3 host-guest architectures for improved charge generation and transfer in photoelectrochemical applications, Materials Research Express, 4 (2017) 016409.

[55] J. Deng, X. Lv, J. Liu, H. Zhang, K. Nie, C. Hong, J. Wang, X. Sun, J. Zhong, S.-T. Lee, Thin-Layer Fe2TiO5 on Hematite for Efficient Solar Water Oxidation, ACS Nano, 9 (2015) 5348-5356.

[56] D.A. Wheeler, G. Wang, Y. Ling, Y. Li, J.Z. Zhng, Nanostructured hematite: synthesis, characterization, charge carrier dynamics, and photoelectrochemical properties, Energy Environ. Sci., 5 (2012) 6682–6702.

[57] J.Y. Kim, G. Magesh, D.H. Youn, J.-W. Jang, J. Kubota, K. Domen, J.S. Lee, Single-crystalline, wormlike hematite photoanodes for efficient solar water splitting, Scientific Reports, 3 (2013) 2681.

[58] J.-J. Wang, Y. Hu, R. Toth, G. Fortunato, A. Braun, A facile nonpolar organic solution process of a nanostructured hematite photoanode with high efficiency and stability for water splitting, Journal of Materials Chemistry A, 4 (2016) 2821-2825.

[59] Gurudayal, S.Y. Chiam, M.H. Kumar, P.S. Bassi, H.L. Seng, J. Barber, L.H. Wong, Improving the Efficiency of Hematite Nanorods for Photoelectrochemical Water Splitting by Doping with Manganese, ACS Applied Materials & Interfaces, 6 (2014) 5852-5859.

[60] H. Pan, X. Meng, J. Cai, S. Lia, G. Qin, 4d transition-metal doped hematite for enhancing photoelectrochemical activity: theoretical prediction and experimental confirmation, RSC Adv., 5 (2015) 19353–19361.

[61] M.N. Huda, A. Walsh, Y. Yan, S.-H. Wei, M.M. Al-Jassim, Electronic, structural, and magnetic effects of 3d transition metals in hematite, J. Appl. Phys. , 107 (2010) 123712.

[62] R.R. Rangaraju, A. Panday, K.S. Raja, M. Misra, Nanostructured anodic iron oxide film as photoanode for water oxidation, Journal of Physics D: Applied Physics, 42 (2009) 135303.

[63] D.A. Wheeler, G. Wang, Y. Ling, Y. Li, J.Z. Zhang, Nanostructured hematite: synthesis, characterization, charge carrier dynamics, and photoelectrochemical properties, Energy & Environmental Science, 5 (2012) 6682-6702.

[64] S. Shinde, R. Bansode, C. Bhosale, K. Rajpure, Physical properties of hematite α-Fe2O3 thin films: application to photoelectrochemical solar cells, Journal of Semiconductors, 32 (2011) 013001.

[65] X.Y. Meng, G.W. Qin, S. Li, X.H. Wen, Y.P. Ren, W.L. Pei, L. Zuo, Enhanced photoelectrochemical activity for Cu and Ti doped hematite: The first principles calculations, Applied Physics Letters, 98 (2011) 112104.

[66] D. Cao, W. Luo, M. Li, J. Feng, Z. Li, Z. Zou, A transparent Ti 4+ doped hematite photoanode protectively grown by a facile hydrothermal method, CrystEngComm, 15 (2013) 2386-2391.

[67] M. Barroso, S.R. Pendlebury, A.J. Cowan, J.R. Durrant, Charge carrier trapping, recombination and transfer in hematite (α-Fe2O3) water splitting photoanodes, Chem. Sci., 4 (2013) 2724–2734.

[68] Y. Zhang, H. Ji, W. Ma, C. Chen, W. Song, J. Zhao, Doping-Promoted Solar Water Oxidation on Hematite Photoanodes, Molecules, 21 (2016) 868.

[69] X. Meng, G. Qin, W.A. Goddard III, S. Li, H. Pan, X. Wen, Y. Qin, L. Zuo, Theoretical understanding of enhanced photoelectrochemical catalytic activity of Sn-doped hematite: Anisotropic catalysis and effects of morin transition and Sn doping, The Journal of Physical Chemistry C, 117 (2013) 3779-3784.

[70] H. Pan, X. Meng, D. Liu, S. Li, G. Qin, (Ti/Zr,N) codoped hematite for enhancing the photoelectrochemical activity of water splitting, Phys. Chem. Chem. Phys., 17 (2015) 22179-22186.

[71] Z.D. Pozun, G. Henkelman, Hybrid density functional theory band structure engineering in hematite, The Journal of Chemical Physics, 134 (2011) 224706.

[72] D. Varshney, A. Yogi, Structural and Electrical conductivity of Mn doped Hematite (a-Fe2O3) phase, Journal of Molecular Structure, 995 (2011) 157-162.

[73] J. Velev, A. Bandyopadhyay, W. Butler, S. Sarker, Electronic and magnetic structure of transition-metal-doped α-hematite, Physical Review B, 71 (2005) 205208.

[74] X. Zhang, H. Li, S. Wang, F.-R.F. Fan, A.J. Bard, Improvement of hematite as photocatalyst by doping with tantalum, The Journal of Physical Chemistry C, 118 (2014) 16842-16850.

[75] Y. Hu, D.K. Bora, F. Boudoire, F. Haeussler, M. Graetzel, E.C. Constable, A. Braun, A dip coating process for large area silicon-doped high performance hematite photoanodes, Journal Of Renewable And Sustainable Energy, 5 (2013).

[76] X. Xie, K. Li, W.-D. Zhang, Photoelectrochemical properties of Ti-doped hematite nanosheet arrays decorated with CdS nanoparticles, RSC Advances, 6 (2016) 74234-74240.

[77] S. Li, J. Cai, Y. Mei, Y. Ren, G. Qin, Thermal oxidation preparation of doped hematite thin films for photoelectrochemical water splitting, International Journal of Photoenergy, 2014 (2014).

[78] W. Li, X. Liang, P. An, X. Feng, W. Tan, G. Qiu, H. Yin, F. Liu, Mechanisms on the morphology variation of hematite crystals by Al substitution: The modification of Fe and O reticular densities, Scientific reports, 6 (2016) 35960.

[79] D.K. Bora, Fabrication of silicon doped hematite photoelectrode with enhanced photocurrent density via solution processing of an in-situ TEOS modified precursor, Materials Science in Semiconductor Processing, 31 (2015) 728-738.

[80] F. Bouhjar, M. Mollar, M.L. Chourou, B. Marí, B. Bessaïs, Hydrothermal synthesis of nanostructured Cr-doped hematite with enhanced photoelectrochemical activity, Electrochimica Acta, 260 (2018) 838-846.

[81] E.L. Tsege, T.S. Atabaev, M.A. Hossain, D. Lee, H.-K. Kim, Y.-H. Hwang, Cu-doped flower-like hematite nanostructures for efficient water splitting applications, Journal of Physics and Chemistry of Solids, 98 (2016) 283-289.

[82] S.Y. Chiam, M.H. Kumar, P.S. Bassi, H.L. Seng, J. Barber, L.H. Wong, Improving the efficiency of hematite nanorods for photoelectrochemical water splitting by doping with manganese, ACS applied materials & interfaces, 6 (2014) 5852-5859.

[83] O. Zandi, T.W. Hamann, The potential versus current state of water splitting with hematite, Physical Chemistry Chemical Physics, 17 (2015) 22485-22503.

[84] A. Bandyopadhyay, J. Velev, W. Butler, S.K. Sarker, O. Bengone, Effect of electron correlations on the electronic and magnetic structure of Ti-doped α-hematite, Physical Review B, 69 (2004) 174429.

[85] R. Strens, B. Wood, Diffuse reflectance spectra and optical properties of some iron and titanium oxides and oxyhydroxides, Mineralogical Magazine, 43 (1979) 347-354.

Chapter 3

Experimental Details

3.1 Chemicals and reagents

Preparation of samples used during this study was carried out at the Laboratory for High-Performance Ceramics, Swiss Federal Laboratories for Materials Science and Technology, Empa, Dübendorf in Switzerland. The chemicals used were all of analytical grade and supplied by Sigma Aldrich, UK. These include;

1. Iron (III) nitrate nanohydrate $(Fe(NO_3)_3 \cdot 9H_2O)$, 99.95%

2. OLEIC acid $(C_{18}H_{34}O_2)$, $\geq 99\%$ (GC)

3. Tetrahydrofuran, anhydrous (C_4H_{80}), $\geq 99.9\%$

4. Deionized water

5. Titanium (IV) butoxide $Ti(OBu)_4$, 97 %

6. Compressed Nitrogen (99.99%)

3.2 Synthesis Method

Hematite thin films were produced by simple and low-cost spin coating and dip coating methods using fluorine-doped tin oxide (FTO) glass as substrates. For spin coating, an SM-180-BT SAWATEC spin coater was used, while a dip coater DipMasterTM-50 (Chemat Technology Inc., USA) was used for dip coating. The preparation procedure involved repeated deposition, drying and annealing at elevated temperatures.

3.3 Analytical equipment

X-Ray Diffractometry (XRD): X-ray diffraction is a conventional technique used to examine phase purity and crystallinity of different forms of materials. Powder X-ray diffraction (PAN analytical X'Pert PRO) fitted with Co-Kα (λ = 1.79801 Å), and Cu-Kα (λ =1.5401 Å) radiation was used for structural analysis of the fabricated iron oxide thin films, at room temperature.

Raman Spectroscopy: Raman spectroscopy (Horiba Jobin-Yvon T64000) equipped with a 100x working-distance objective and a nitrogen-cooled CCD detector was used to study the vibrational properties of hematite thin films. An argon-ion laser line at 514.5 nm was used as the excitation source. High-resolution confocal Raman microscopy WITec alpha300R (confocal Raman imaging, AFM and SNOM), line 532 nm laser radiation was also used during the study. To avoid local heating of the samples, laser power was kept low enough (0.15 mW), focused on a spot size of about 5 µm on the sample.

UV-Vis Spectroscopy: Optical properties of the films were measured with a Cary 5E UV/VIS/NIR spectrophotometer operating in the wavelength region of 300-800 nm. The absorption spectrum was measured against an uncoated FTO substrate as a reference without further corrections for reflection and scattering losses.

High-resolution field emission scanning electron microscopy (FESEM): FESEM employing Zeiss Ultra 55 instrument (Carl Zeiss AG) fitted with the usual SEM detectors and in-lens detector, operating at 2kV was used for surface morphology of the films throughout the study.

Atomic Force Microscopy (AFM): A Nanoscope atomic force microscope (AFM) were performed in a tapping mode at a scan rate of 0.4 Hz, to analyze surface morphology and surface roughness of the films.

X-ray Photoelectron Spectroscopy (XPS): A Thermo SCIENTIFIC K-alpha X-ray photoelectron spectrometer equipped with a 100 mm monochromatic Al- Kα radiation source was used to verify incorporation of Ti in hematite.

Profilometry: Film thickness of the prepared thin films were measured with a mechanical profilometry (*P-15 KLA Tencor*).

Impedance spectroscopy

The electrochemical impedance (EIS) properties were investigated to understand the charge transfer properties of the samples [1], by a Bio-Logic VMP300 potentiostat (Knoxville TN 37930, USA) controlled by the EC-Lab® V10.40 software in a three-electrode configuration. A hematite thin film, a carbon plate and a Ag/ AgCl (3 M KCl) were employed as the working, counter and reference electrodes respectively. A 1 M potassium hydroxide (KOH) electrolyte was used for analysis. The EIS measurements were performed in darkness within a frequency range of 0.01 Hz to 100 kHz.

Photoluminescence spectroscopy

Photoluminescence spectroscopy (PL) is a useful tool commonly used to understand the charge transfer, trapping and recombination process of the charge carriers in semiconductor materials [2]. A PL study was carried out at room temperature using a Perkin-Elmer LS-55 Fluorescence Spectrometer.

Photoelectrochemical properties

All photoelectrochemical measurements were carried out in a photoelectrochemical system comprising of a potentiostat (Voltalab80 PGZ 402) interfaced with a PC, a three-electrode photoelectrochemical cell, also known as a "cappuccino cell", (manufactured from PEEK plastic) [3], and a solar simulator 1 Sun Oriel lamp from L.O.T-Oriel AG. A hematite sample, a platinum plate (0.5 × 0.5 cm) and a Ag/AgCl/3M KCl electrode were employed as the working, cathode and reference electrodes, respectively. Potassium hydroxide (KOH) was used as the electrolyte solution.

References

[1] X. Xie, K. Li, W.-D. Zhang, Photoelectrochemical properties of Ti-doped hematite nanosheet arrays decorated with CdS nanoparticles, RSC Advances, 6 (2016) 74234-74240.

[2] Y.W. Phuan, E. Ibrahim, M.N. Chong, T. Zhu, B.-K. Lee, J.D. Ocon, E.S. Chan, In situ Ni-doping during cathodic electrodeposition of hematite for excellent photoelectrochemical performance of nanostructured nickel oxide-hematite p-n junction photoanode, Applied Surface Science, 392 (2017) 144-152.

[3] A. Braun, Q. Chen, D. Flak, G. Fortunato, K. Gajda-Schrantz, M. Grätzel, T. Graule, J. Guo, T.W. Huang, Z. Liu, Iron resonant photoemission spectroscopy on anodized hematite points to electron hole doping during anodization, ChemPhysChem, 13 (2012) 2937-2944.

Chapter 4

Surface structural properties of hematite prepared by dip coating: effect of electrochemical oxidation

4.1 Introduction

Hematite is, from many points of view, a potential photoanode material for photoelectrochemical water splitting [1-3]. However, like most investigated materials, an unassisted water oxidation reaction is not possible, and thus potentials of over 1 V *versus* RHE are required to drive the chemical reactions. Upon exposure to anodic bias in contact with an alkaline electrolyte, several electrochemical reactions take place on the electrode surface, even at room temperature. Electrochemical oxidation (anodization), especially, is considered an operational step in the functionality of a photoelectrochemical cell [4]. Anodization involves formation of an oxide layer resulting from oxidation of the surface that, may increase the corrosion resistance of the metal [5]. Compared to other electrochemical processes, significant heat is generated during anodization [6]. The produced heat can have a substantial influence on modifying the microstructure at the photoanode surface, which subsequently influence its functionality under PEC environment.

During anodization, the applied anodizing potential causes dissociation of water, and possibly the electrolyte, to occur at the oxide-electrolyte interface [5]. Also, a significant amount of anions is supplied by water dissociation due to the water splitting process. Accordingly, some of the ions combine with oxygen anions and form a metal oxide [5, 7]. A thin layer of oxide film forms by both outward and inward diffusion of ions through the oxide-electrolyte interface and simultaneously oxidation heat is generated [8, 9]. The growth of this anodic oxide film is a complex process, involving transport of matter and charge between different phases, like metal, oxide and

anodizing medium. Both chemical dissolution and electric field dissolution play a role in the structure and composition of the formed anodic film [8]. The thickness of the formed anodic oxide layer is influenced by the charge passed (i.e. the product of current density and time) whereas the morphology and composition depend on the anodizing conditions like anodizing potential and time, reaction temperature, electrolyte type, pH and concentration [6]. The surface undergoes extensive morphological reorganization upon anodization. The oxide scales are in continuous transformation including grain growth, phase transformation, porosity, recrystallization, development and thickening that depend on anodizing conditions [10].

Published results revealed that molecular electronic properties at and near the hematite surface change upon anodization [4, 11-13]. According to Gajda-Schrantz *et al.* new electronic states are probably formed on and below the hematite surface upon anodization at 600 mV *versus* Ag/AgCl in KOH, pointing to hole doping [12]. Also, in another study, Braun *et al.* assumed that "continued exposure to the anodizing conditions might cause preservation of the formed states in the form of a thin anodic film, the thickness of which scales with exposure time," [13]. On the basis of their report, it appears that anodization may possibly also affect the microstructural features of the photoanode.

Microstructural features such as crystallinity, crystal size, shape and spatial distribution, defects, particle size, morphology and texture play an essential role in the functional performance of the photoelectrode in a PEC cell [14, 15]. The surface properties of the photoelectrode significantly influence charge transport and transfer efficiency at the semiconductor-electrolyte interface. In this thesis, the effect of anodization on microstructural properties at the hematite surface is investigated.

4.2 PART A: Morphological, structural and optical properties of hematite thin film upon electrochemical oxidation

4. 2A.1 Materials and methods

4. A.1.1 Electrode preparation

Pristine hematite thin films were synthesized by dip coating of iron oleate precursor complex on a conductive fluorine-doped tin oxide (FTO; TEC-8 Pilkington supplied by Hartford Glass, MA) coated glass substrates in a systematic procedure illustrated in Figure 4-1. The FTO substrates were pre-washed in an ultrasonic bath of acetone and isopropanol for 30 min, rinsed with ethanol and blown dry with compressed N_2 (99.95%). An iron oleate precursor complex was prepared by heating 17.0 g of oleic acid ($C_{18}H_{34}O_2$) to 125 ˚C using a hot plate before adding 28.0 g of iron (III) nitrate ($Fe(NO_3)_3{\cdot}9H_2O$) in small amounts while continuously stirring to give a red-brown viscous mass. The complex mixture was then cooled to room temperature and left to dry in the fume hood for 24h. Subsequently, 70 mL of tetrahydrofuran (THF) was added to dissolve the contents followed by high-speed centrifugation (4000 rpm) for 30 min. The resultant supernatant solution was recovered for further processing. During deposition, the substrate was immersed into the solution for the 30s then withdrawn with a speed of 130 mm/min. The iron-oleate thin films were dried at 70 °C on a hot plate, after removing the precursor from the back of the substrate with an acetone-soaked wipe. The films were annealed in a furnace at 500 ˚C for 30 minutes at a heating and cooling rate of 10 °C/min. During annealing, excess hematite peeled off from the surface which was removed with a paper towel after cooling. The deposition, drying and heat treatment steps were repeated four times in this order to obtain optimized hematite thin films of four layers.

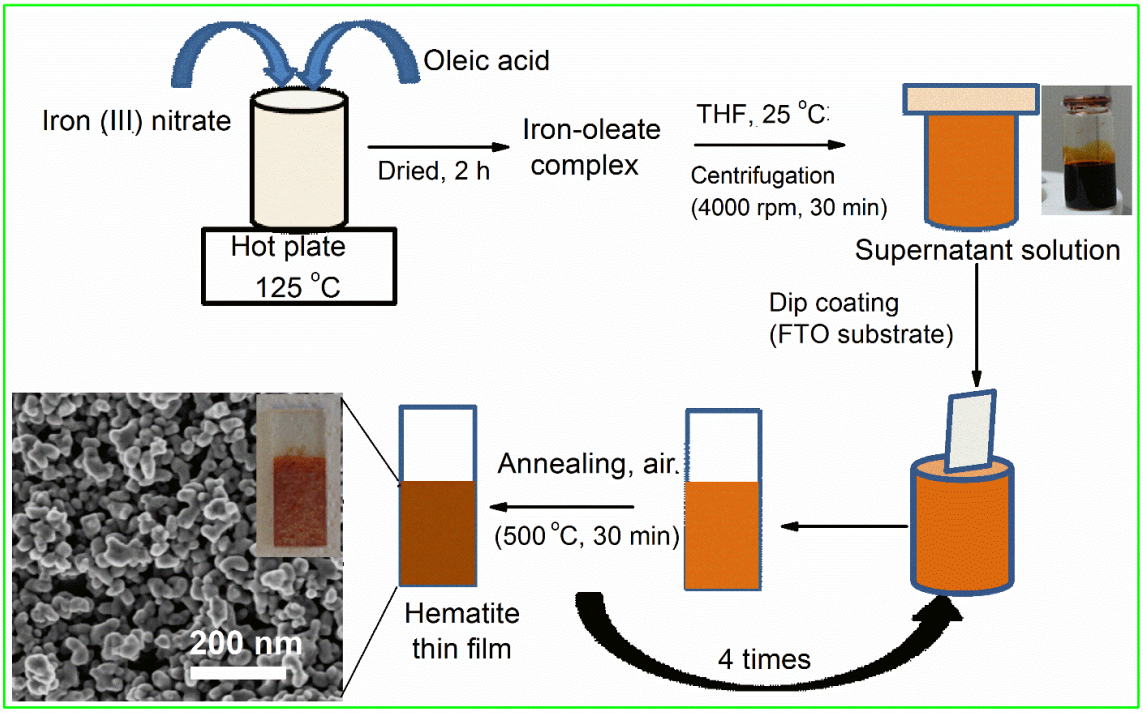

Figure 4-1: A schematic presentation of a systematic procedure for the preparation of dip-coated pristine α-Fe_2O_3 nanostructures[16].

4.A.1.2 Electrochemical oxidation process

Anodization of the film was carried out in a photoelectrochemical system comprising of a potentiostat (Voltalab80 PGZ 402) interfaced with a PC, a three-electrode photoelectrochemical cell, also known as a "cappuccino cell", (manufactured from PEEK plastic) [13], and a solar simulator 1 Sun Oriel lamp from L.O.T-Oriel AG as shown in Figure 4-2. Figure 4-2 B shows the corresponding scheme of the system. A hematite sample, a platinum plate (0.5 × 0.5 cm) and a Ag/AgCl/3M KCl electrode were employed as the working, cathode and reference electrodes, respectively. Potassium hydroxide (KOH) was used as the electrolyte solution. The electrical contact of the photoanode was established through the FTO layer on the substrate and the titanium plate on the sample holder of the PEC cell. The simulated sunlight corresponded to the AM 1.5 Global solar spectrum. A constant anodic potential of 500 mV *vs* a Ag/AgCl electrode was applied to the working electrode of an area of 2.5 cm^2, immersed in 10 cm^3 of 1 M KOH (pH=13.8) in

darkness and under illumination for 60 s. The sample was heated from the front through a bull-eye-shaped window of an area of 28.3 cm^2. The anodized samples were later washed with double distilled water to remove the occluded ions from the anodized solutions and left to dry in air.

4.A.1.3 Characterization of the samples

Spectroscopy measurements were carried out before and after exposure to PEC environment conditions. The phase composition and crystallinity of the thin films were analyzed by powder x-ray diffraction with cobalt-Kα radiation. The surface morphology was examined using a high-resolution field emission scanning electron microscopy (FESEM, Carl Zeiss AG) operating at 2 kV. Raman spectra of the films were obtained in 180° backscattering geometry with a 0.15 mW Ar+ laser at a wavelength of 514.5 nm, focused on a spot size of about 5 μm. The absorption spectra of the films were measured by a Cary 5E UV/VIS/NIR spectrophotometry, using a blank FTO substrate as the reference.

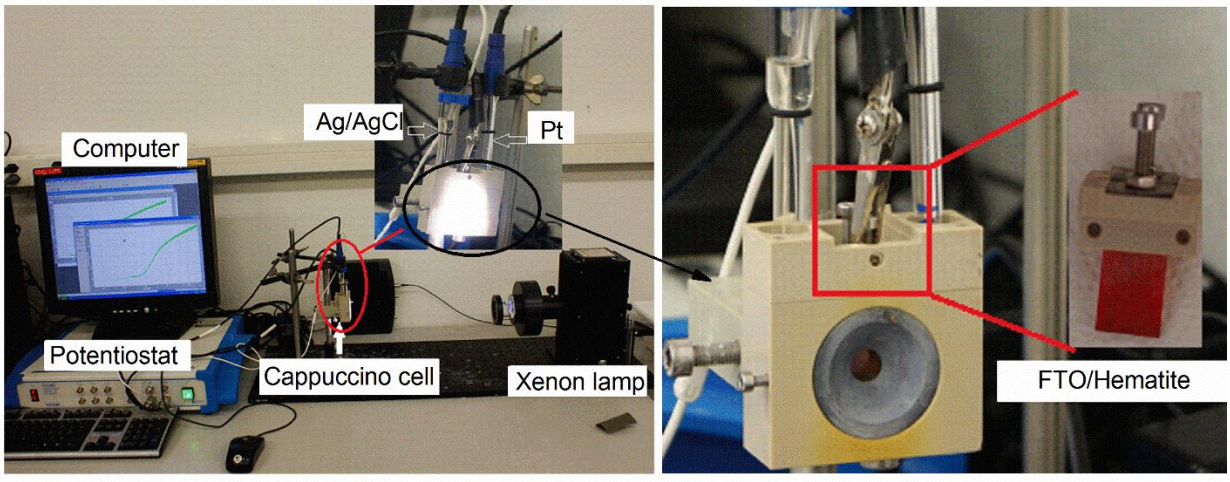

(A)

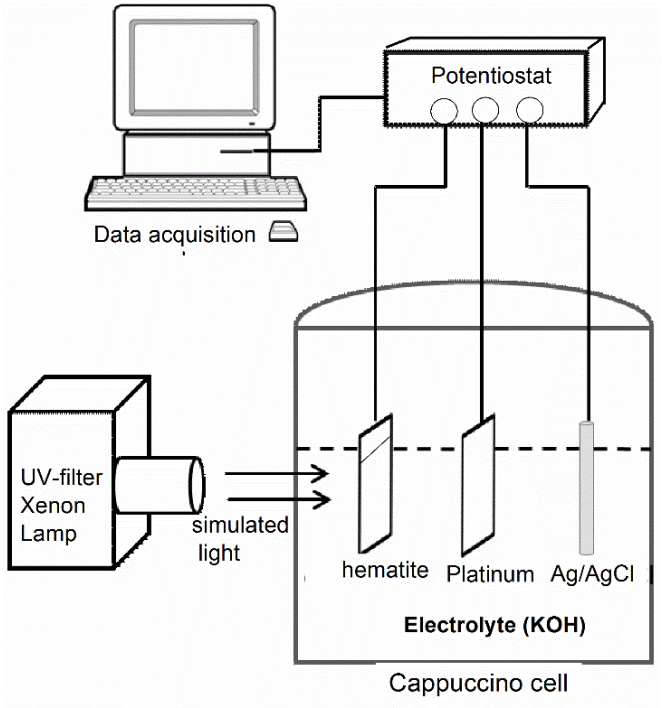

(B)

Figure 4-2**:** Test bench setup (left) for the photoelectrochemical cell characterization: (A) photo of the actual setup (A: left) and the expanded view of the cappuccino cell ((A: right) and the (B) corresponding scheme[16].

4. 2A.2 Results and discussion

The scanning electron microscopic imaging of the synthesized pristine and treated hematite thin films was obtained as presented in Figure 4-3. The electron microscopy data revealed formation of a porous film with spherical nanoparticles on the surface. Initially, the particles were smaller and irregular in shape as is evident from the micrographs. It is quite clear from the figure that upon anodization the particle size increased and grew into a regular spherical shape. The average particle size increased from ~57 nm for pristine nanoparticles to ~ 73 nm upon anodization in darkness. Under illumination, the particle size increased to ~ 77 nm. The increase in particle size under light could be attributed to Ostwald ripening; whereby large particles grow at the expense of small particles as a result of an increase in temperature at the surface.

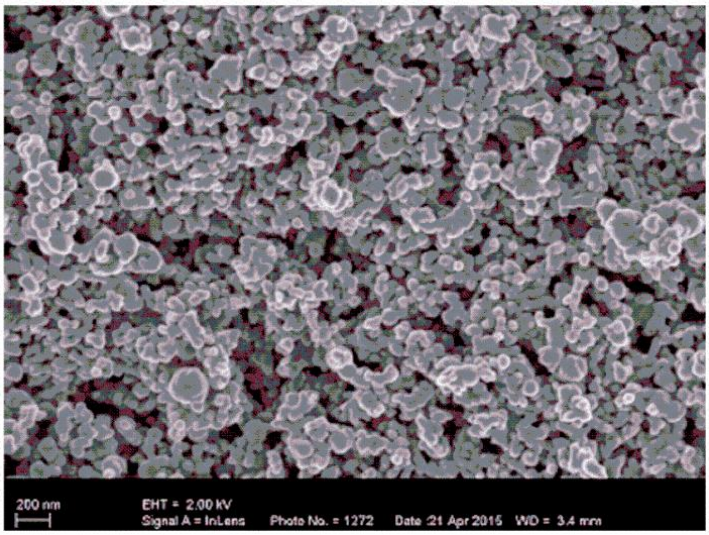

(A)

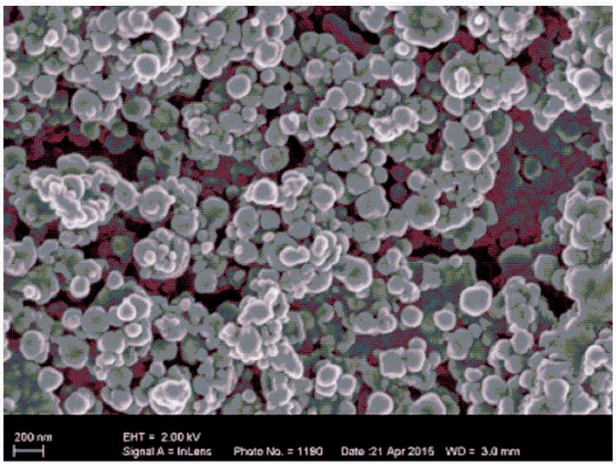

(B)

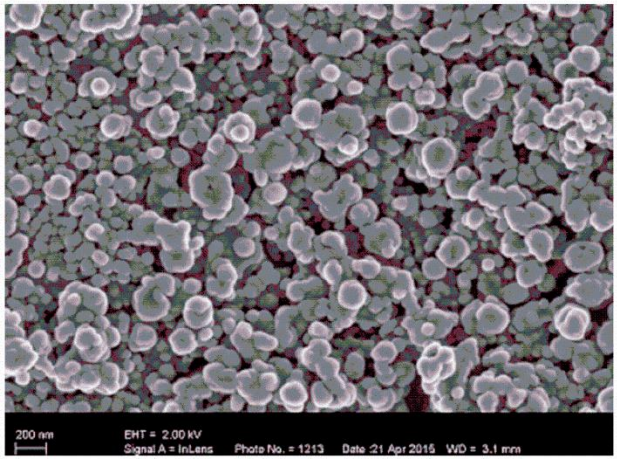

(C)

Figure 4-3:FE-SEM top-view images of pristine hematite film (A) anodized nanostructures treated for 60 s at a constant anodic potential of 500 mV a Ag/AgCl electrode , in darkness (B) and with and under illumination (C) [17].

The phase composition and crystallinity of the nanostructures were examined using X-ray diffractometry. Figure 4-4 shows the XRD diffraction patterns of the α-Fe_2O_3 nanostructures before and after electrochemical oxidation. The strong peaks in all the samples confirm the formation of nanoparticles with high crystallinity. The XRD patterns showed peaks corresponding to α-Fe_2O_3 phase with lattice constants a = b = 5.032, c = 13.733 and R-3c space group [JCPDS

#89-0599]. Two strong hematite characteristic peaks were observed at 2θ values of 38.76 and 41.67˚ corresponding to (104) and (110) hematite crystal planes. Additional weaker diffraction peaks were also observed at 2θ values corresponding to (012), (113), (024), and (116) planes in hematite. The XRD patterns are consistent with previous studies [1]. The peaks, however, were shifted to higher Bragg angles due to the difference in the wavelength (0.179801 nm) of the incoming X-rays which are dependent on the X-ray source (cobalt). For example, (104) and (110) peaks are usually reported at 2θ values of ~33.1˚ and ~35.5˚ respectively with a Cu-$k_{\alpha-1}$ radiation source[1]. The sharp and narrow peaks with a small full width at half maximum (FWHM), indicated that the synthesized hematite nanocrystals were well crystallized [18]. Highly ordered crystalline materials are essential towards achieving high solar conversion efficiencies. As the crystallinity increases the density of defects and the site for electron-hole recombination decreases, which suggests that structural property can influence the photocurrent efficiency [19]. A close inspection of the expanded (104) peak in Figure 4-4 B showed a significant decrease in FWHM in anodized samples, suggesting an increase in crystallite size upon anodization. Crystallite size, D was estimated according to the Scherrer equation for x-ray diffractions [20];

$$D = \frac{0.94\lambda}{\beta \cos\theta} \tag{4.1}$$

Here, β and θ are the FWHM and Bragg angle, respectively. The average crystallite size for the samples was found as presented in Table 4-1. The XRD results confirmed electron microscopy data. The average crystallite size increased from ~ 33 nm for the pristine sample to 41 and 43 nm for anodized samples under light and darkness, respectively.

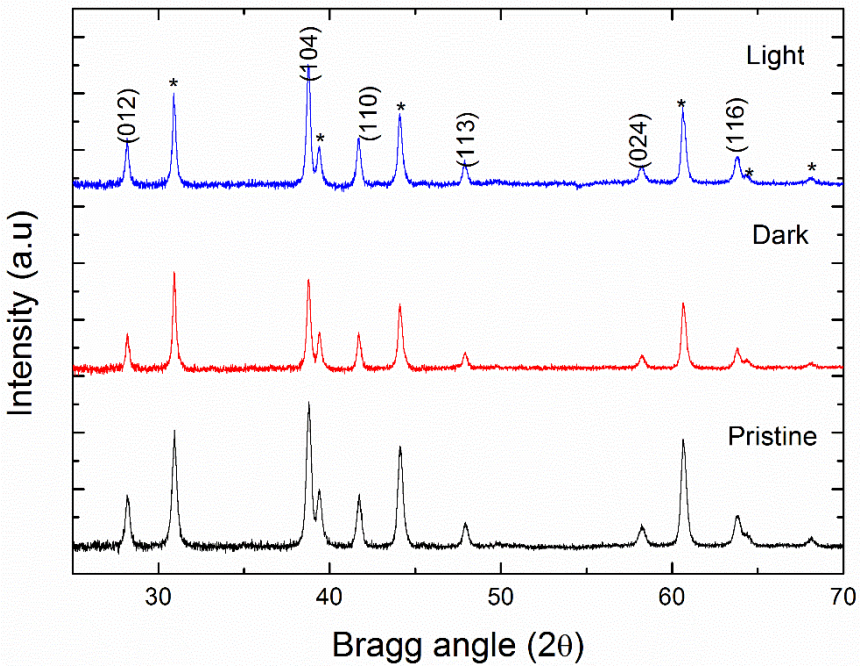

(A)

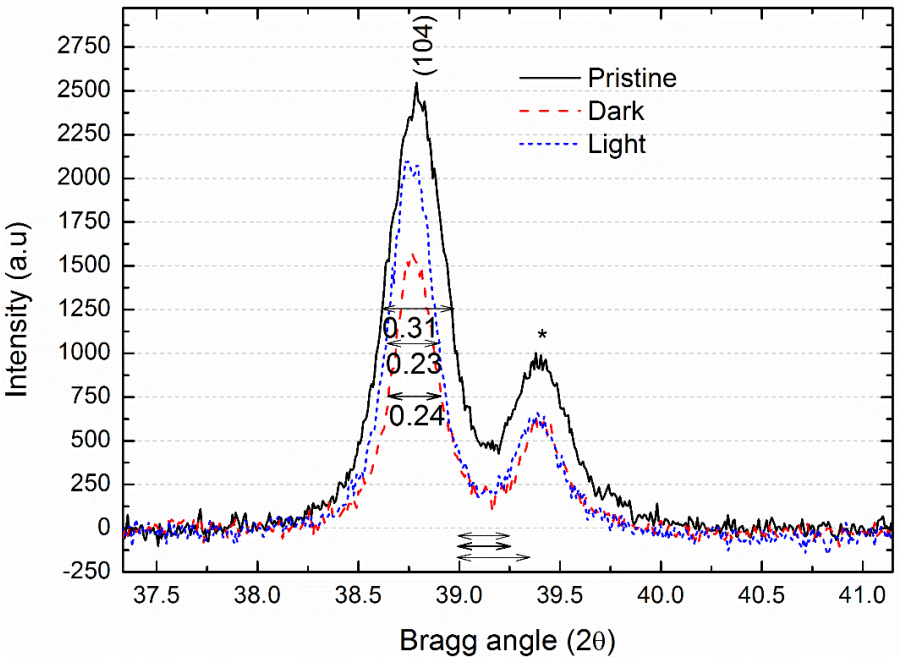

(B)

Figure 4-4: XRD patterns of pristine and anodized nanostructured α-Fe_2O_3. The peaks marked with (*) corresponds to SnO_2 originating from the substrate [ICSD #77-0451]. (B) Shows the expanded view of the (104) peak, clearly showing a decrease in FWHM upon anodization[17].

Table 4-1: Full width half maximum (FWHM) and average crystallite size (D) of nanostructured hematite before and after electrochemical oxidation in 1M KOH at 500 mV, for 60s [17].

Sample name	FWHM (2θ)			D(nm)
	(012)	(104)	(110)	
Pristine	0.283	0.307	0.315	33
Light	0.209	0.230	0.307	41
Dark	0.215	0.235	0.303	43

Raman spectra of the films shown in Figure 4-5 confirmed the formation of α-Fe_2O_3 from the crystallographic point of view, as evidenced by the appearance of the distinct sharp seven first-order Raman optical phonon modes (two A_{1g} modes, five E_g mode) predicted [21], and calculated in this work by group theory. It is worth noting; however, that group theory does not tell the frequencies of the phonon modes. Therefore, the phonon modes were assigned according to polarized Raman spectra analysis in Ref. [22] and tabulated in Table 4-2. The two phonon modes at frequencies of 220 and 493 cm^{-1} were assigned to fully symmetric A_{1g} modes. The active phonon mode at 220 cm^{-1} is attributed to cations vibrating against each other along the principal axis, while the latter arises from the interaction of the lighter O atoms vibrating perpendicular to the *c*-axis [22]. The polar doubly degenerate E_g phonon modes arise from lattice atomic vibrations in the basal planes, beating in the direction perpendicular to the *c*-axis and split into longitudinal optical (LO) and transverse optical (TO) modes [22]. The expanded curves of the phonon modes in the wavenumber region of 200-350 cm^{-1} in Figure 4-5B, clearly showed broadening and shifting of peaks to lower wavenumbers upon anodization.

A summary of the peak positions and linewidths as obtained by fitting the measured peaks by Lorentzian shape is tabulated in Table 4-2. Residual strain in thin film heterostructures is an

essential issue in device fabrication. Usually, micro-stress in crystallites may be due to vacancies, defects, thermal expansions and contractions of unit cells etc. Compressive stress induces a blue shift in Raman phonon frequencies, while tensile stress induces a redshift [23]. Thus, the observed redshift and broadening in the anodized films indicates weakening of Fe-O bonds in the FeO_6 octahedra, probably due to size-induced lattice expansion [4, 24]. No other phases were detected, which corroborates XRD data.

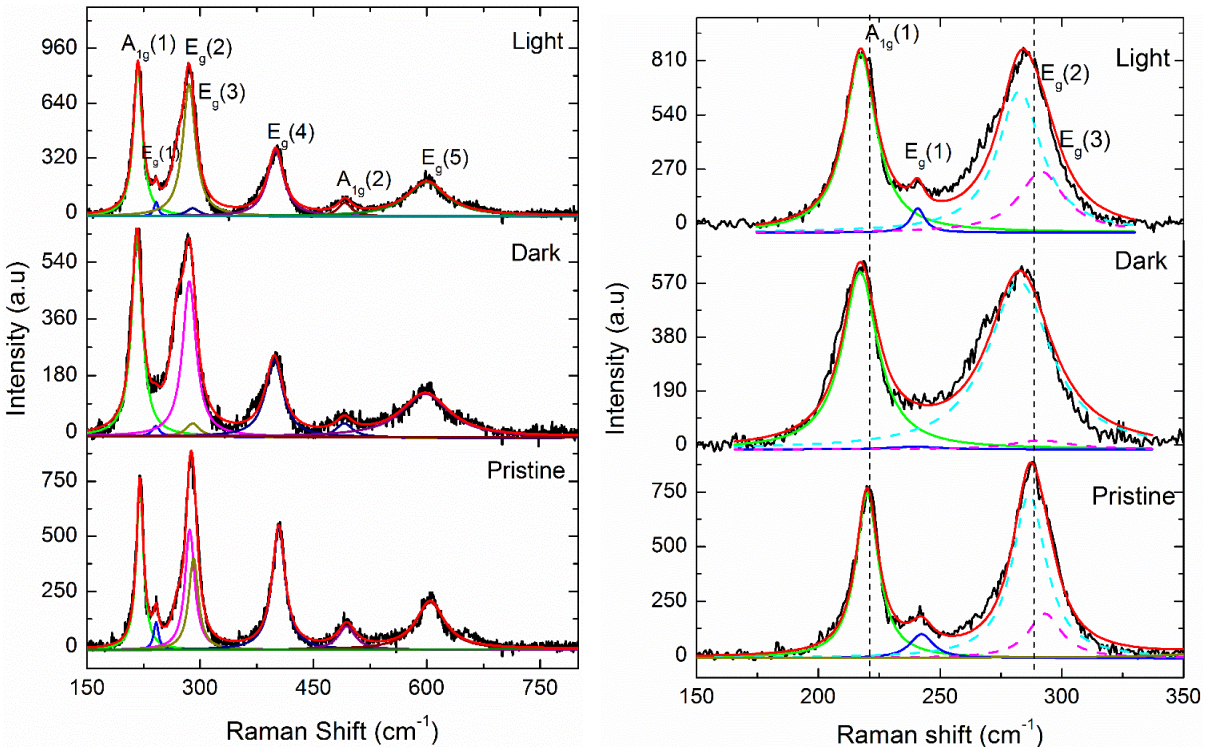

Figure 4-5: (A) Raman spectra of α-Fe_2O_3 nanoparticles: before and after anodization at 500 mV for 60 s. (B) shows fitted and deconvoluted expanded curves of the phonon modes in the wavenumber region of 200-350 cm^{-1} [17].

Table 4-2: Wavenumbers (ν) and linewidth (FWHM) of the pristine and anodized nanostructured α-Fe_2O_3 (D_{3d}^6 -symmetry) and their symmetry assignments [17].

Pristine (this work)		Anodized in light		Anodized in dark		Exp (pristine) [25]	Symmetry assignment
ν /cm^{-1}	FWHM /cm^{-1}	ν /cm^{-1}	FWHM /cm^{-1}	ν /cm^{-1}	FWHM /cm^{-1}	ν /cm^{-1}	
220.1	11.07	217.9	14.2	216.2	17.4	224	A_{1g} (1)
493.9	26.8	492.2	28.4	490.5	29.8	496	A_{1g} (2)
241.8	7.85	241.8	29.3	240.7	26.7	243	E_g (1)
287.6	19.7	284.6	24.5	286.3	19.2	290	E_g (2)
296	19.7	293.6	24.5	290.5	29.5	297	E_g (3)
403.8	20.3	400.3	26.5	397.9	29.6	408	E_g (4)
604.7	48.1	600	61.4	598	82.7	609	E_g (5)

Because the absorption efficiency of the photoanode is strongly dependent on structural properties like morphology, type and size of the particles and crystallinity, the optical properties of the films were examined with respect to the modifications on the surface morphology. Higher crystallinity leads to better visible light absorption and charge separation and hence better PEC performance of the nanocrystals [19, 26]. The obtained optical absorption and transmittance (inset) spectra are shown in Figure 4-6. The spectra show a very low relative absorption intensity for pristine films obtained by UV-vis spectroscopy. In comparison, the relative intensity of the anodized films was enhanced throughout the visible region. Also, the absorption band is slightly shifted to longer wavelengths from ~ 535 nm for pristine film to 560 nm for anodized films, which suggested a decrease in the energy bandgap upon anodization. Conversely, the relative intensity of transmittance of the films (inset) decreased as the absorption increased. The difference in the relative intensity of absorption or transmittance was attributed to the variation in particle size and the enhanced surface upon anodization [27].

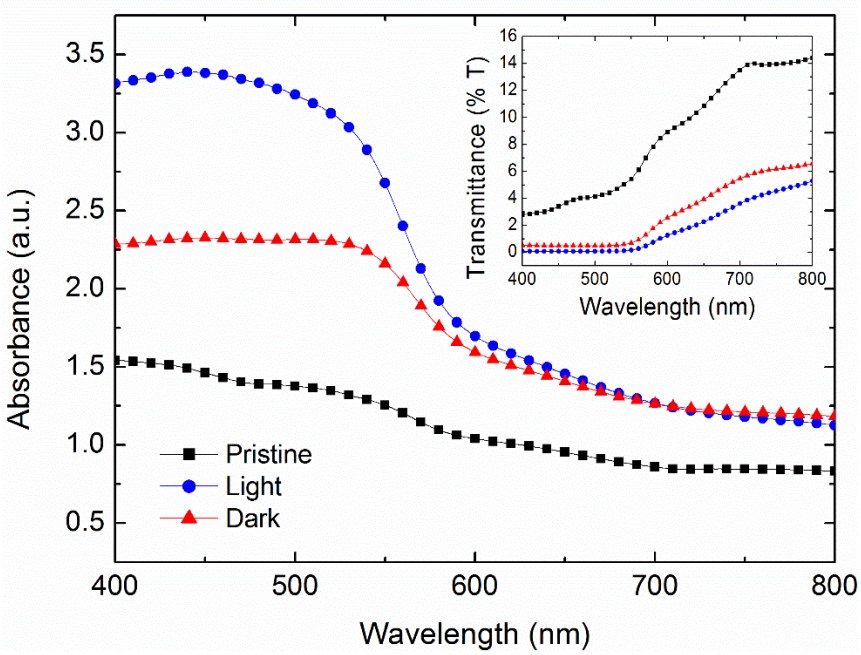

Figure 4-6: UV-vis absorption and transmittance (inset) spectra of the films before and after electrochemical oxidation [17].

4. 2A.3 Concluding remarks

Nanostructured hematite thin films were prepared by a simple dip coating technique and electrochemically oxidized (anodized) in 1molar of KOH at a constant potential of 500mV vs the Ag^{+}/AgCl electrode for 60 s. The X-ray diffractometry and electron microscopy analyses revealed significant modifications on the size of the nanoparticles at the surface, without changing the crystallographic structure. After all, only the surface is expected to be affected during anodization and not the bulk [4]. The crystallite size increased from ~33 nm for the film in the pristine state to ~ 41 nm for the film anodized under illumination. Also, SEM imaging revealed enhanced surface as the particles grow into a regular spherical shape and larger size compared to the pristine film. The average particle size increased from approximately ~ 57 nm for pristine samples to ~73 and 77 nm for samples anodized in the dark and under illumination, respectively. The changes on the structural features at the surface influenced the optical properties of the anodized films. Optical

absorption was enhanced during anodization compared to pristine film. The role of the exposure time on the modifications was considered and reported in the next section.

References

[1] D.K. Bora, A. Braun, E.C. Constable, “In rust we trust”. Hematite – the prospective inorganic backbone for artificial photosynthesis, Energy Environ. Sci., 6 (2013) 407-425.

[2] M.J. Katz, S.C. Riha, N.C. Jeong, A.B.F. Martinson, O.K. Farha, J.T. Hupp, Toward solar fuels Water splitting with sunlight and rust, Coordination Chemistry Reviews 256 (2012) 2521- 2529.

[3] A. Duret, M. Gratzel, Visible Light-Induced Water Oxidation on Mesoscopic r-Fe2O3 Films Made by Ultrasonic spray pyrolysis, J. Phys. Chem. B 109 (2005) 17184-17191.

[4] D.K. Bora, A. Braun, S. Erat, A.K. Ariffin, R. Löhnert, K. Sivula, J.r. Töpfer, M. Grätzel, R. Manzke, T. Graule, Evolution of an oxygen near-edge X-ray absorption fine structure transition in the upper Hubbard band in α-Fe2O3 upon electrochemical oxidation, The Journal of Physical Chemistry C, 115 (2011) 5619-5625.

[5] R.R. Rangaraju, K.S. Raja, A. Panday, M. Misra, An investigation on room temperature synthesis of vertically oriented arrays of iron oxide nanotubes by anodization of iron, Electrochimica Acta, 55 (2010) 785-793.

[6] I. De Graeve, H. Terryn, G.E. Thompson, Influence of heat transfer on anodic oxidation of aluminium, Journal of Applied Electrochemistry, 32 (2002) 73-83.

[7] E.A. Garcla, Dynamical diffusion model to simulate the oxide crystallization and grain growth during oxidation of zirconium at 573 and 623 K, Journal of Nuclear Materials DOI (1995) 299-304.

[8] X.-w. Wei, C.-y. Chen, Influence of oxidation heat on hard anodic film of aluminum alloy, Transactions of Nonferrous Metals Society of China, 22 (2012) 2707-2712.

[9] S.R. Morrisons, The Chemical Physics of surface, Plenum Press New York and London.

[10] A. Saijo, K. Murakami, M. Hino, T. Kanadani, Effect of Environmentally Friendly Anodization on the Mechanical Properties and Microstructure of AZ91D Magnesium Alloy, Materials Transactions, 49 (2008) 903-908.

[11] A. Braun, K. Sivula, D.K. Bora, J. Zhu, L. Zhang, M. Grätzel, J. Guo, E.C. Constable, Direct Observation of Two Electron Holes in a Hematite Photoanode during Photoelectrochemical Water Splitting, The Journal of Physical Chemistry C, 116 (2012) 16870-16875.

[12] K. Gajda-Schrantz, S. Tymen, F. Boudoire, R. Toth, D.K. Bora, W. Calvet, M. Gratzel, E.C. Constable, A. Braun, Formation of an electron hole doped film in the alpha-Fe2O3 photoanode upon electrochemical oxidation, Phys Chem Chem Phys, 15 (2013) 1443-1451.

[13] A. Braun, Q. Chen, D. Flak, G. Fortunato, K. Gajda-Schrantz, M. Grätzel, T. Graule, J. Guo, T.W. Huang, Z. Liu, Iron resonant photoemission spectroscopy on anodized hematite points to electron hole doping during anodization, ChemPhysChem, 13 (2012) 2937-2944.

[14] M. Sugiyama, K. Fujii, S. Nakamura, Solar to Chemical Energy Conversion: Theory and Application, Springer2016.

[15] S. Heiroth, R. Frison, J.L. Rupp, T. Lippert, E.J.B. Meier, E.M. Gubler, M. Döbeli, K. Conder, A. Wokaun, L.J. Gauckler, Crystallization and grain growth characteristics of yttria-stabilized zirconia thin films grown by pulsed laser deposition, Solid State Ionics, 191 (2011) 12-23.

[16] K. Maabong, Y. Hu, A. Braun, A.G. Machatine, M. Diale, Influence of anodization time on the surface modifications on α-Fe2O3 photoanode upon anodization, Journal of Materials Research, 31 (2016) 1580-1587.

[17] K. Maabong, A.G. Machatine, Y. Hu, A. Braun, F.-J. Nambala, M. Diale, Morphology, structural and optical properties of iron oxide thin film photoanodes in photoelectrochemical cell: Effect of electrochemical oxidation, Physica B: Condensed Matter, 480 (2016) 91-94.

[18] K.F. McCarty, Inelasticlight scattering in Fe203- phonon and magnon scattering, Solid State Communications, 68 (1988.) 799-.2,.

[19] J. Joy, J. Mathew, S.C. George, Nanomaterials for photoelectrochemical water splitting–review, International Journal of Hydrogen Energy, DOI (2018).

[20] V.D. Mote, Y. Purushotham, B.N. Dole, Williamson-Hall analysis in estimation of lattice strain in nanometer-sized ZnO particles, Journal of Theoretical and Applied Physics, 6 (2012) 1-8.

[21] S.-H. Shim, T.S. Duffy, Raman spectroscopy of Fe2O3 to 62 GPa, American Mineralogist, 87 (2001) 318–326.

[22] R. Cuscó, N. Domènech-Amador, T. Hatakeyama, T. Yamaguchi, T. Honda, L. Artús, Lattice dynamics of a mist-chemical vapor deposition-grown corundum-like Ga2O3 single crystal, Journal of Applied Physics, 117 (2015) 185706.

[23] E. Smith, G. Dent, Modern Raman spectroscopy-A practical approach, John Wiley & Sons Ltd, England, 2005.

[24] M. Yang, D. Huang, P. Hao, F. Zhang, X. Hou, X. Wang, Study of the Raman peak shift and the linewidth of light-emitting porous silicon, Journal of Applied Physics, 75 (1994) 651-653.

[25] S.-H. Shim, T.S. Duffy, Raman spectroscopy of Fe2O3 to 62 GPa, American Mineralogist, 87 (2002) 318-326.

[26] Y.W. Phuan, E. Ibrahim, M.N. Chong, T. Zhu, B.-K. Lee, J.D. Ocon, E.S. Chan, In situ Ni-doping during cathodic electrodeposition of hematite for excellent photoelectrochemical performance of nanostructured nickel oxide-hematite p-n junction photoanode, Applied Surface Science, 392 (2017) 144-152.

[27] D.K. Bora, A. Braun, R. Erni, G. Fortunato, T. Graule, E.C. Constable, Hydrothermal Treatment of a Hematite Film Leads to Highly Oriented Faceted Nanostructures with Enhanced Photocurrents, Chemistry of Materials, 23 (2011) 2051-2061.

Part B: Influence of exposure time on the changes in surface structural properties of hematite upon anodization

4. 2B.1 Materials and method

Inspired by the findings in Part A, the study was extended to examine the influence of exposure time on the morphological changes induced on the surface of hematite upon anodization. For that purpose, a second batch of samples was prepared following the same method employed in the Part A. In this case, a constant anodic potential of 700 mV vs the Ag/AgCl electrode was applied under illumination for various times of 1, 10 and 900 min. The structural properties and surface morphology of the films were characterized by XRD, FESEM and AFM.

4. 2B.2 Results and discussion

XRD diffraction patterns of the pristine and anodized films were analyzed and presented in Figure 4-7. The XRD diffractograms were indexed to polycrystalline hematite [JCPDS #89-0599]. Similarly, the expanded XRD patterns of the (012), (104) and (110) peaks showed decreasing peak linewidth upon anodization, which signified increased crystallite size in the treated thin films. The extracted FWHM values and the corresponding average crystallites size are presented in Table 4-3. Similarly, the crystallite size increased from ~ 31 nm (pristine) to 38 nm for the film exposed to PEC environment for 60 s. The crystallites size increased with increase in the exposure time to 39 nm and 44 nm for films anodized for 10 and 900 min, respectively. The estimated average crystallite size lies within the same range as those for the nanostructures subjected to 500 mV for 60 s, regardless of the difference in the applied anodic potential and exposure time. No clear correlation between the applied anodic potential and crystallites size was detected. The dislocation density δ, which represents the density of defects or imperfections in the film was estimated according to the following equation, $\delta = 1/D^2$ [1], where D is the average crystallite size. The calculated values of δ for all the films are also given in Table 4-3. Dislocation density exhibit a

decreasing trend with increasing anodization time, which suggested decrease in concentration of dislocation lines per volume on the lattice and hence better crystallization. Usually, enhanced crystallinity favors charge separation and transfer as well as light absorption, while defect sites generally act as recombination centers for photogenerated electrons and holes [2].

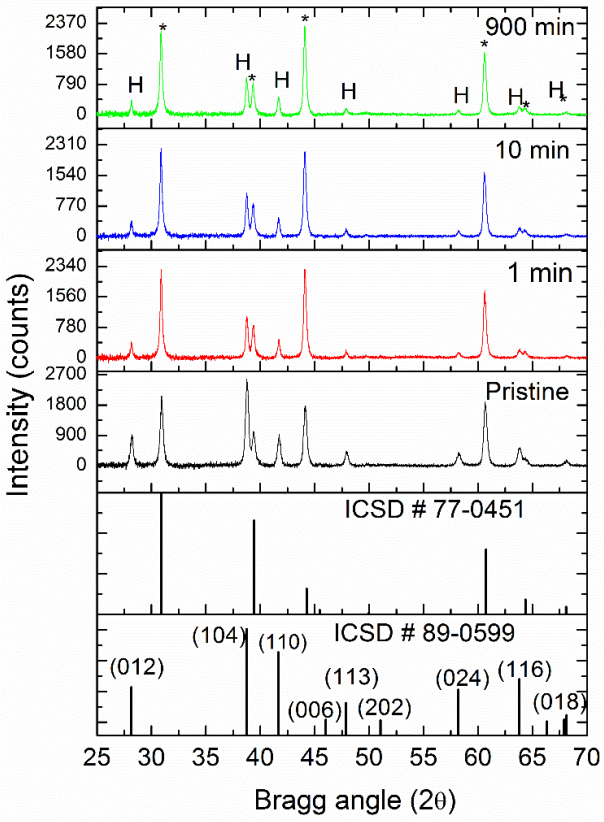

Figure 4-7: XRD diffraction of pristine and anodized α-Fe_2O_3 films (marked with H) deposited on F:SnO_2 substrates. The peaks marked with (*) corresponds to SnO_2 originating from the substrate. The standard powder pattern of α-Fe_2O_3 [JCPDS #89-0599] and SnO_2 [ICSD #77-0451] are also included [3].

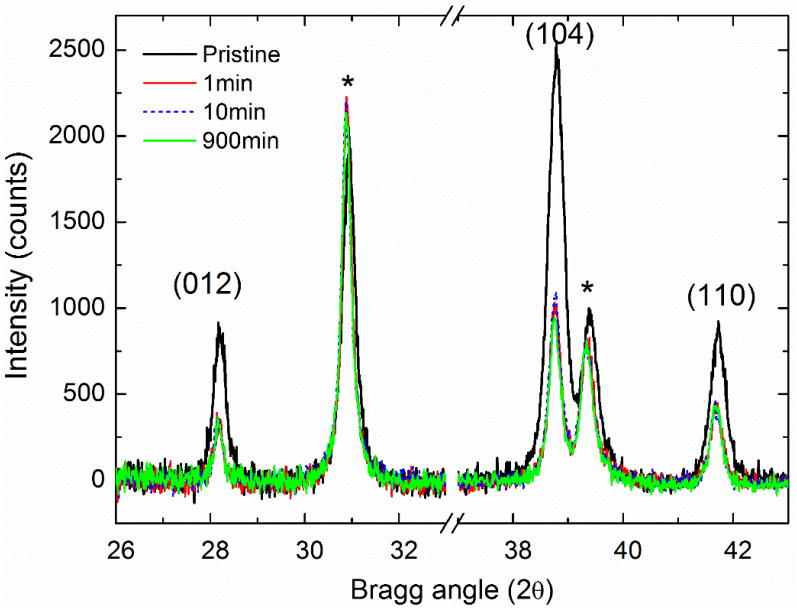

(A)

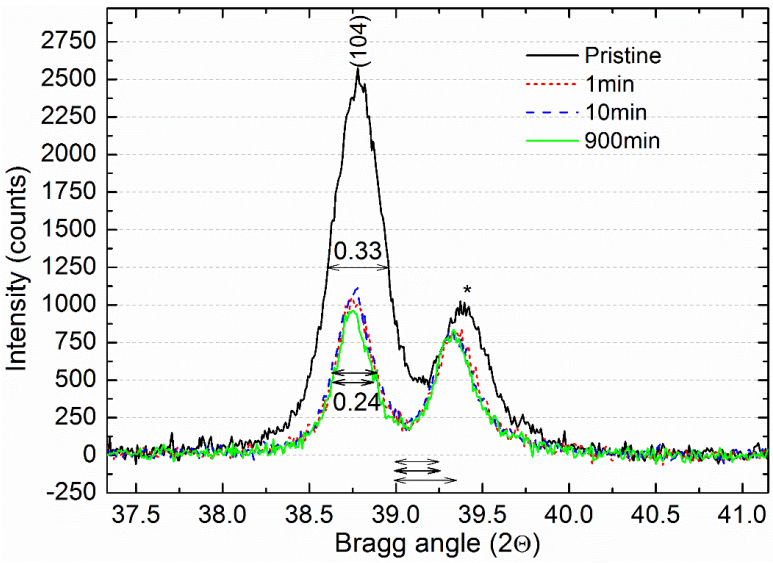

(B)

Figure 4-8: Expanded view of XRD patterns of the main characteristic peaks of hematite (A) and that of (104) peak (B), clearly showing decreasing peak linewidth upon anodization [3].

Table 4-3: A presentation of the linewidths (FWHM), average crystallites size (D) and the dislocation density (δ) of the α-Fe_2O_3 nanoparticles before and after electrochemical oxidation in 1M KOH at 700 mV at various anodization times [3].

Anodization time (minutes)	FWHM (2θ)			Crystallite size (nm)	Dislocation density, δ (10^{10})
	(012)	(104)	(110)	XRD	
0	0.324	0.331	0.34	31	0.00100
1	0.261	0.271	0.28	38	0.00069
10	0.247	0.26	0.27	39	0.00066
900	0.224	0.24	0.24	44	0.00052

The analysis of surface morphology by AFM was carried out and the results obtained as presented in Figure 4-9. The 2D and 3D AFM images revealed formation of well crystalline spherical nanoparticles. Before anodization, the nanoparticles in hematite appeared invisible on the substrate probably due to loosely attached hematite grains on the substrate surface [4]. The poor-adherence was confirmed by the maximum height of the particles in the pristine film as compared to anodized films. Clearly, after just 60 s, the nanoparticles became visible on the surface. The AFM data provide significant support that the particle size increases upon anodization. The particle size increased from ~ 58 nm for the pristine film to 88 and 149 nm for the films treated for 1 min (60s) and 900 min, respectively. The root-mean-square (rms) surface roughness of the samples was extracted from AFM data and presented against anodization time in Figure. 4-10. The pristine films surface exhibits rms roughness of ~ 49.4 nm. However, a rapid decrease in the rms value was observed upon anodization as clearly depicted in Figure. 4-10. The rms value decreased as the anodization time increased and was ascribed to smoothening of the surface upon anodization. The smoothening of the films' surface upon anodization is in agreement with the visual observations made by other researchers [5].

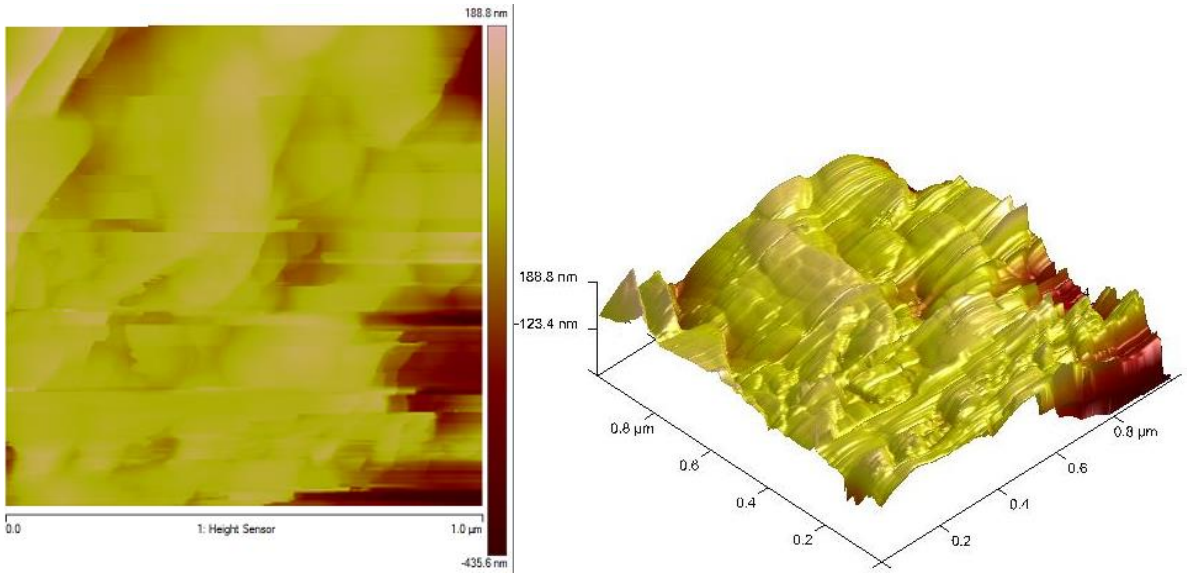

A: Pristine

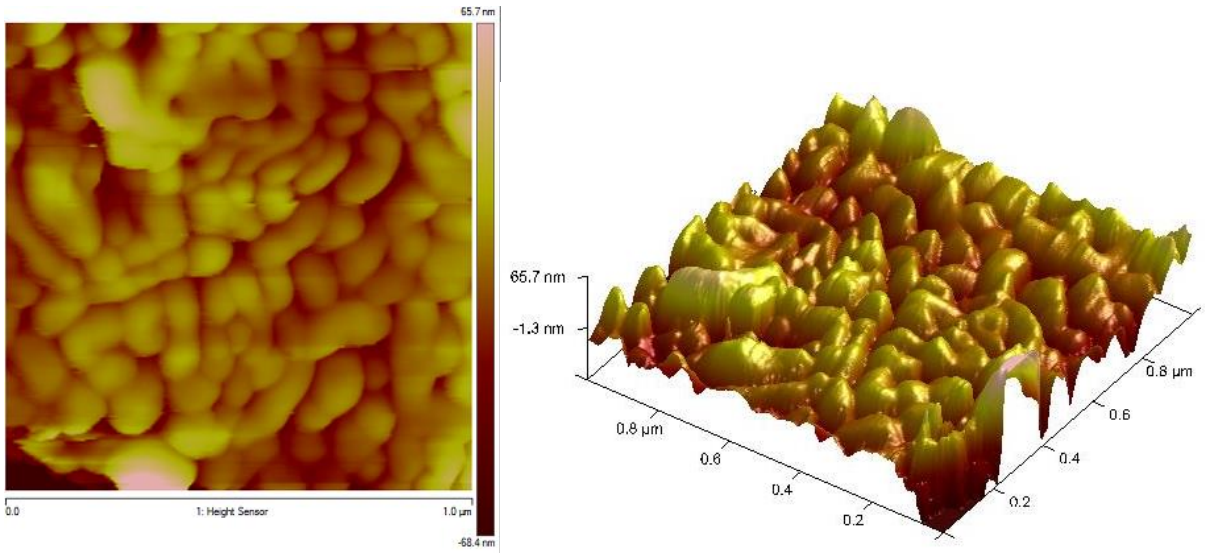

B: 1 min

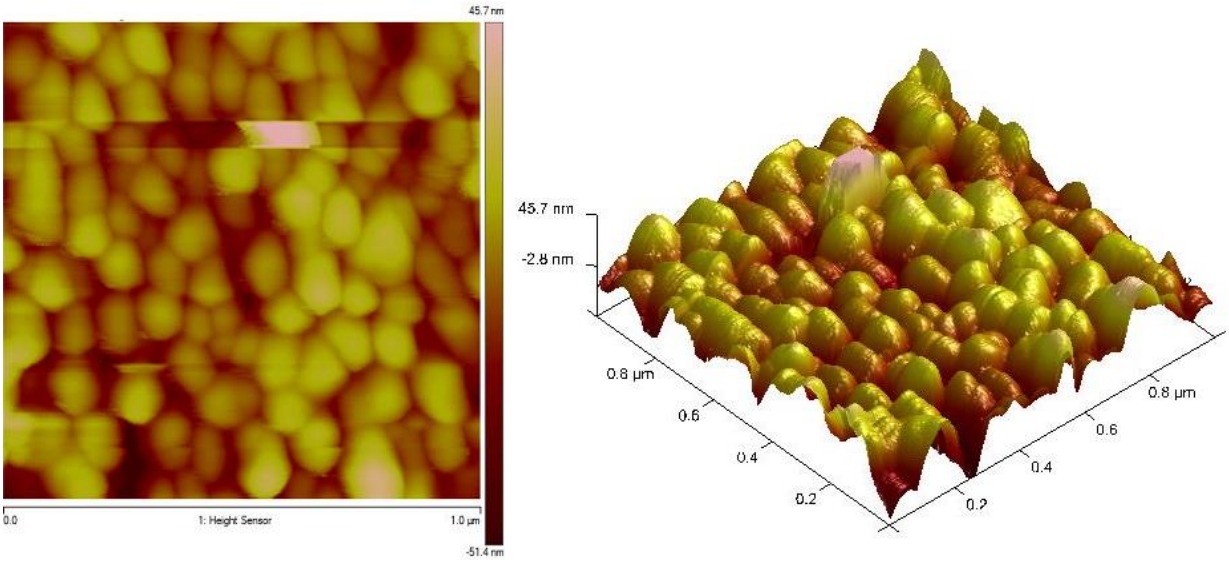

C: 10 min

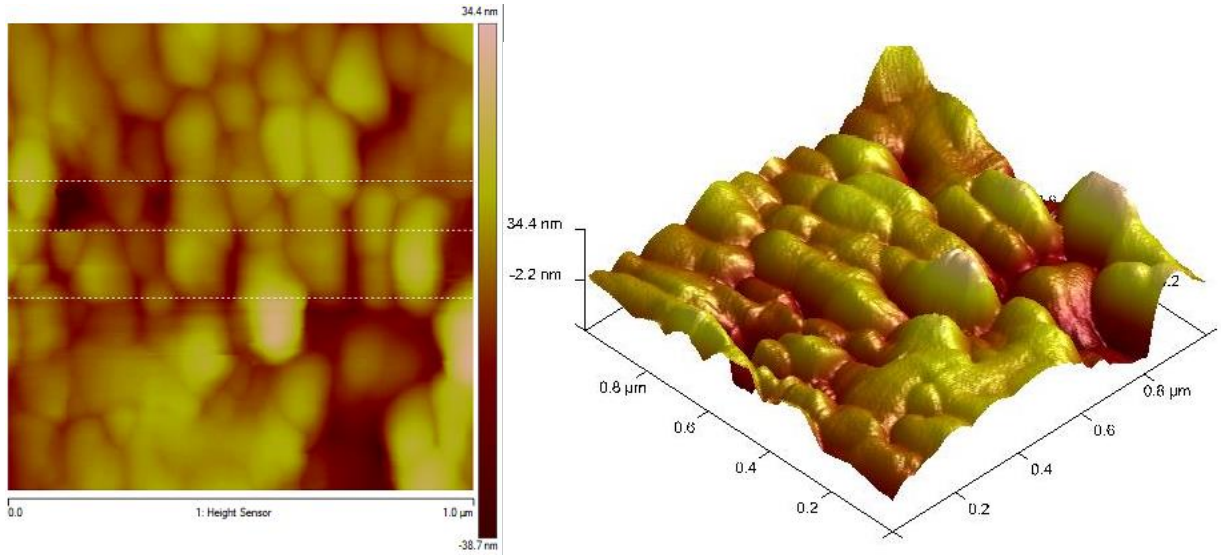

D: 900 min

Figure 4-9: Top-view 2D and 3D AFM images of pristine and anodized α-Fe_2O_3 nanostructures in 1M KOH under illumination, at 700 mV for various times [3].

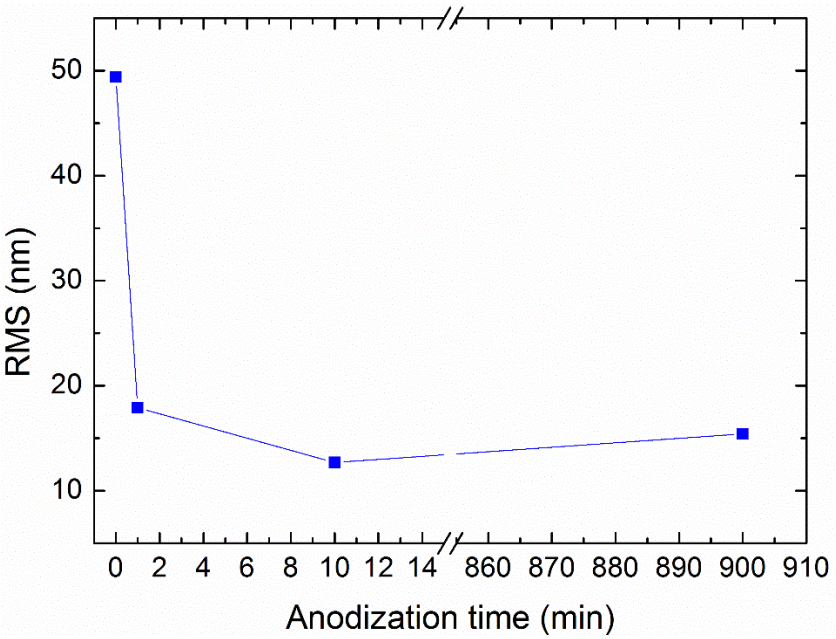

Figure 4-10: The root-mean-square (RMS) surface roughness versus anodization time for α-Fe_2O_3 films anodized at 700 mV vs Ag/AgCl [3].

The increase in the particle size was further confirmed by electron microscopy imaging in Figure 4-11. Before anodization, the surface was covered with small-sized and roughly-shaped spherical nanoparticles. The surface was enhanced as the particle size increased upon anodization. The particle size increased from ~ 58 nm for pristine sample to ~ 153.5 nm for the film treated for 900 min. A summary of SEM and AFM analyses is presented in Table 4-4. Generally, the size of the nanoparticles on the surface increased with increasing exposure time, without losing shape. The increase in crystal size and film thickness is expected to impact on the charge transportation and thus water oxidation due to increased charge diffusion distance to the surface in hematite. Also, excessive increase in the particle could affect the structure of the nanoparticle interior and surface or even cause phase distortion.

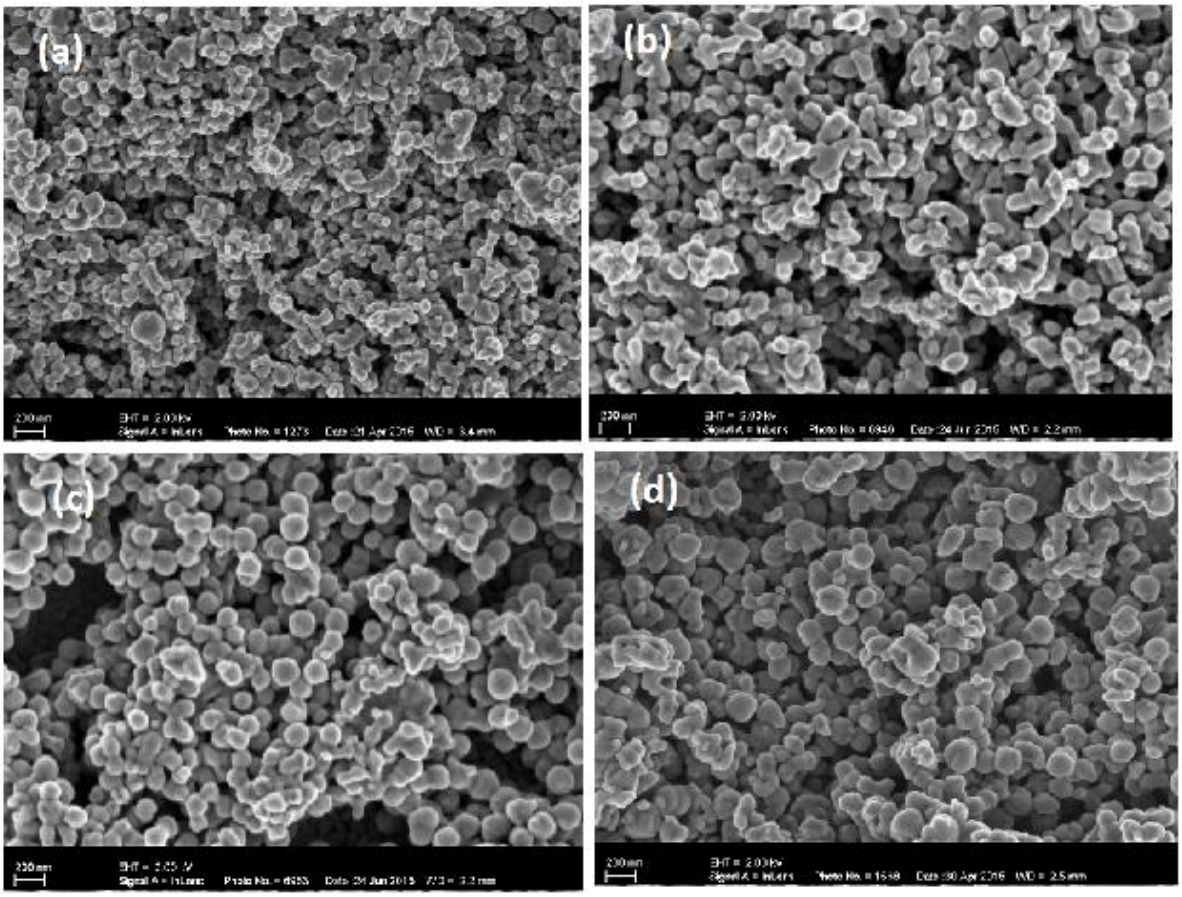

Figure 4-11: FE-SEM images of α-Fe_2O_3 nanostructure before (a) and after anodization (b: 1min, c: 10 min, d: 900 min) at 700 mV, under illumination [3].

Table 4-4: A comparison of the particle size and the surface roughness of the hematite nanoparticles before and after electrochemical oxidation at 700 mV for various anodization times [3].

Anodization time (min)	Particle size (nm)		RMS (nm)
	FESEM	AFM	
0	57.9	58.4	49
1	88.3	88.0	18
10	121.8	117.3	13
900	153.5	149.5	15

Figure 4-12 shows typical UV-vis absorption spectra of the synthesized nanostructures. The absorption edge of the anodized films slightly shifted to more extended wavelength region, suggesting narrowing of the band gap upon exposure to PEC environment. Decrease in the band gap energy as a result of increasing particle size has been reported in literature [6]. The onset absorption band occurred at ~ 592 nm for pristine nanoparticles, and ~ 598 and 596 for films anodized at 1 min and 900 min (longest time) respectively. A slight red shift to longer wavelength in anodized films was expected due to enhanced surface and enlarged particles upon anodization.

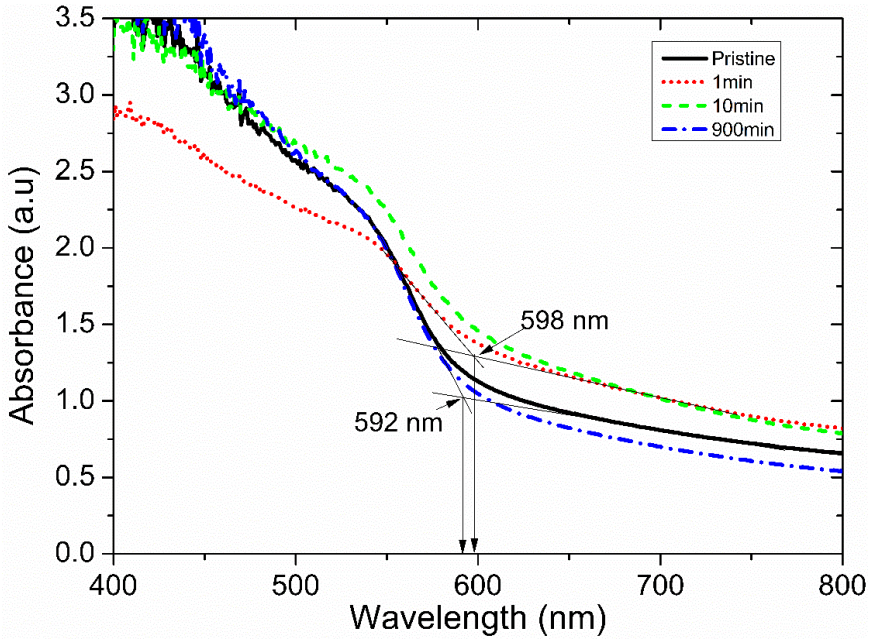

Figure 4-12: UV-vis spectra of α-Fe_2O_3 films before and after anodization at 700 mV for various times[3].

Grain growth mechanism upon anodization of a pre-existing oxide film is a complex process although one may establish a number of analogies with anodization of metal surfaces. For example, previous studies suggested different potential factors that may cause an increase surface temperature leading to grain growth upon anodization such as oxidation reaction heat and convectional joule heating (electrical power dissipated) of the electrolyte [7] and the heating of the

oxide under illumination [8]. In addition, because of the mismatch between the photon absorption depth and minority carrier diffusion length, the majority of the photogenerated electron and hole pairs recombine non-radiatively before contributing to water splitting. Thus, the energy released from nonradiative recombination may heat the oxide surface. Probably grain growth occurs due to Ostwald ripening; whereby large particles grow at the expense of small particles as a result of increase in temperature at the surface. Smaller grains exhibit large surface free energy and higher solubility than larger ones and tend to agglomerate, coalesce and slowly dissolve and re-deposit on the large crystals and simultaneously grain growth occurs [9, 10].

Furthermore, during the re-crystallization and re-growth processes, the number of grain boundaries decrease due to the annihilation of small grains by grain boundary migration [11]. The rotation-coalescence of neighboring grains results in the elimination of grain boundaries between them and supposedly grain growth. Within this framework, grain growth upon anodization may reduce recombination of the photogenerated holes and electrons and subsequently enhance the PEC performance of the photoelectrode [12]. Conversely, excessive grain growth may impact negatively on the production of photocurrent as the hole diffusion distance increases resulting in the loss of the charge carriers through recombination in the bulk.

Braun *et al.*, reported enhanced current density on anodized hematite nanostructures upon anodization at 200 and 600 mV vs the Ag/AgCl electrode in 1M KOH for 24 h [13]. Though the enhancement on the photocatalytic process was attributed to hole doping upon anodization, the contribution of the enhancement of the surface cannot be ruled out. However, the influence of the observed modifications on the microstructural features at the hematite surface upon anodization on the photocurrent production and long term stability of the films, awaits confirmation and further investigations are part of future work. In the present work the focus was only on the microstructural

properties as the first step in a systematic study on the effect electrochemical oxidation of hematite photoanode.

4. 2B.3. Concluding remarks

The influence of exposure time on the surface crystallographic structure modifications on the hematite (α-Fe_2O_3) photoanode upon anodization in a PEC cell was investigated. The hematite thin films prepared by an economic and facile dip coating method were anodized in 1M KOH at an anodic potential of 700 mV versus a Ag/AgCl electrode under simulated illumination. The crystallite size increased from ~ 31 nm for nanoparticles in the pristine state to ~ 38 and 44 nm after anodization for 1 min (shortest time) and 900 min (longest time), respectively, without losing the shape. A positive correlation between anodization time and nanoparticles size was observed from FEG-SEM and AFM analyses. The nanoparticle size increased with increasing anodization time from ~58 nm in the pristine state to ~ 154 nm for films exposed for 900 min; longer exposure time to PEC conditions resulted in larger grains. The increase in size of the nanoparticles during anodization is expected to improve the conductivity of α-Fe_2O_3 due to reduced recombination rate of holes and electrons as a result of improvement on the surface of the electrode during anodization. The density of dislocations, surface roughness and possibly grain boundaries decreased. The findings in this section may provide valuable information towards its performance in a PEC cell.

References

[1] Y. Caglar, S. Ilican, M. Caglar, F. Yakuphanoglu, J. Wu, K. Gao, P. Lu, D. Xue, Influence of heat treatment on the nanocrystalline structure of ZnO film deposited on p-Si, Journal of Alloys and Compounds, 481 (2009) 885-889.

[2] J. Joy, J. Mathew, S.C. George, Nanomaterials for photoelectrochemical water splitting–review, International Journal of Hydrogen Energy, DOI (2018).

[3] K. Maabong, Y. Hu, A. Braun, A.G. Machatine, M. Diale, Influence of anodization time on the surface modifications on α-Fe2O3 photoanode upon anodization, Journal of Materials Research, 31 (2016) 1580-1587.

[4] S.-C. Shei, S.-J. Chang, P.-Y. Lee, Rinsing effects on successive ionic layer adsorption and reaction method for deposition of ZnO thin films, Journal of the Electrochemical Society, 158 (2011) H208-H213.

[5] D.K. Bora, A. Braun, S. Erat, A.K. Ariffin, R. Löhnert, K. Sivula, J.r. Töpfer, M. Grätzel, R. Manzke, T. Graule, Evolution of an oxygen near-edge X-ray absorption fine structure transition in the upper Hubbard band in α-Fe2O3 upon electrochemical oxidation, The Journal of Physical Chemistry C, 115 (2011) 5619-5625.

[6] D.A. Wheeler, G. Wang, Y. Ling, Y. Li, J.Zhanghng, Nanostructured hematite: synthesis, characterization, charge carrier dynamics, and photoelectrochemical properties, Energy Environ. Sci., 5 (2012) 6682–6702.

[7] X.-w. Wei, C.-y. Chen, Influence of oxidation heat on hard anodic film of aluminum alloy, Transactions of Nonferrous Metals Society of China, 22 (2012) 2707-2712.

[8] S.R. Morrisons, The Chemical Physics of surface, Plenum Press New York and London.

[9] E.A. Garcla, Dynamical diffusion model to simulate the oxide crystallization and grain growth during oxidation of zirconium at 573 and 623 K, Journal of Nuclear Materials DOI (1995) 299-304.

[10] M.R. Belkhedkar, A.U. Ubale, Preparation and Characterization of Nanocrystalline α-Fe2O3 Thin Films Grown by Successive Ionic Layer Adsorption and Reaction Method.pdf, International Journal of Materials and Chemistry 5(2014) 109-116.

[11] F. Li, L. Zhang, R.M. Metzger, On the Growth of Highly Ordered Pores in Anodized Aluminum Oxide, Chem. Mater., 10 (1998,) 2470-2480.

[12] S.H. Tamboli, G. Rahman, O.-S. Joo, Influence of potential, deposition time and annealing temperature on photoelectrochemical properties of electrodeposited iron oxide thin films, Journal of Alloys and Compounds, 520 (2012) 232-237.

[13] A. Braun, Q. Chen, D. Flak, G. Fortunato, K. Gajda-Schrantz, M. Gratzel, T. Graule, J. Guo, T.W. Huang, Z. Liu, A.V. Popelo, K. Sivula, H. Wadati, P.P. Wyss, L. Zhang, J. Zhu, Iron resonant photoemission spectroscopy on anodized hematite points to electron hole doping during anodization, Chemphyschem : a European journal of chemical physics and physical chemistry, 13 (2012) 2937-2944.

[14] K. Gajda-Schrantz, S. Tymen, F. Boudoire, R. Toth, D.K. Bora, W. Calvet, M. Gratzel, E.C. Constable, A. Braun, Formation of an electron hole doped film in the alpha-Fe2O3 photoanode upon electrochemical oxidation, Phys Chem Chem Phys, 15 (2013) 1443-1451.

[15] V.M. Arutyunyan, Physical properties of the semiconductor-electrolyte interface, Sov. Phys. Usp, 32 (1989) 521-540.

Chapter 5

Nanostructured Ti-doped hematite photoanodes for hydrogen generation via solar-driven water splitting

5.1 Introduction

Hematite has been studied as a prospective photoanode material for water oxidation using sunlight, owing to its outstanding stability and an ideal bandgap of ~2.1 eV and its capability to absorb a substantial portion of the visible spectrum [1-4]. However, its photoelectrochemical performance is still hindered by rapid charge recombination as a consequence of poor conductivity, short diffusion length of holes, low carrier mobility and short lifetime of the carriers [1-4]. Despite the significant efforts to alleviate the drawbacks, reported efficiencies are still much lower than the predicted theoretical value and hence the need to strive for optimization of preparation techniques and conditions and keep exploring for more robust strategies [5].

Elemental doping remains one prime and simple strategy to enhance PEC performance of hematite by tuning the bulk and surface electronic properties of the photoanode material, which are different. Also, the structural changes associated with doping effects could influence the charge transport and charge transfer properties of the material. Ti is one common dopant found to tune bulk properties of hematite efficiently. Various experimental works employing different techniques such as pulse laser deposition (PLD), hydrothermal, dip coating, spray pyrolysis, reactive magnetron sputtering, in situ solid-state reaction method have been reported [6-11]. This study utilizes advantages of chemical solution methods to synthesize Ti-doped hematite photoelectrodes at low cost. Dip coating and spin coating methods are cost-effective and straightforward sol-gel techniques, offering control over desired electrode thickness due to layer

by layer growth mechanism. Also, deposition is done at low temperatures. Doping with various elements can be achieved by merely adding dopant precursors into the precursor solution. To date, reports on the synthesis of nanostructured Ti-doped hematite by these two methods for application in solar water splitting are very limited.

5.2 PART A: Nanostructured hematite thin films prepared by dip coating

The dip coating technique involves immersing a substrate in a solution bath for a sufficient time, to ensure the deposition of the solvent on the substrate, and withdrawal from the solution bath at a prescribed speed. The film thickness is determined by the withdrawal speed and viscosity of the solvent. At higher withdrawal speed, the viscous drag force becomes large resulting in a large amount of the solution moving upwards with the substrate, resulting in the formation of a thicker film. Hu *et al*. demonstrated the potential use of this technique for a large area (10 x 10 cm) Si-doped hematite photoanode [12].

5.2A.1 Materials and methods

Synthesis of the photoelectrode

Hematite thin films were deposited by dip coating of iron oleate precursor prepared following the same procedure as described in Figure 4-1. During deposition, the substrate was immersed into the solution for 30s then withdrawn at 130 mm/min. The iron-oleate films were dried at 70 °C on a hot plate followed by annealing in the furnace at 550 °C for 30 min, at heating and cooling rate of 10 °C/min. The deposition, drying and heat treatment steps were repeated in this order, for each layer at a time, to obtain an optimized three-layered hematite thin film. To study the effect of doping, a small controlled amount of titanium (IV) butoxide $(TiBuO)_4$ was added to obtain Ti doping levels of 0.5, 1 and 2 at%.

Characterization

The phase composition and crystallinity of the thin films were analyzed by powder X-ray diffraction with Cu-Kα radiation. The surface morphology was examined using field emission scanning electron microscopy (FESEM, Carl Zeiss AG) operating at 2 kV. Raman spectra of the films were obtained in 180° backscattering geometry with a 0.15 mW Ar+ laser at a wavelength of 514.5 nm, focused on a spot size of about 5 μm. The UV–Vis spectra of the films were measured by a Cary 5E UV/VIS/NIR spectrophotometry, using a blank FTO substrate as a reference. Photoelectrochemical measurements of the hematite film photoanodes were carried out using a similar three-electrode configuration shown in Figure 4-2, with a platinum plate counter electrode and Ag/AgCl/ saturated KCl reference electrode in contact with 1 M KOH (pH~13.6) electrolyte. The photocurrent measurement was recorded from – 300 to + 700 mV vs the Ag/AgCl electrode, swept at a rate of 10 mV s^{-1} in darkness and under simulated light (100 mW cm^{-2}) using a 300W xenon lamp (LOT Oriel). The measured potential vs Ag/AgCl (sat. KCl) reference electrode potential was converted to RHE scale, following the Nernst equation [13],

$$V_{RHE} = V_{Ag/AgCl} + 0.059pH + V^{0}_{Ag/AgCl} \qquad (5.1)$$

Where $V^{0}_{Ag/AgCl} = 0.1976$ V at 25 °C. To monitor the amount of oxygen (O_2) and hydrogen (H_2) evolved from the reaction between the α-Fe_2O_3 and H_2O, a closed cycle re-circulating gas chromatography (GC) system equipped with a custom-built, sealed electrochemical cell developed at Empa was used.

5. 2A.2 Results and discussion

Because the film thickness plays a vital role in the performance of the photoelectrode, optimization of the thickness was carried out. The pristine photoanodes with 1 to 5 layers were synthesized at the optimized temperature of 550 °C. All the films were characterized by XRD and UV-vis

spectroscopy to understand the role of film thickness on the degree of crystallinity and photoabsorption of the fabricated hematite thin films (Figure 5-1).

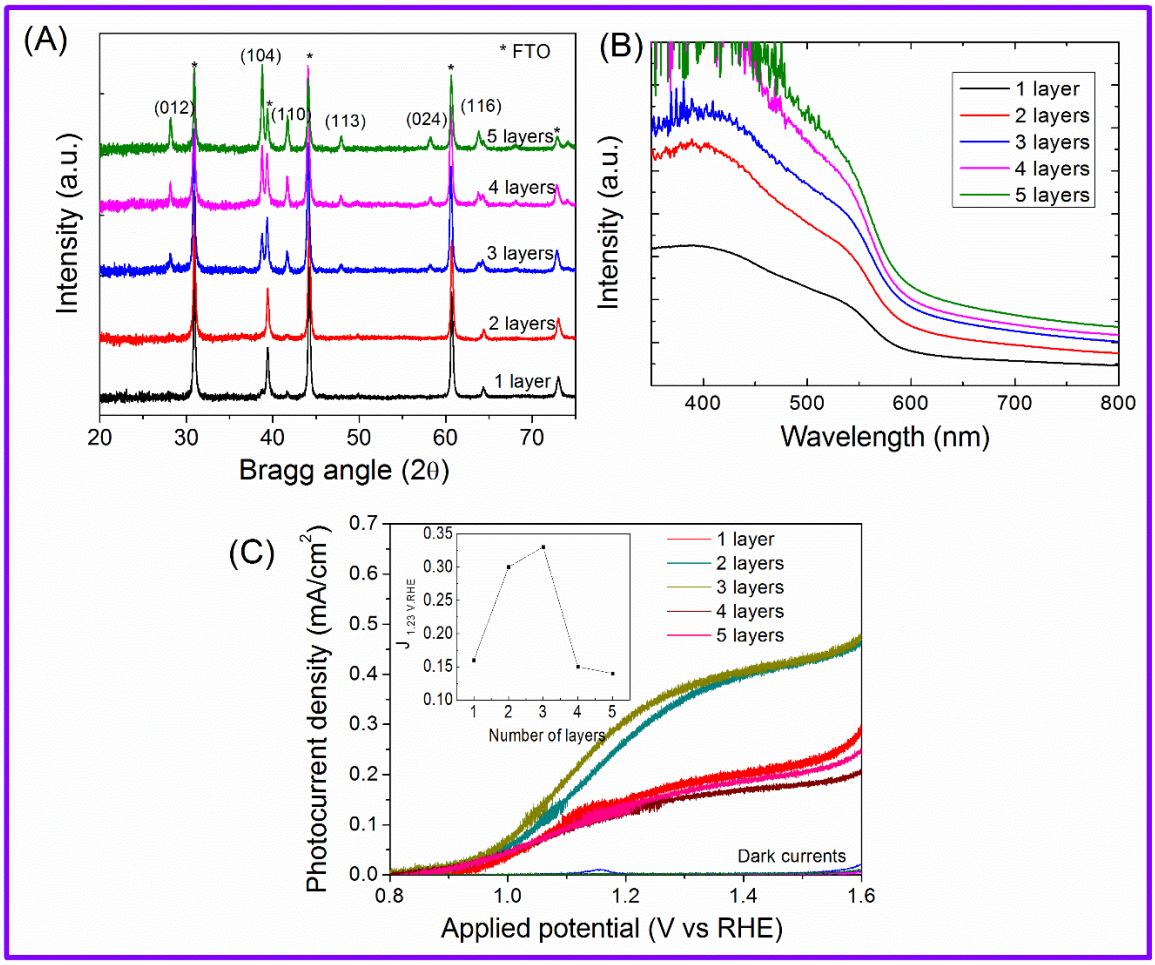

Figure 5-1: (A) XRD patterns, (B) absorption spectra and (C) photocurrent-potential curves of α-Fe_2O_3 thin films of different thicknesses. The inset in (C) shows the photocurrent density at 1.23 V vs RHE against number of layers.

The results demonstrated that photoabsorption and crystallinity of the samples increased with an increase in the film thickness as expected. The enhancement in crystallinity was attributed to increase in the particles size as the thickness increases. In spite of the improvement in photocurrent and crystallinity of the films with film thickness, the photocurrent increased with increasing film thickness up to three layers and decreased afterwards (Figure 5-1(C)). The three-layered thin film

thus showed the best photocatalytic activity. A decrease in PEC performance with film thickness in α-Fe_2O_3 has been previously reported in the literature [14, 15]. Generally, the photocatalytic activity corresponds to the charge transport and separation efficiency, which are related to the space charge layer in the material [16].

For the best optical efficiency, a thicker electrode is essential for efficient light absorption. However, as the film thickness increases and become comparable to the space charge layer width, additional current cannot be produced since most of the charge carriers generated outside the space charge layer recombine and consequently the photocurrent decreases [4, 17, 18]. Also, thicker electrodes result in high recombination of the photogenerated electron-hole pairs due to longer diffusion distance and hence charger resistance in the bulk. On the other hand, while a thinner electrode is necessary for efficient hole collection at the electrode-electrolyte interface [19, 20], ultrathin thickness limit efficient photon absorption, particularly for indirect materials with low absorption coefficient such as hematite.

Figure 5-2 shows electron microscope micrographs of the optimized pristine and Ti-doped hematite films. The results demonstrated the formation of porous spherical-shaped individual nanoparticles of high crystallinity. The cross-sectional view of the pristine film in Figure 5-2 (A) revealed an average film thickness of 505.3 nm. The pristine film exhibited nanoparticles of average diameter of ~ 60-70 nm. The nanoparticles remained almost unchanged after doping except for a slight decrease in size. The particle size decreased to average diameter in the range of ~ 50 - 35 nm (Figure 5-2 (B)). The decrease in particle size is expected to facilitate charge transport and separation in the photoanodes due to reduced charge diffusion distances and high surface area to volume ratio [21]. The drawback with the dip coating process is the formation of non-uniform

and cracked surface which usually provide more recombination sites for the electron and hole pairs as it was observed on SEM micrographs and presented in Figure 5-2 (C).

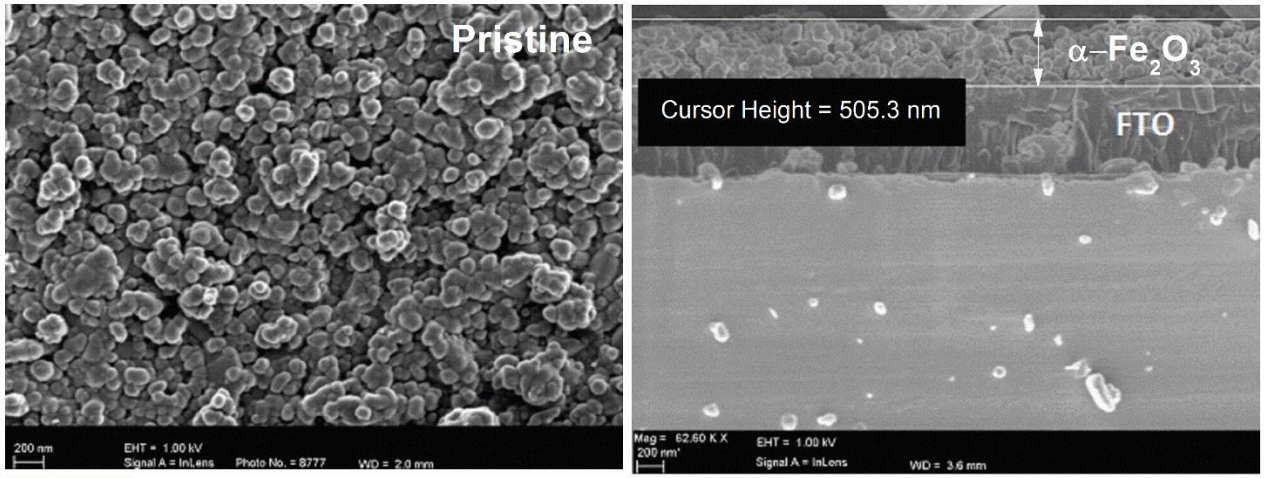

(A)

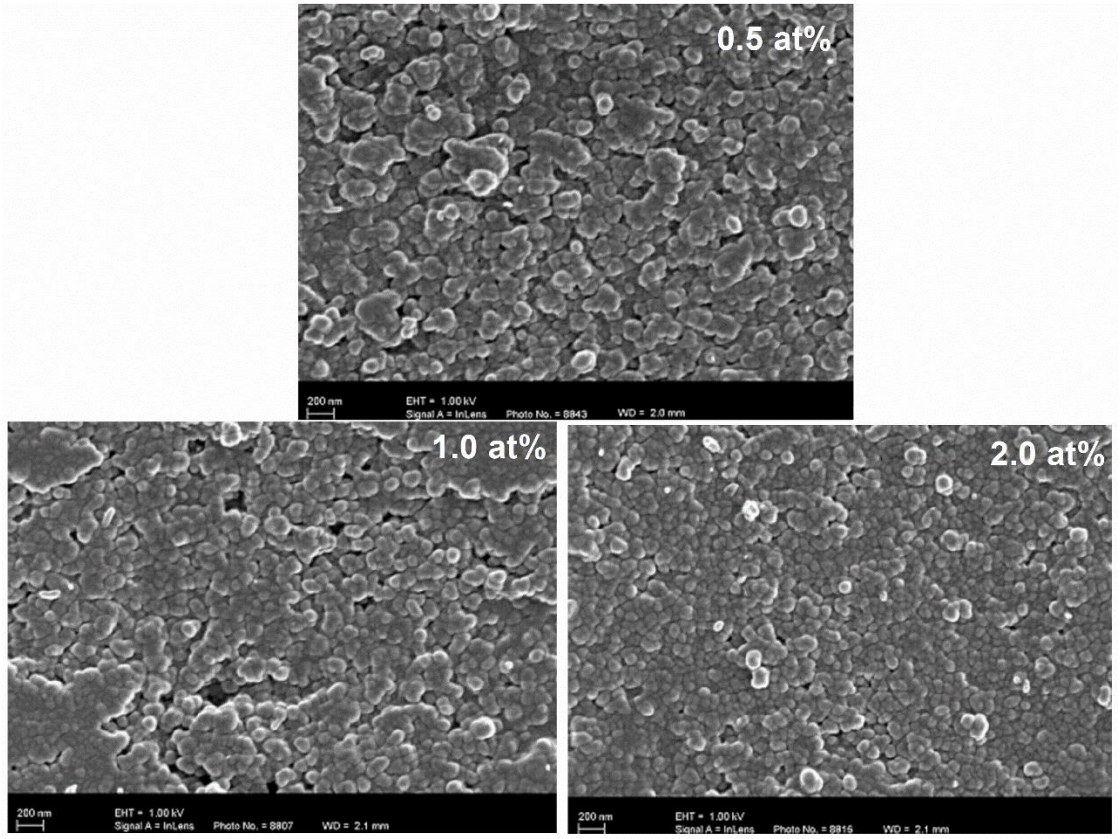

(B)

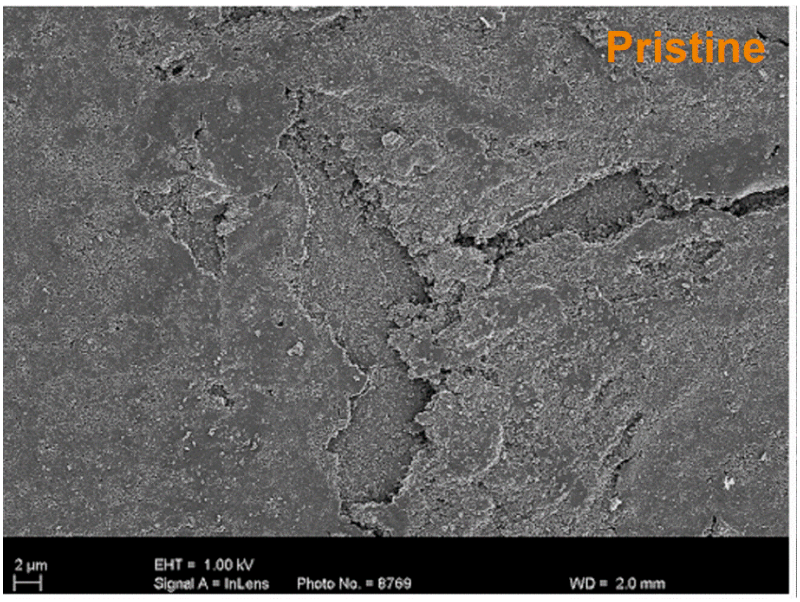

(C)

Figure 5-2: FESEM micrographs of (A) pristine and (B) Ti-doped α-Fe_2O_3 nanoparticles. The scale bar equal to 200 nm. (C) Low magnification micrograph of the pristine film revealing uneven surface [22].

X-ray diffraction analysis was carried out to examine the phase purity and crystallinity of the synthesized α-Fe_2O_3 photoanodes. Typical XRD diffraction in Figure 5-3, observed at 2θ values of ~ 24°, 33°, 36°, 41°, 49° and 62° respectively, correspond to the (012), (104), (110), (113), (024), (116) crystal planes in hematite [23-25]. The peak intensity distribution was indexed to polycrystalline hematite with rhombohedral structure (JCPDS no.73–0603). The average crystallite size ranged from 37 nm for the pristine film to 35.5, 32 and 30.5 nm for 0.5at%, 1at% and 2 at% doped films, respectively. The decrease in crystallite size was confirmed by peak broadening, especially in the 1at% and 2 at% doped films in Figure 45-3 (B). No extra peaks corresponding to Ti impurities or other phases were observed in all the films. The sharp peaks identified by (*) originated from the FTO substrate (cassiterite, phase, [JCPDS: 77-0451]).

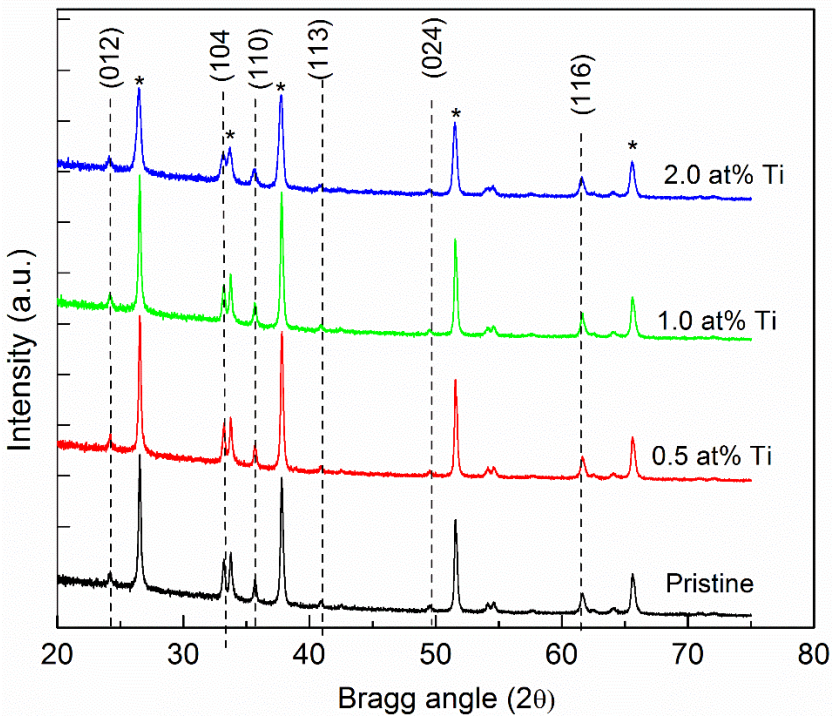

(A)

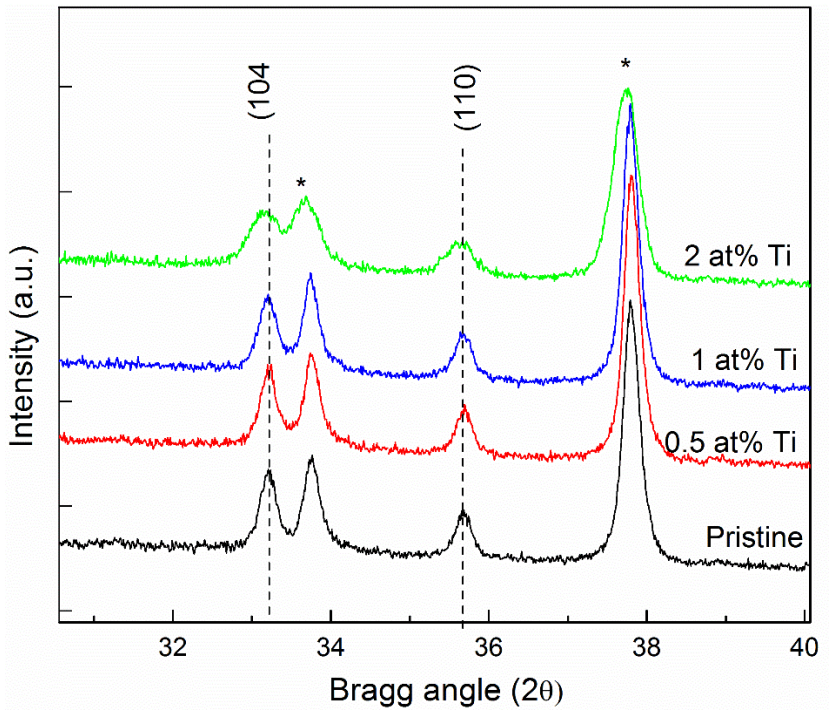

(B)

Figure 5-3: XRD patterns of dip-coated pristine and Ti-doped hematite nanostructured films. (B) expanded view of the patterns [22].

Typical UV-visible absorption spectra of the synthesized α-Fe_2O_3 nanoparticles were recorded and presented in Figure 5-4. The nanoparticles exhibit strong absorption band centred near the UV region (350-450 nm), associated with ligand-to-metal charge transfer (direct transition) of O^{2-} (2p) $\rightarrow$ Fe^{3+} (3d). In the visible region (580-800 nm) absorption is very weak due to indirect forbidden charge transition Fe^{3+} (3d) $\rightarrow$ (3d) [26]. All the films exhibit an overlapping cut-off wavelength at ~597 nm which corresponds to an energy band gap of 2.1 eV, in agreement with reported values in literature. The main advantage of doping is the fine tuning of the band gap. A narrow bandgap is essential for achieving high STH efficiencies. Large band gap fails to absorb the required intensities of visible spectrum energy to efficiently split the water [27]. Doping with Ti has been found to introduce impurity donor levels in the band structure, narrowing the band gap [28]. These donor levels usually act as effective photoelectron providers as relatively little energy is required to set the donor electrons in these levels free into the conduction band and participate in conductivity, enhancing PEC activity. From the UV-vis optical absorption measurement, the optical band gap of the semiconductor can be estimated from the absorption coefficient according to the Tauc mode [29, 30];

$$\alpha = \frac{B(h\nu - E_g)^n}{h\nu} \tag{5.2}$$

where,

$$B = \left[\frac{e^2}{nch^2 m_e^*}\right](2m_r)^{3/2} \tag{5.3}$$

Here, B is a constant, $h\nu$ is photo energy, n depends on the nature of optical transition: n = ½ and 2 for allowed direct and indirect transitions, respectively. E_g is the optical band gap and, m_r and m_e^* are respectively the reduced and effective masses of the charge carriers.

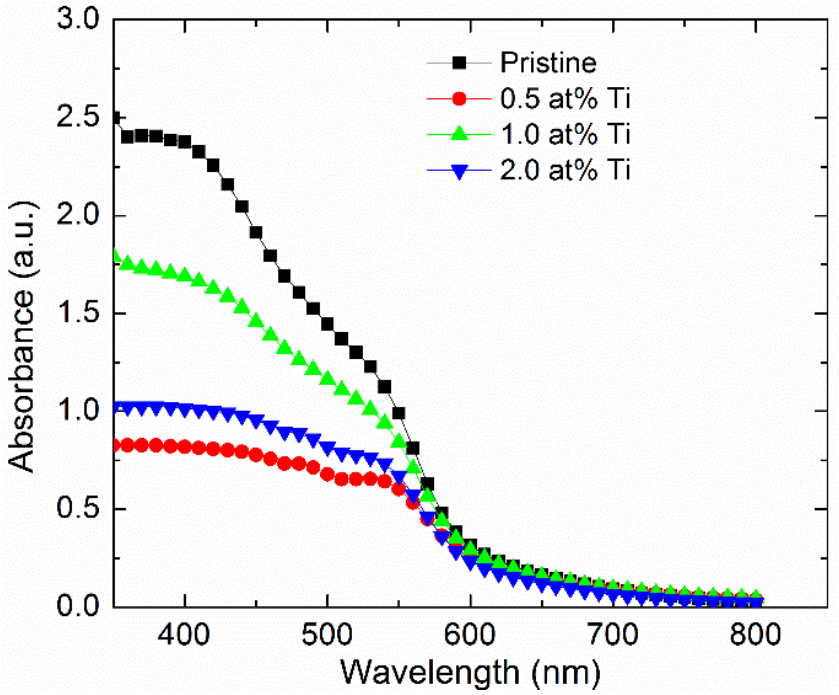

(A)

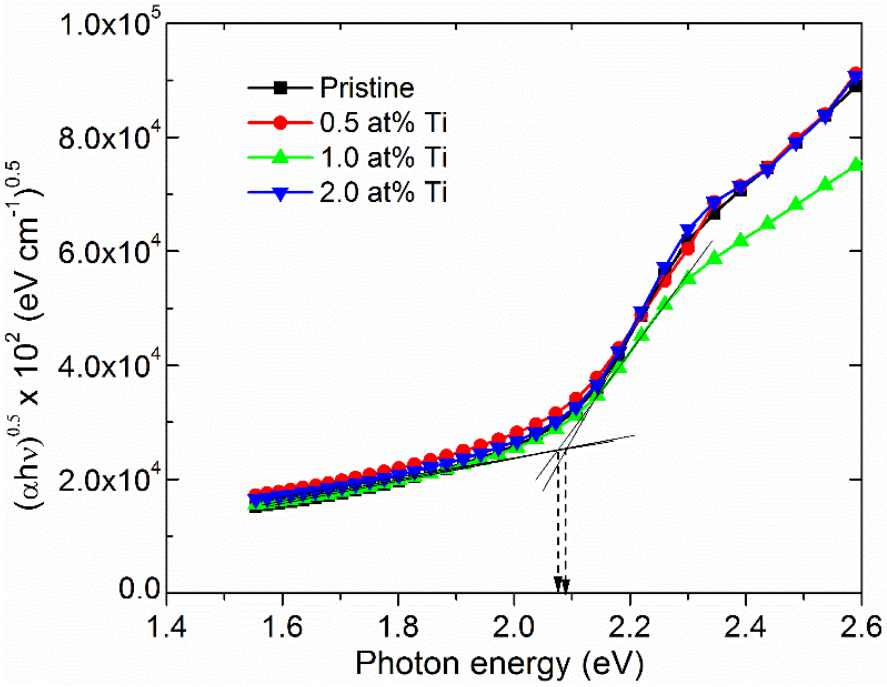

(B)

Figure 5-4: (A) UV-vis absorption spectra of pristine and Ti-doped α-Fe_2O_3 nanostructures. (B) The estimated optical band gap of the nanostructures from Tauc model [22].

Hematite exhibit an indirect band gap where a band minimum appears at a different momentum away from the Γ-point in the crystal Brillouin zone, and therefore its indirect phonon-assisted band gap energy was determined by extra-plotting the linear fit to the plot of $(\alpha h\nu)^{1/2}$ *versus* the photon energy to zero absorbance. The estimated energy gap of pristine nanoparticles was obtained as 2.09 ± 0.02 eV. No significant changes in energy band gap observed after doping with Ti.

The photoanodes were tested for their photoelectrochemical water oxidation performance in darkness and under simulated illumination. Figure 5-5 shows photoelectrochemical characteristics of the Ti-doped α-Fe_2O_3 photoanodes compared to pristine electrodes. The inset in Figure 5-5 (A) shows the photograph of the pristine hematite photoanode. The optimized pristine film of average thickness of *ca*. 505 nm produced a photocurrent density of 0.32 mA/cm^2 at 1.23 V *vs* RHE. The low current density was ascribed to high recombination of the photogenerated electron and hole pairs as electron scanning of the films revealed cracks and folding, which provide recombination sites for photogenerated charge carriers [14, 15].

Prepared under the same conditions, Ti-hematite films showed enhanced PEC performance compared to the pristine film. Substitution of Ti^{4+} at Fe^{3+} ion lattice sites increased current density to a maximum value of ~ 0.72 mA/cm^2 at 1.23 V *vs* RHE for the film doped with 1.0 at% Ti, which is 2-fold increase compared to the pristine photoanode. Furthermore, the J^2-V curves [31] in Figure 5-5 (B) shows significantly reduced photocurrent onset potentials in modified electrodes compared to the pristine film, which is clearly illustrated in the inset. Reduced onset potential in doped α-Fe_2O_3 nanoparticles is probably due to faster hole injection kinetics as a result of improve charge properties in doped photoanodes [32]. Also, the plateau current density at 1.45 V *vs*. RHE increased from ~ 0.43 mA/cm^2 for pristine to ~ 0.95 mA/cm^2 for 1 at% Ti-hematite photoanode. The value of the plateau current density reflects the probability of photogenerated holes reaching

the semiconductor-electrolyte interface and taking part in water oxidation, at such high potentials [33]. At higher potentials, band bending and the electric field in the space charge region increase and facilitate charge separation within the region. The greater the bending, the faster the electron-hole pair separation occurs, and the number of photogenerated holes reaching the interface increases.

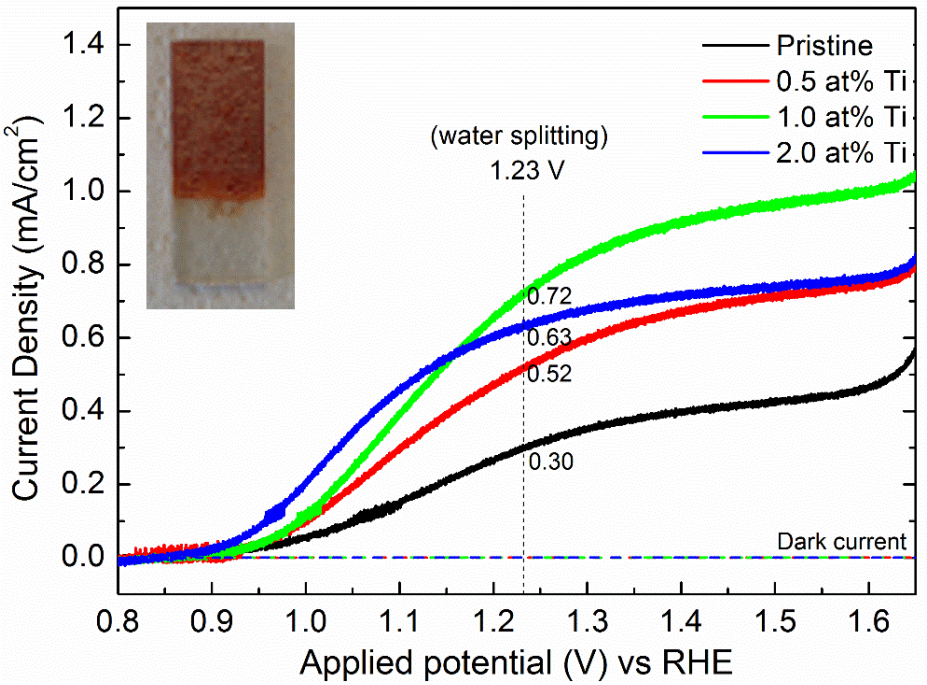

(A)

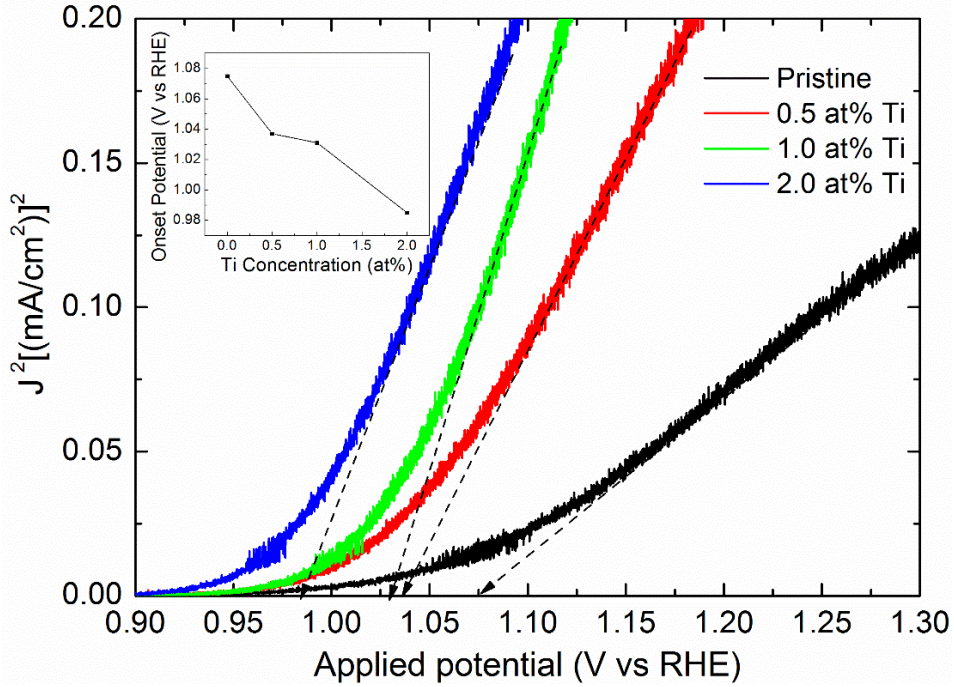

(B)

Figure 5-5: Photoelectrochemical characteristics of dip-coated nanostructured pristine and Ti: α-Fe_2O_3 photoelectrodes in contact with 1 M KOH. Inset of (A) shows the photograph of the pristine photoanode. (B) The estimated photocurrent onset potential. Inset shows current onset potential as a function of Ti concentration [22].

Ti doping improves electron conductivity as a result of increased donor concentration and improved mobility [18]. Conductivity is linearly dependent on mobility, carrier density and donor density through the following expression, $\sigma = ne\mu$ where e, n and μ respectively denote electron charge, charge density and mobility. The increased conductivity is beneficial for transportation of photogenerated electrons to the FTO substrate, and thus reducing charge recombination. Also, theoretical studies based on DFT have demonstrated that Ti doping can potentially improve dispersion of the *E-k* band in the conduction band as compared to the pristine hematite [34, 35]. More dispersed band lines in the conduction band indicate reduced electron effective mass and therefore improved electron mobility and hence increased conductivity [34, 35]. Curvature of the

electronic energy bands is related to charge carrier effective mass as (assuming parabolic bands) [36];

$$m^*(k) = \left(\frac{h}{2\pi}\right)^2 \left[\frac{d^2E(\vec{k})}{dk^2}\right]^{-1} \quad (3)$$

Relatively small curvature implies greater carrier effective mass and consequently small charge carrier mobility according to the relation $\mu = e\tau / m^*$, where τ corresponds to charge relaxation time. Although the current density still increased compared to the pristine and the 0.5 at% Ti-doped film (~ 0.52 mA/cm^2), it decreased to 0.63 mA/cm^2 with 2 at% doping level. At higher concentrations, Ti^{4+} would have defect scattering/recombination properties and suppresses charge separation efficiency, lowering the photocurrent [37]. Moreover, *ab initio* calculations on electron transport in doped hematite suggested that Ti^{4+} dopant has empty 3d orbital favouring electron trapping, which may affect the electron hopping mode for electron transport along iron atoms, especially at lower doping concentration level and thus inhibit photoactivity [38]. Saroj *et al*. also noted that at considerable Ti doping concentrations, above optimal level, the donor density decreases as excess electrons localize on Ti^{4+} ions, decreasing the electric field within the space charge layer resulting in low field-driven charge separation [39].

Photocurrent is generally a reflection of water oxidation by the photogenerated holes. To measure the potential of the fabricated photoanodes for hydrogen generation, the amount of hydrogen and oxygen generated in the PEC cell was monitored in a specifically designed gas-tight Teflon PEC cell with gas chromatography (GC-2014, Shimadzu) at EMPA (Figure 5-6). Due to the unavailability of the equipment, only the pristine and the best performing doped (1 at% Ti) photoelectrodes were examined.

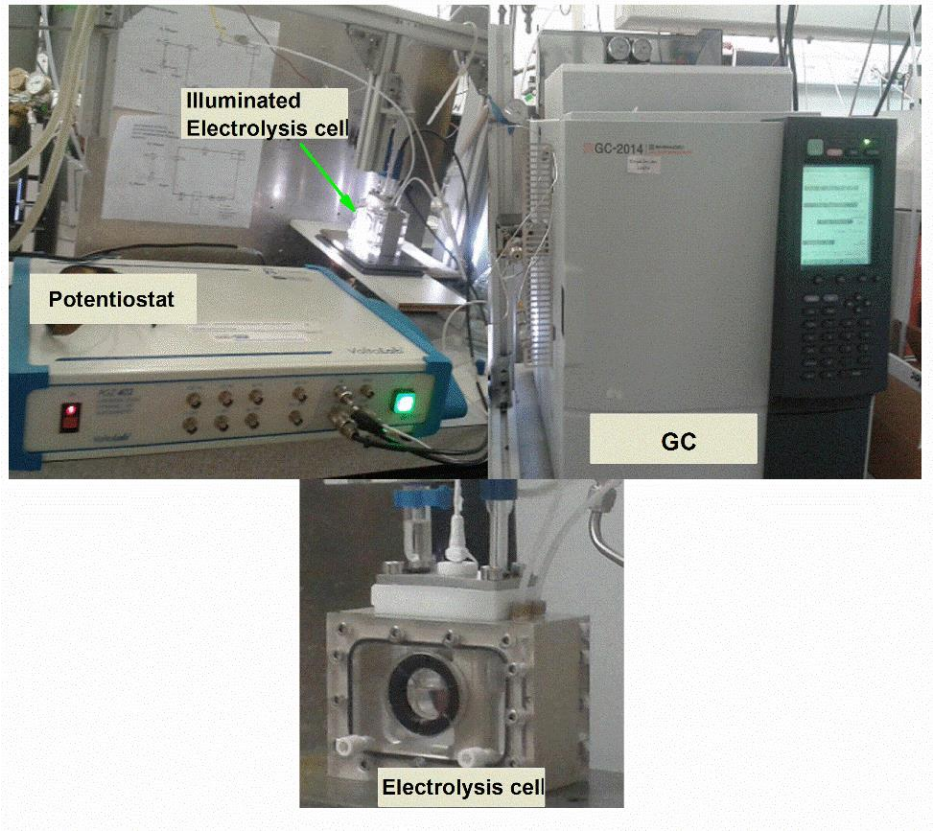

Figure 5-6: Photographs of the Gas Chromatograph system used for gas analysis. The photo was taken at EMPA.

Figure 5-7 shows the amount of O_2 and H_2 evolved measured during 175 min. Indeed, the figure confirms the production of solar fuels via water splitting. The amount of H_2 evolved was significantly increased upon doping with 1 at%, which renders Ti-doped photoanodes prepared by dip coating promising for solar water splitting despite the low current density produced with relative to other methods, e.g., hydrothermal [7]. The enhancement in H_2 evolution was associated with improved hole transfer kinetics at the hematite-electrolyte interface as a result of Ti doping.

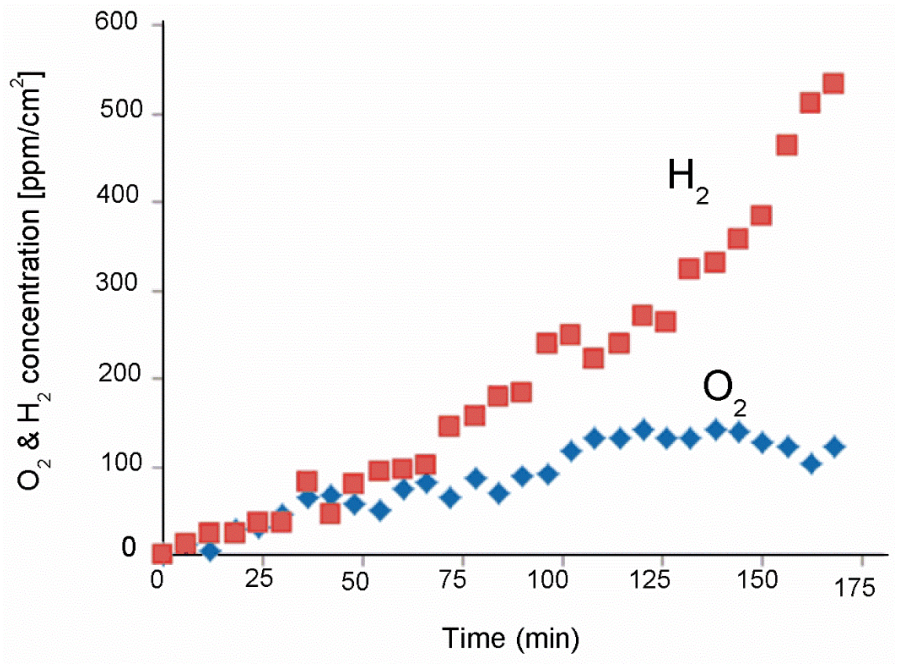

(A)

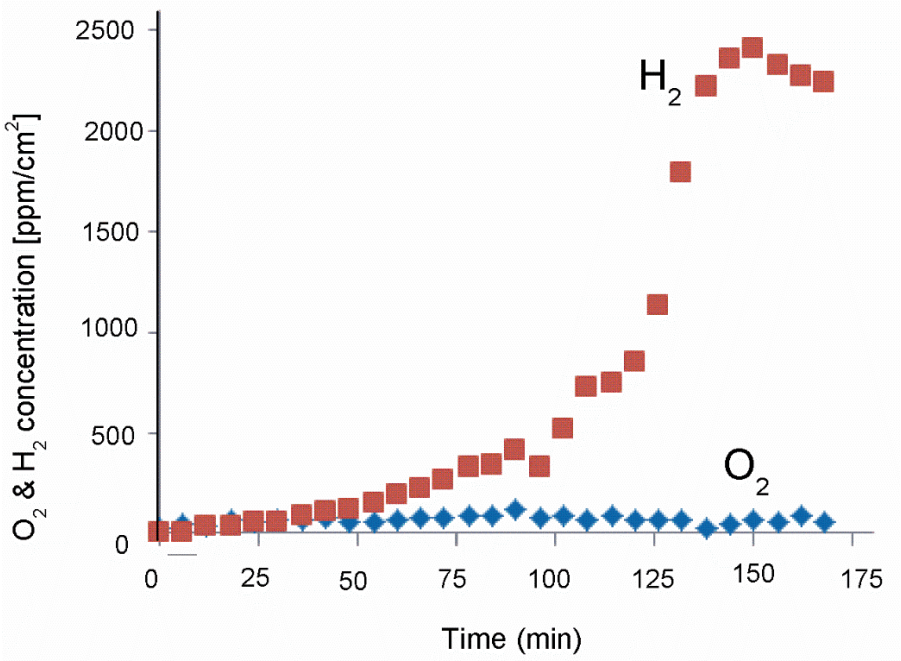

(B)

Figure 5-7: O_2 and H_2 evolution as a function of time at +1.3 V vs. Ag/AgCl electrode for pristine (A) and 1 at% Ti-doped (B) α-Fe_2O_3 photoanodes [22].

5. 2A.3 Concluding remarks

Pristine and Ti-doped hematite nanostructured films were prepared via a simple and cost-effective dip coating method and investigated for photoelectrochemical water splitting application. Doping with Ti was effective in improving the photoelectrochemical properties of the hematite photoanode. The PEC analysis of the films showed enhanced photoactivity and a significant cathodic shift in onset potential upon Ti doping, suggestive of improved charge separation and hence enhanced charge transfer at the semiconductor-electrolyte interface. The current density increased from 0.32 mA/cm^2 for pristine photoanode to the maximum value of ~ 0.72 mA/cm^2 at 1.23 V vs RHE upon doping with 1 at% Ti doping level and slightly more hydrogen was evolved from the same photoanode compared to pristine hematite. The drawback of the dip coating process is excess hematite that peels off during annealing resulting in an uneven surface and high density of surface structural defects like cracks in the film which provide recombination sites for the electron and hole pairs. As a result, the PEC performance obtained is low compared to values obtained by other techniques presented in Table 1.1 in Section 1.1

References

[1] Z. Lin, J. Wang, Low-cost nanomaterials toward greener and more efficient energy applications, Springer, Verlag London, 2014.

[2] J.Z. Zhang, Metal oxide nanomaterials for solar hydrogen generation from photoelectrochemical water splitting, MRS Bulletin 336 (2011) 48-55.

[3] K. Sivula, F. Le Formal, M. Gratzel, Solar water splitting: progress using hematite (alpha-Fe(2) O(3)) photoelectrodes, ChemSusChem, 4 (2011) 432-449.

[4] Y. Lin, G. Yuan, S. Sheehan, S. Zhou, D. Wang, Hematite-based solar water splitting: challenges and opportunities, Energy & Environmental Science, 4 (2011) 4862.

[5] P.S. Bassi, S.Y. Chiam, Gurudayal, J. Barber, L.H. Wong, Hydrothermal Grown Nanoporous Iron Based Titanate, Fe2TiO5 for Light Driven Water Splitting, ACS Applied Materials & Interfaces, 6 (2014) 22490-22495.

[6] S. Chatman, C.I. Pearce, R.K. M., Charge Transport at Ti-Doped Hematite (001)-Aqueous Interfaces, Chemistry of Materials, 27 (2015) 1665−1673.

[7] J. Deng, J. Zhong, A. Pu, D. Zhang, M. Li, X. Sun, S.-T. Lee, Ti-doped hematite nanostructures for solar water splitting with high efficiency, J. Appl. Phys., 112 (2012) 084312.

[8] T.S. Atabaev, N.H. Hong, Y.-H. Hwang, M. Ajmal, H.-K. Kim, Ti-doped hematite thin films for efficient water splitting, Appl. Phys. A 118 (2015) 1539-1542.

[9] J.A. Glasscock, P.R. Barnes, I.C. Plumb, N. Savvides, Enhancement of photoelectrochemical hydrogen production from hematite thin films by the introduction of Ti and Si, The Journal of Physical Chemistry C, 111 (2007) 16477-16488.

[10] C.J. Sartoretti, M. Ulmann, B. Alexander, J. Augustynski, A. Weidenkaff, Photoelectrochemical oxidation of water at transparent ferric oxide film electrodes, Chemical Physics Letters, 376 (2003) 194-200.

[11] C. Miao, T. Shi, G. Xu, S. Ji, C. Ye, Photocurrent enhancement for Ti-doped Fe2O3 thin film photoanodes by an in situ solid-state reaction method, ACS applied materials & interfaces, 5 (2013) 1310-1316.

[12] Y. Hu, D.K. Bora, F. Boudoire, F. Haeussler, M. Graetzel, E.C. Constable, A. Braun, A dip coating process for large area silicon-doped high performance hematite photoanodes, Journal Of Renewable And Sustainable Energy, 5 (2013).

[13] J. Wang, B. Feng, J. Su, L. Guo, Enhanced Bulk and Interfacial Charge Transfer Dynamics for Efficient Photoelectrochemical Water Splitting: The Case of Hematite Nanorod Arrays, ACS applied materials & interfaces, 8 (2016) 23143-23150.

[14] D.K. Bora, A. Braun, S. Erat, A.K. Ariffin, R. Löhnert, K. Sivula, J.r. Töpfer, M. Grätzel, R. Manzke, T. Graule, Evolution of an oxygen near-edge X-ray absorption fine structure transition in the upper Hubbard band in α-Fe2O3 upon electrochemical oxidation, The Journal of Physical Chemistry C, 115 (2011) 5619-5625.

[15] M. Rioult, H.l.n. Magnan, D. Stanescu, A. Barbier, Single crystalline hematite films for solar water splitting: Ti-doping and thickness effects, The Journal of Physical Chemistry C, 118 (2014) 3007-3014.

[16] M. Wang, X. Wu, K. Huang, Y. Sun, Y. Zhang, H. Zhang, J. He, H. Chen, J. Ding, S. Feng, Enhanced solar water-splitting activity of novel nanostructured Fe2TiO5 photoanode by electrospray and surface F-modification, Nanoscale, 10 (2018) 6678-6683.

[17] J.Y. Kim, G. Magesh, D.H. Youn, J.-W. Jang, J. Kubota, K. Domen, J.S. Lee, Single-crystalline, wormlike hematite photoanodes for efficient solar water splitting, Scientific Reports, 3 (2013) 2681.

[18] O. Zandi, A.R. Schon, H. Hajibabaei, T.W. Hamann, Enhanced Charge Separation and Collection in High-Performance Electrodeposited Hematite Films, Chem. Mater., 28 (2015) 765−771.

[19] H. Kim, J. Kim, E. Lee, D.-W. Kim, J.-H. Yun, J. Yi, Effect of the short collection length in silicon microscale wire solar cells, Applied Physics Letters, 102 (2013) 193904.

[20] R. Abea, Recent progress on photocatalytic and photoelectrochemical water splitting under visible light irradiation, Journal of Photochemistry and Photobiology C: Photochemistry Reviews 11 (2010) 179-209.

[21] R.R. Rangaraju, A. Panday, K.S. Raja, M. Misra, Nanostructured anodic iron oxide film as photoanode for water oxidation, Journal of Physics D: Applied Physics, 42 (2009) 135303.

[22] K. Maabong, A.G.J. Machatine, B.S. Mwankemwa, A. Braun, D.K. Bora, R. Toth, M. Diale, Nanostructured hematite thin films for photoelectrochemical water splitting, Physica B: Condensed Matter, 535 (2018) 67-71.

[23] A.J. Abel, I. Garcia-Torregrosa, A.M. Patel, B. Opasanont, J.B. Baxter, SILAR-Deposited Hematite Films for Photoelectrochemical Water Splitting: Effects of Sn, Ti, Thickness, and Nanostructuring, J. Phys. Chem. C, 119 (2015) 4454-4465.

[24] S. Kumari, A.P. Singh, Sonal, D. Deva, R. Shrivastav, S. Dass, V.R. Satsangi, Spray pyrolytically deposited nanoporous Ti4+ doped hematite thin films for efficient photoelectrochemical splitting of water, Int. J. Hydrogen Energy 35 (2010) 3985-3990.

[25] D.K. Bora, A. Braun, E.C. Constable, “In rust we trust”. Hematite – the prospective inorganic backbone for artificial photosynthesis, Energy Environ. Sci., 6 (2013) 407-425.

[26] R.M. Cornell, U. Schwertmann, The Iron Oxides: Structure, Properties, Occurances, and Uses, DOI (Wiley-VCH 2003).

[27] J. Joy, J. Mathew, S.C. George, Nanomaterials for photoelectrochemical water splitting–review, International Journal of Hydrogen Energy, DOI (2018).

[28] J. Velev, A. Bandyopadhyay, W. Butler, S. Sarker, Electronic and magnetic structure of transition-metal-doped α-hematite, Physical Review B, 71 (2005) 205208.

[29] N.M. Abdul Rashid, C. Haw, W. Chiu, N.H. Khanis, A. Rohaizad, P. Khiew, S. Abdul Rahman, Structural- and optical-properties analysis of single crystalline hematite (α-Fe2O3) nanocubes prepared by one-pot hydrothermal approach, CrystEngComm, 18 (2016) 4720-4732.

[30] V.C. Nelson, K.L. Starcher, Introduction to renewable energy, CRC press2015.

[31] J. Cao, T. Kako, N. Kikugawa, J. Ye, Photoanodic properties of pulsed-laser-deposited α-Fe2O3electrode, J. Phys. D: Appl. Phys., 43 (2010) 325101.

[32] P.S. Bassi, R.P. Antony, P.P. Boix, Y. Fang, J. Barber, L.H. Wong, Crystalline Fe2O3/Fe2TiO5 heterojunction nanorods with efficient charge separation and hole injection as photoanode for solar water oxidation, Nano Energy, 22 (2016) 310-318.

[33] S.D. Tilley, M. Cornuz, K. Sivula, M. Gratzel, Light-induced water splitting with hematite: improved nanostructure and iridium oxide catalysis, Angew. Chem. Int. Ed. , 49 (2010) 6405-6408.

[34] M.N. Huda, A. Walsh, Y. Yan, S.-H. Wei, M.M. Al-Jassim, Electronic, structural, and magnetic effects of 3d transition metals in hematite, J. Appl. Phys. , 107 (2010) 123712.

[35] H. Pan, X. Meng, J. Cai, S. Li, G. Qin, 4d transition-metal doped hematite for enhancing photoelectrochemical activity: theoretical prediction and experimental confirmation, RSC Advances, 5 (2015) 19353-19361.

[36] G. Burns, Solid Ptate Physics, Academic Press, New York, 1985.

[37] T.S. Atabaev, M. Ajmal, N.H. Hong, H.-K. Kim, Y.-H. Hwang, Ti-doped hematite thin films for efficient water splitting, Applied Physics A, 118 (2014) 1539-1542.

[38] P. Liao, M.C. Toroker, E.A. Carter, Electron transport in pure and doped hematite, Nano letters, 11 (2011) 1775-1781.

[39] S. Kumari, A.P. Singh, Sonal, D. Deva, R. Shrivastav, S. Dass, V.R. Satsangi, Spray pyrolytically deposited nanoporous Ti4+ doped hematite thin films for efficient photoelectrochemical splitting of water, Int. J. Hydrogen Energy, 35 (2010) 3985-3990.

Part B: Nanostructured hematite thin films prepared by spin coating

Spin coating is an economical and reproducible wet chemical technique for the synthesis of thin film electrodes with excellent uniformity. The controllable film thickness is determined by the spinning speed and viscosity of the precursor solution. During the deposition, some precursor is lost due to radial outflow caused by the centrifugal force. As a result, a thin film forms on the substrate, leading to the formation of small feature sized particles in the film. However, due to a constant radial distribution of the solvent on the substrate, a smooth and uniform film forms. Studies on hematite prepared by spin coating method are very limited in the literature. Souza *et al*. [1] and Shen et al. [2], respectively studied nanostructured Si-doped α-Fe_2O_3 and W-doped α-Fe_2O_3 nanorods prepared by the same technique. In this section, nanostructured Ti-doped α-Fe_2O_3 thin films obtained by spin-coating is reported, and a promising photocurrent density of ~ 1.84 mA cm^{-2} at 1.23 V *vs* RHE was achieved.

5. 2B.1 Materials and methods

Preparation of the electrodes

Pristine and Ti-α-Fe_2O_3 thin films were spin-coated on FTO coated glass substrates using the SM-180-BT SAWATEC spin coater. Pure iron nitrate was mixed with pre-heated oleic acid to make an iron oleate complex following the same method used for dip coating as presented in Figure 5-8. The FTO glass substrates were sonicated in a sequence of acetone, ethanol and deionized water (10 min each step), then dried with compressed nitrogen gas before use. During the deposition, small drops of the precursor were placed on the substrate and spun at 4000 rpm for 30s, at room temperature. The films were annealed in a furnace at 550 °C for 30 min at 10 °C/min heating and cooling rate. Optimized three-layers thin films were obtained by repeated deposition and annealing after each layer. Ti doping was achieved by adding a small amount of titanium (IV) butoxide to the FeOOH precursor to obtain concentration levels of 0.5, 1 and 2 at%.

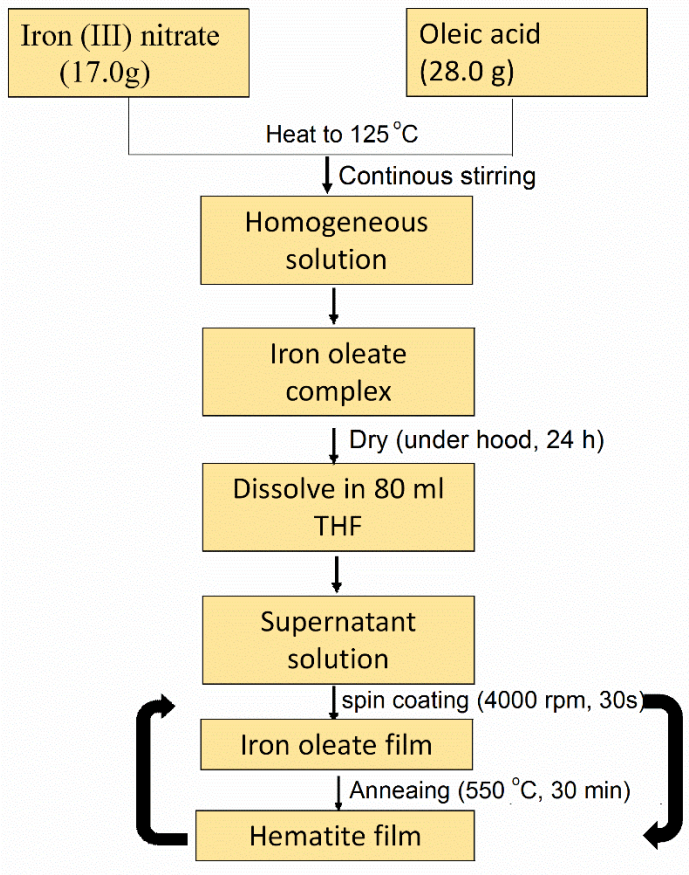

Figure 5-8: Schematic representation of the preparation procedure for spin coated hematite films.

Characterization.

Crystallinity and phase purity of the nanostructures were examined with XRD using Cu-Kα radiation (λ=1.5401 Å). The surface morphology of the films was studied using a high resolution scanning electronic microscope operating at 2 kV and high-resolution confocal Raman microscopy (confocal Raman imaging, AFM and SNOM, WITec alpha300R) equipped with an argon laser (excitation at 532 nm). Optical absorption properties of the films were characterized using a UV−vis−NIR spectrophotometer (Perkin Elmer, Lambda 750). Photoelectrochemical properties of the films were investigated using the PEC system in Figure 4-2. A Bio-Logic VMP300 potentiostat (Knoxville TN 37930, USA) controlled by the EC-Lab® V10.40 software was used

to carry out electrochemical impedance measurements. Photoluminescence (PL) spectroscopy was carried out at room temperature using a Perkin-Elmer LS-55 Fluorescence Spectrometer.

5. 2B.2 Results and discussion

The surface morphology and film thickness of the pristine hematite film obtained by FESEM characterization were as shown in Figure 5-9. Spin coating ensures a uniform and conformal coverage across the substrate. The film consists of densely packed small-sized spherical nanostructures in a non-porous layer of an average thickness of 415 nm. The average diameter of the nanoparticles was 25-30 nm. The SEM images of the Ti-doped hematite films were as shown in Figure 5-10. It is clear that particle size decreased with increasing doping concentration level. Ti dopants can act as structural directing agents to produce ideal structural architectures which can increase charge collection efficiency [3]. Small grains offer increased surface area and shorter diffusion distances for photogenerated holes and thus facilitate charge transport in hematite. On the other hand, small grains are commonly associated with higher density of grain boundaries which lead to higher electron-hole recombination [4].

Figure 5-11 shows 2D and 3D AFM top view images of the films obtained at room temperature. The figure confirms a uniform surface coverage on the substrate. No significant differences were observed between the morphology of the undoped film and the doped ones. Ti doping did not affect the morphology of the thin films during growth. Consistent with FESEM imaging, the AFM revealed that nanoparticles, well distributed on the substrate and intensely dense, were grown on the FTO substrate.

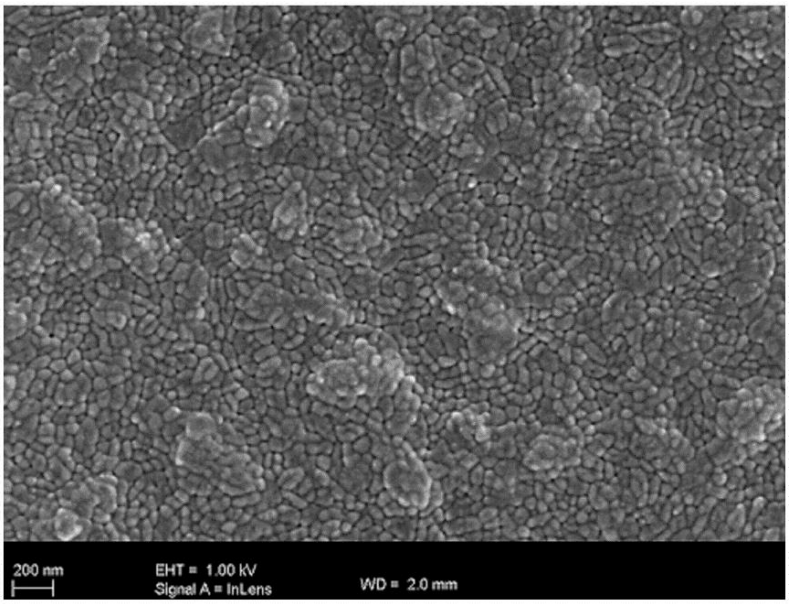

(A)

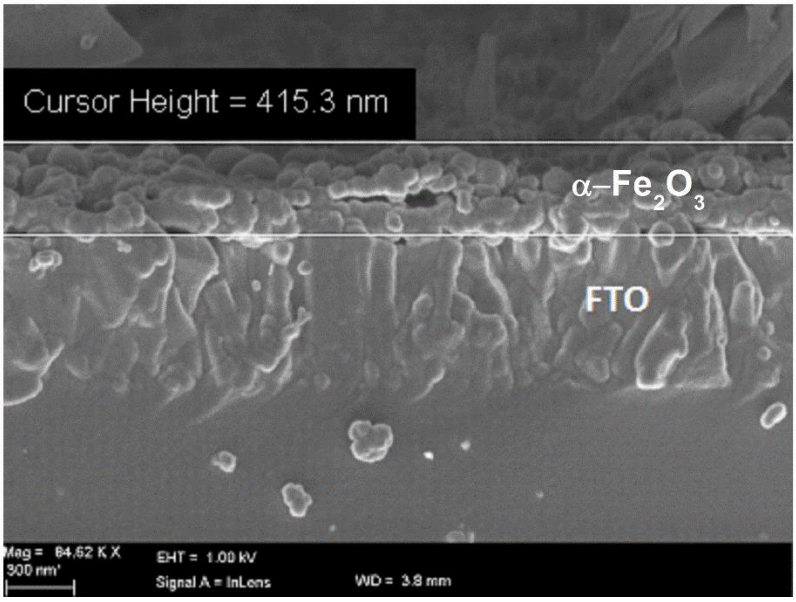

(B)

Figure 5-9: FESEM top-view (A) and cross-sectional view (B) micrographs of spin-coated pristine hematite photoanode.

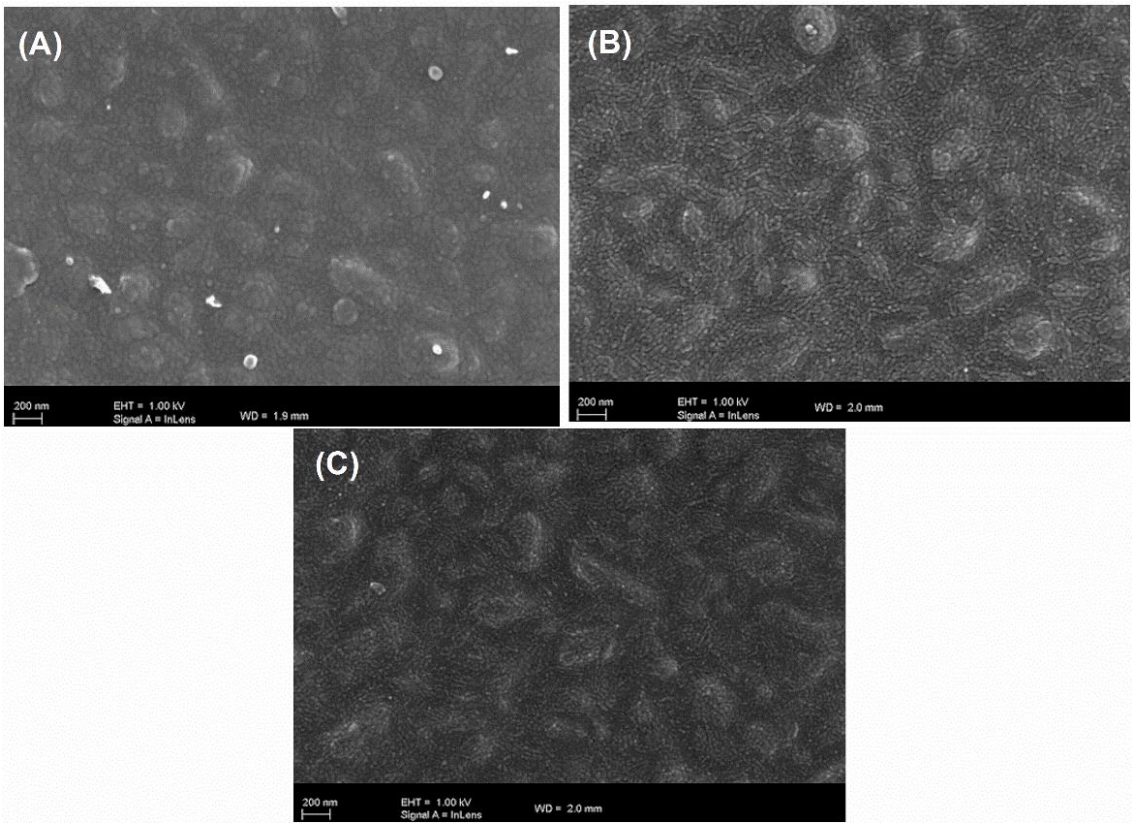

Figure 5-10**:** FESEM micrographs of the spin-coated Ti-hematite photoanodes: (A) 0.5, (B) 1.0 and (C) 2.0 at% Ti. The scale bar is equal to 200 nm.

XPS was performed to confirm the incorporation of Ti into hematite in the Ti-doped photoanodes. The full XPS spectra (survey) in Figure 5-12 (A) indicated the presence of the main elements (Fe, O, and Ti) in the fabricated films. The high-resolution spectra of the Fe 2p peaks in Figure 5-12 (B) shows distinct typically observed peaks with binding energies centered at ~ 711.58 eV and ~ 724.91 eV which respectively correspond to Fe $2p_{3/2}$ and Fe $2p_{1/2}$,of α-Fe_2O_3 [5]. For the Ti 2p spectra, Figure 5-12 (C) revealed two peaks positioned at binding energies of ~ 459.2 eV and ~ 464.8 eV assigned to Ti $2p_{3/2}$ and Ti $2p_{1/2}$ respectively, which suggest existence of to the Ti^{4+} state in the Ti-O-Fe structure [6]. The existence of Ti in +4 state is also confirmed by the splitting (~ 6 eV) between the two peaks (Ti $2p_{3/2}$ and Ti $2p_{1/2}$) [7]. No Ti peaks detected in the pristine film as expected.

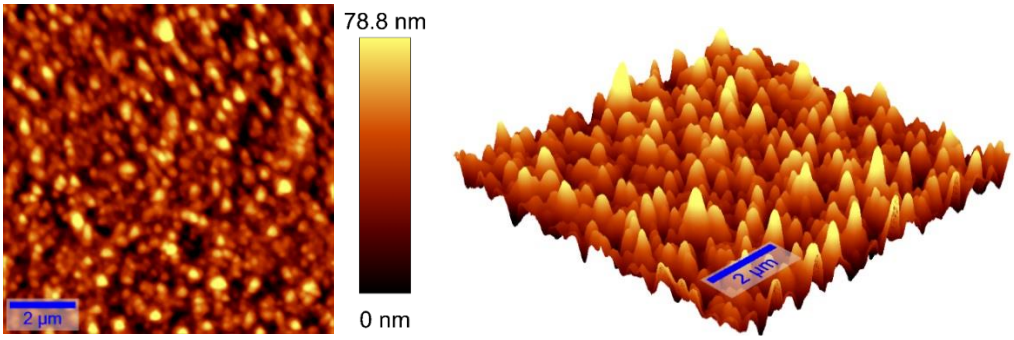

(A): Pristine

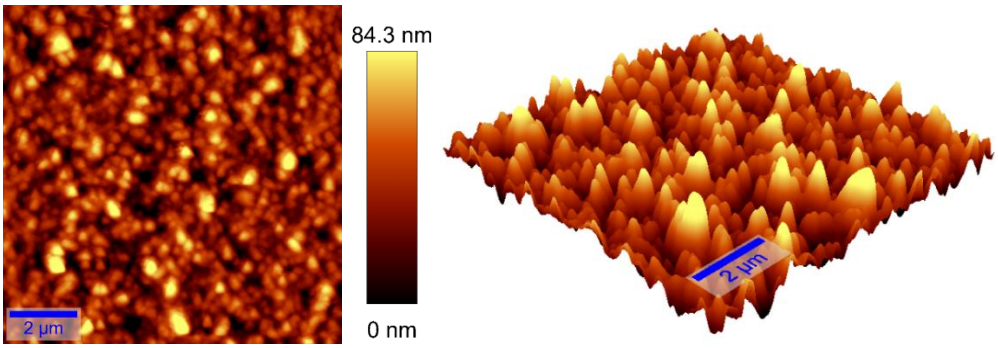

(B): 0.5 at% Ti

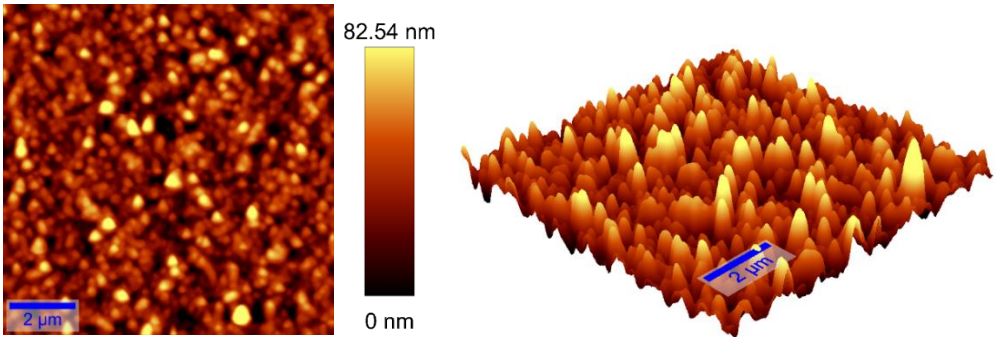

(C): 1.0 at% Ti

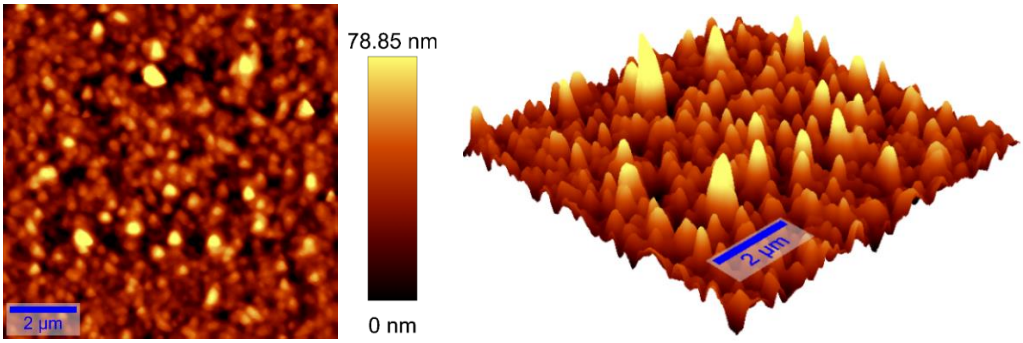

(D): 2.0 at% Ti

Figure 5-11: AFM 2D and 3D top view images of the pristine and Ti-α-Fe_2O_3 films.

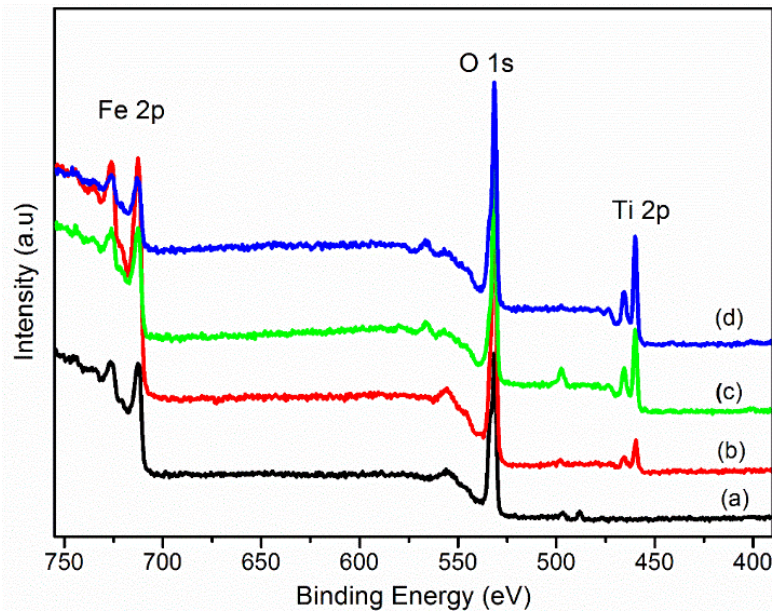

(A)

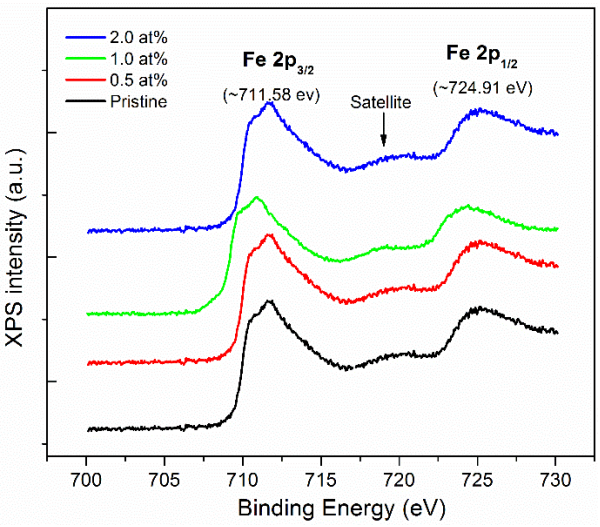

(B)

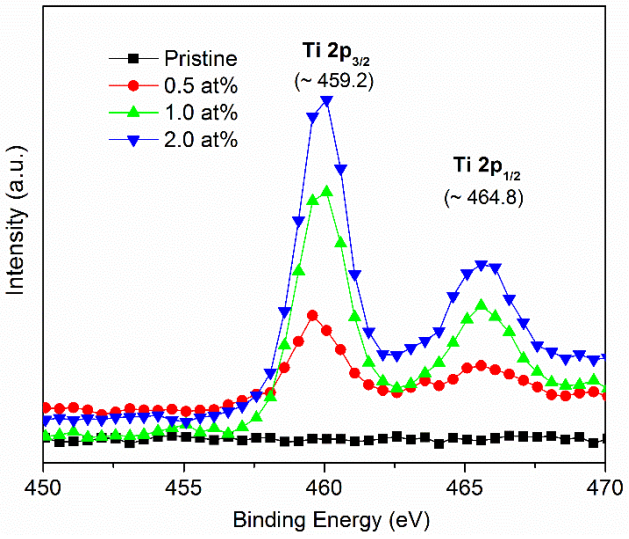

(C)

Figure 5-12: XPS spectra for pure and Ti-doped hematite (A) survey scan (a: pristine, b: 0.5, c: 1.0 and d: 2.0 at% Ti). (B) High-resolution spectra of the Fe 2p and (C) High-resolution spectra of the Ti 2p signal.

The XRD patterns of the pristine and Ti-hematite nanostructures obtained at room temperature are presented in Figure 5-13. The figure reveals less prominent and broad diffraction peaks for the films relative to those of the substrate. However, the Bragg reflections observed at $2\theta = 33.8°$,

35.8° and 43.6° were indexed to (104), (110) and (113) crystal planes in hematite [JCPDS-73-0603]. The relatively weak and broad diffractogram peaks from the hematite film could be attributed to small nanocrystallites as evidenced by FESEM. The same trend of weak XRD signal for spin coated hematite was previously reported by Souza *et al*. [1]. In spite of low intensity, a careful inspection of the peaks in the expanded (Figure 5-13 (B)) revealed a stronger relative intensity for the (110) peak compared to that of (104) peak, with the ratio of intensities; I(110)/I(104) found as ~ 1.15, obtained by fitting the measured peaks with a Lorentzian shape. This implies that the nanoparticles grew in the [110] crystallographic plane as previously reported [1]. No peaks were observed for Ti impurities. The strong peaks identified by solid dots originated from the FTO substrate.

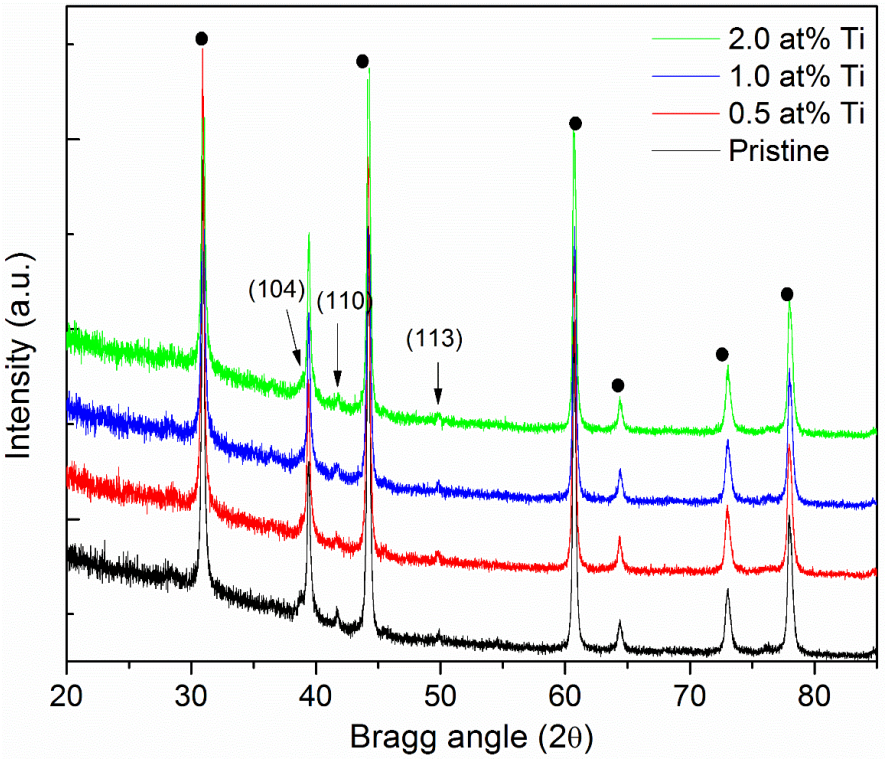

(A)

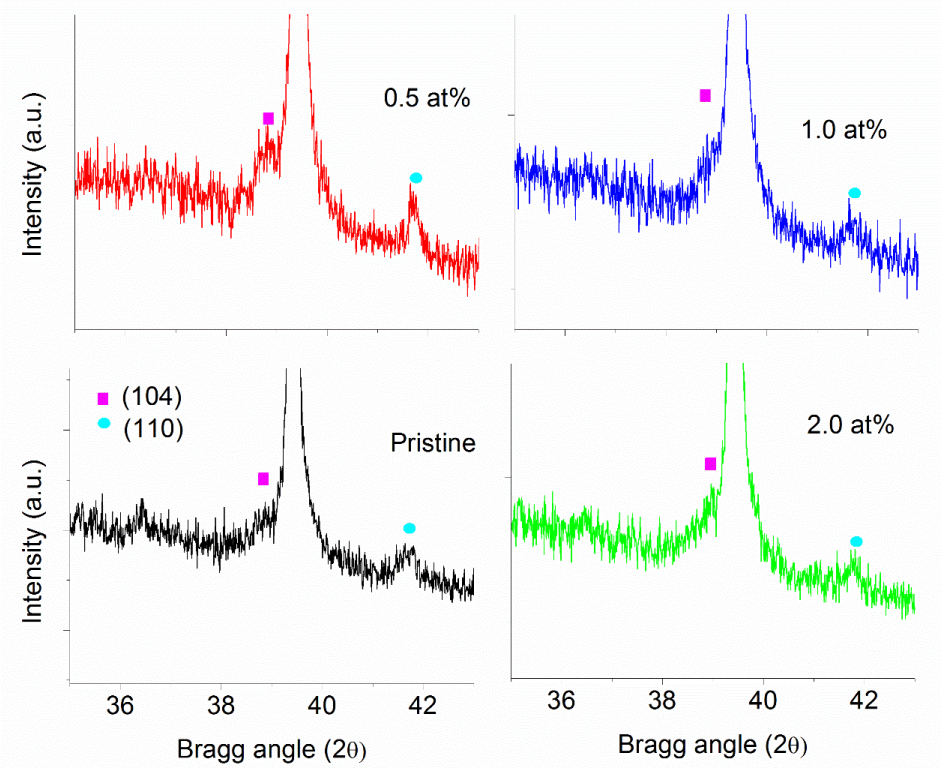

(B)

Figure 5-13: XRD patterns of the pristine and Ti-hematite thin films (A) and the expanded view of the (110) and (104) peaks (B) .

The phase purity of the samples was further verified by Raman spectroscopy. Figure 5-14 (A) shows typical Raman phonon modes of hematite between 200 and 620 cm^{-1}, with a small contribution from the substrate between 1050 and 1150 cm^{-1} [8]. The phonon modes appear narrow and strong signifying high crystallinity of the nanostructures, which confirms that the small XRD peaks were a consequence of small crystallites in the films and not poor crystallinity. Since upon doping Ti dopants enter the lattice of hematite substitutionally, Ti doping is expected to lead to slight compression of the crystal, owing to the small ionic size of the Ti dopant, Ti^{4+} (0.605 Å) as compared to that of Fe^{3+} (0.645 Å), inducing blue shift in Raman phonon frequencies [9]. However, in this study, no significant difference was observed in Raman frequencies between the pure and doped films (Figure 5-14 (B)).

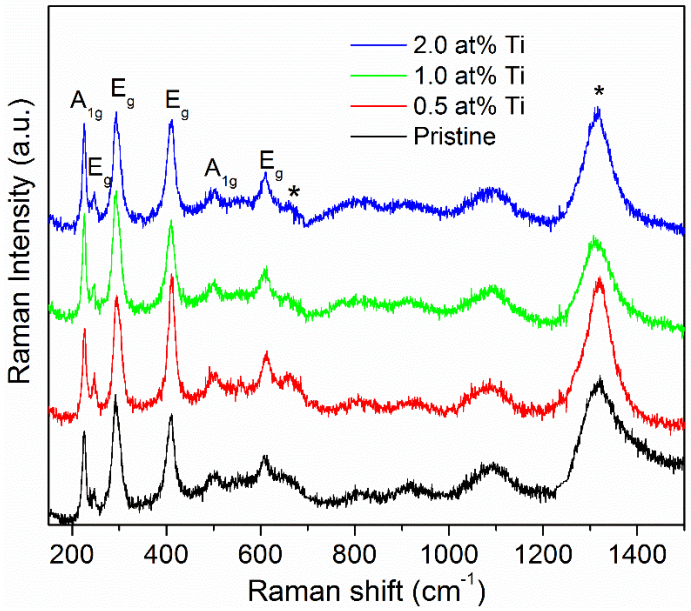

(A)

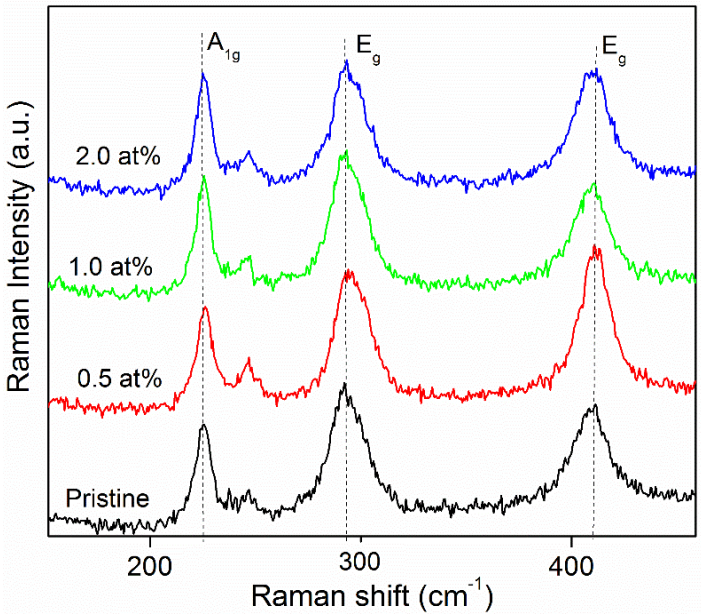

(B)

Figure 5-14: Raman spectra of pristine and Ti-hematite thin films (B) Extended view of the spetra reaviling no significant changes in Raman frequencies in the films due to Ti-doping.

Two extra modes were observed at frequencies of ~ 660 cm^{-1} and ~ 1316 cm^{-1}, marked with (*) in Figure 5-14 (A). According to group theory analysis of the first order Raman selection rules, the

two peaks arise from forbidden scatterings in Raman phonon scattering. Shim and Duffy studied the pressure dependence of Raman phonon modes in hematite and assigned the vibrational mode at ~ 660 cm^{-1} to E_u symmetry which is IR-active [10]. In crystals with inversion symmetry (centrosymmetric) like hematite, the *mutual exclusion rule* forbids Raman active phonon modes to be IR active and *vice versa*. Therefore, the E_u phonon mode is prohibited in Raman scattering. Forbidden modes may be activated (allowed) in Raman scattering as a result of disorder which relaxes or lifts selection rules [11]. The phonon mode at ~ 1320 cm^{-1} was attributed to a second-order phonon process overtone $2E_u$ (2 x 660)of the mode at 660 cm^{-1} [10]. We note that to date the origin of this high-frequency phonon mode is still surrounded by controversial discussions and will not be discussed further in this work.

Figure 5-15 shows UV-vis absorption and transmittance spectra of the synthesized pristine and Ti-doped hematite films. Inset of Figure 5-15 (A) shows photographs of the films. By visual inspection, the films appeared smooth, glossy and semitransparent, resulting in transmittance characteristics shown in Figure 5-15 (B). All the films exhibited relatively high transmittance of up to 50 % at high wavelength region. Conversely, the absorption is low in the visible area. No distinction in the absorption spectra of pristine and doped films with a nearly overlapped intrinsic absorption edge observed at ~ 597 nm, suggesting no significant change in the bandgap of hematite due to Ti incorporation. The indirect energy bandgap was estimated by Tauc model and presented in Figure 5-16. No significant difference in bandgap between undoped and doped films, even among the doped samples were observed. The films showed the bandgap of around 2.09 eV. This suggests that incorporation of Ti into hematite lattice did not cause significant changes to electronic band structure of the pristine hematite.

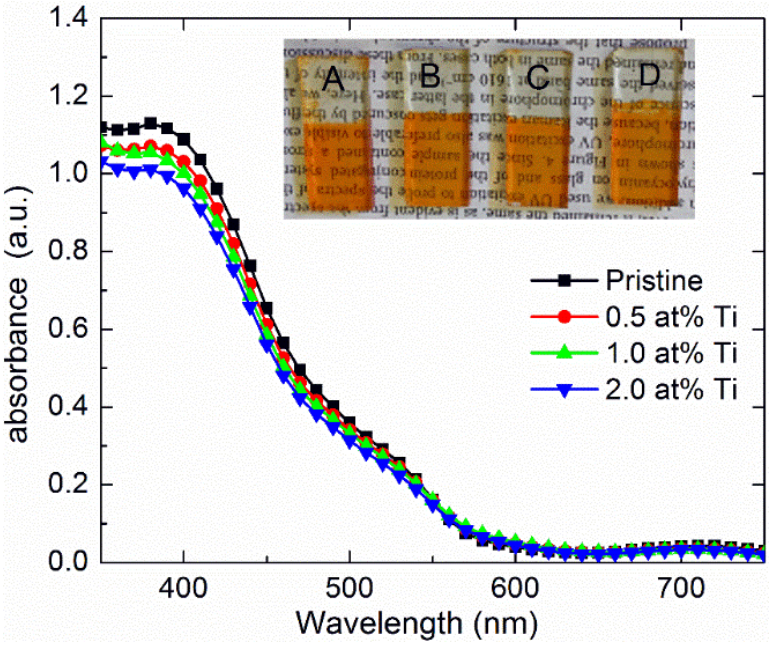

(A)

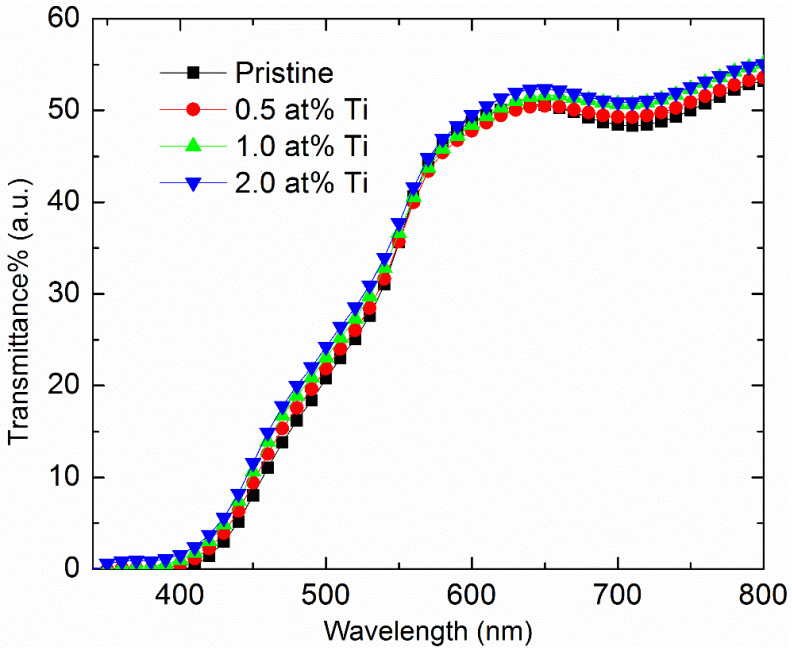

(B)

Figure 5-15: UV–vis absorption spectra (A) and transmittance spectra (B) of pristine and Ti-hematite photoanodes. Inset of (A) shows the photographs of the films (A: pristine, B:0.5, C:1.0 and D:2.0 at% Ti).

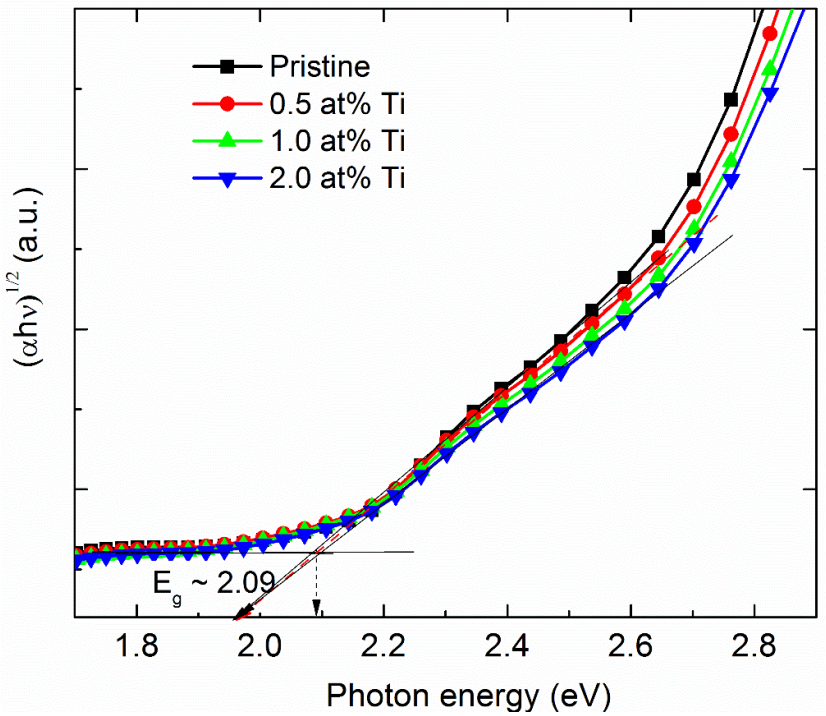

Figure 5-16: Band gap analysis using Tauc plots for pristine Ti-doped α-Fe_2O_3 photoanodes.

To evaluate the photoelectrochemical performance of the photoanodes, PEC measurements were carried out by linear sweep voltammetry at 10 mVs^{-1} in 1M KOH, in darkness and under simulated illumination using the same PEC system in Figure 4-2. Figure 5-17 shows the measured water oxidation photocurrent density as a function of the applied potential for pristine and Ti-hematite photoelectrodes. The pristine film showed a negligible current density of ~ 0.013 mA/cm^2 at 1.23 V *vs* RHE, despite the favorable [110] growth direction for charge transport in hematite. Hematite is experimentally reported to be an anisotropic conductor, with conductivity observed greater along the (001) basal planes than planes parallel to the *c*-axis [12, 13]. The anisotropic behaviour has been ascribed to lower effective electron mass and hence higher mobilities across the basal planes than in other phases perpendicular to the plane [12, 13]. The low photocurrent density in the pristine film was attributed partly due to poor absorption of light as the films displayed high

transparency in the visible region (Figure 5-15(B)). By varying the number of layers deposited onto the substrate from 1 to 7 layers, different pristine films with different thicknesses were produced under the same preparation conditions, which did not show any effect on the current density production. Souza *et al*. reported a similar behaviour of poor photoelectrochemical activity in pristine hematite prepared by same technique [1]. The poor PEC response was ascribed to poor conductivity and high recombination of the photoexcited electron-hole pairs in the pristine film. Reportedly, pure hematite exhibit poor intrinsic electrical conductivity (< 1 cm^2 V^{-1} s^{-1}) [14]. The low intrinsic conductivity is attributed to strong localization of the 3d electrons at the Fe ions [15]. The crystal field due to O^{2-} surrounding the Fe atom plus their Coulomb correlation which prevents the electrons from forming 3d-bands, limit their transport through the crystal lattice resulting in very low conductivity [15].

Ti incorporation significantly improved the PEC performance of the pristine hematite photoelectrode as presented in Figure 5-17. The inset figure clearly shows a sharp increase of current density upon Ti doping. The current density significantly increased to a remarkable value of ~ 1.2 mA/cm^2 at 1.23 V *vs* RHE, with 0.5 at% doping level. This value was also found to be 3.5 times larger than the value reported by Souza *et al*. [1] of 0.35 mA/cm^2, for the 0.5 % Si-α-Fe_2O_3 system. In addition, the plateau current density increased significantly to ~ 1.85 mA cm^{-2} at 1.45 V *vs* RHE as compared to the almost negligible value for the pristine film with 0.5 at% doping level. Assuming that the films were of approximately the same thickness, it can be concluded that the results were indicative of the successful suppression of recombination of photogenerated electron-hole pairs which limits with charge collection efficiency at the semiconductor-electrolyte interface.

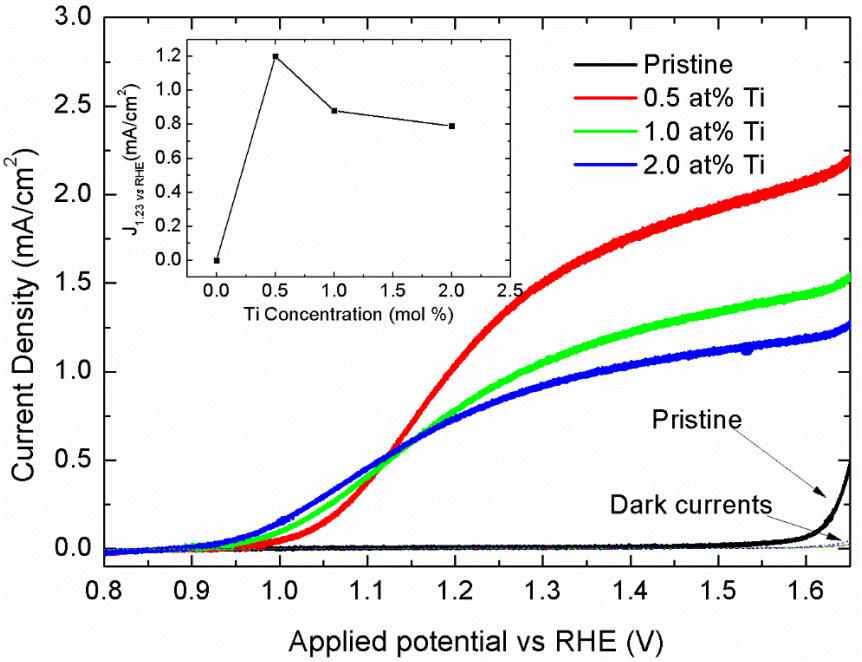

Figure 5-17: Current-potential curves for spin coated pristine α-Fe_2O_3 and α-Fe_2O_3:Ti. The inset shows a plot of current density at 1.23 V vs RHE as a function of doping level.

The results indicated improved photogenerated holes collection efficiency in the modified films. However, as previously reported in literature, including the dip coated Ti-hematite in this study, increasing the Ti concentration above a certain optimum level (depending on the material properties) becomes less effective [16, 17]. Increasing doping level to 1 at% and 2 at% resulted in a decrease in current density, respectively yielding ~ 0.88 and ~ 0.79 mA/cm^2 at 1.23 V *vs* RHE. In spite of the decrease in current density with increasing doping level, lower photocurrent onset potentials were achieved for all doping levels compared to pristine film (Figure. 5-18). The onset potential was also found to depend on the doping concentration level. A significant shift in the onset potential by > 400 mV was achieved with 0.5 at% doping level. A low photocurrent onset is very crucial towards reduction of the overpotentials required to achieve the maximum photocurrent density and thus increase the overall efficiency [18].

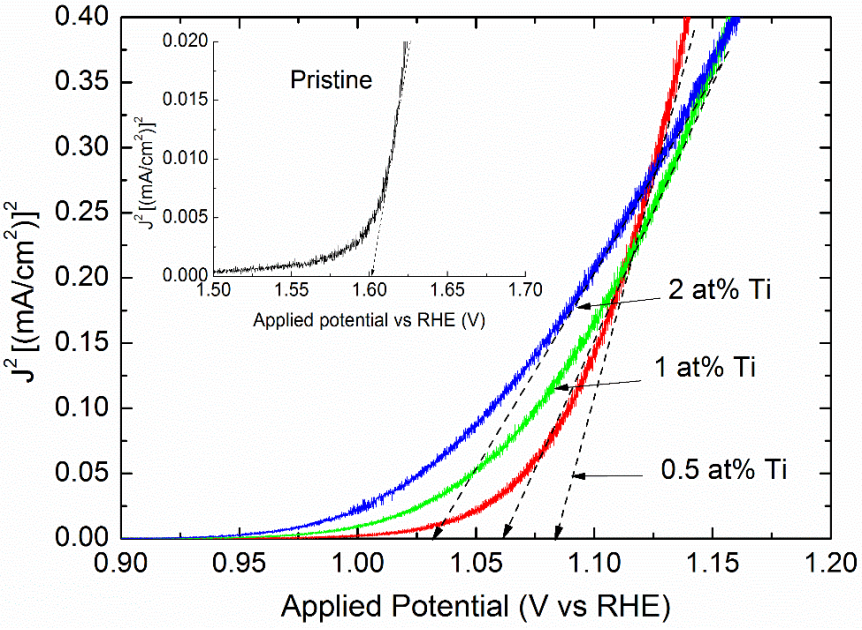

(A)

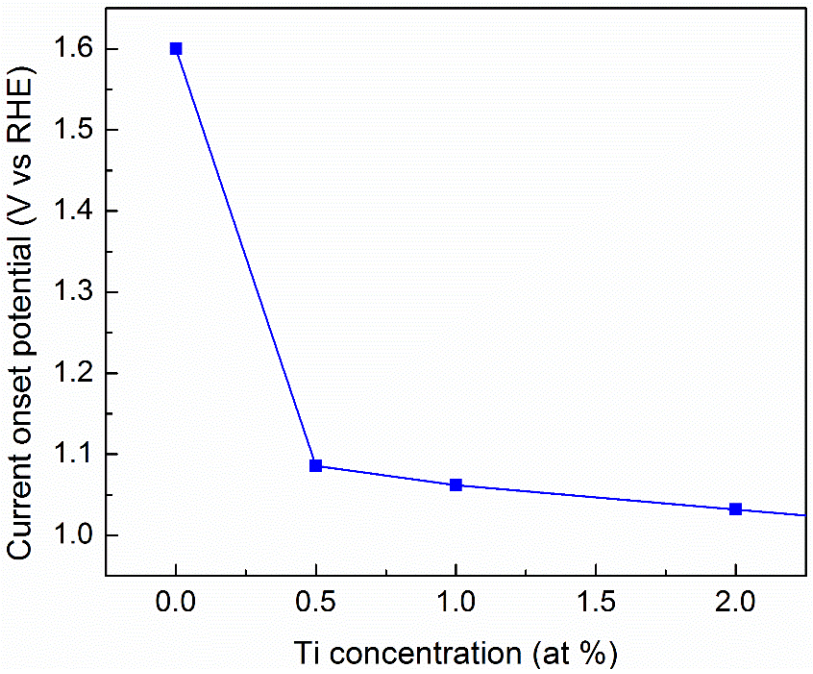

(B)

Figure 5-18: (A) The estimated water oxidation photocurrent onset potentials for Ti-doped and pure hematite (inset) photoanodes. (B) A plot of onset potentials as a function of doping level, clearly showing photocurrent onset potential with increasing doping level.

Even though it is difficult to compare PEC performance from samples synthesized with different methods due to the existence of other accentuating or compensating defects [19], it is noticed that spin-coated Ti-doped hematite photoanodes exhibited better PEC performance compared to their dip coated counterparts. The difference in the performance of the photoanodes was attributed to the quality of the thin films which was influenced by the nature of the preparation procedure. Compared to dip coating, spin coating allows uniform coverage on the substrate with minimal density of surface imperfections (like cracks) that generally provide recombination site for photogenerated electrons and hole pairs. As a result, special attention was given to the spin-coated doped samples, and further experiments were conducted to understand the enhancement in PEC performance of Ti-doped films.

To understand the enhancement in the performance of the 0.5 at% Ti-doped hematite photoanode in water splitting, charge transport and transfer properties in the fabricated films were investigated by electrochemical impedance (EIS) and photoluminescence (PL) spectroscopy. EIS is commonly used to characterize charge transfer properties at the electrode-electrolyte interface. The radius of the arc in the EIS Nyquist plots reflects the interfacial charge transfer resistance [5]. A larger semicircular radius represents larger electron transport resistance and lower charge separation efficiency of the photoexcited electron-hole pairs [20]. The impedance measurements were carried out in 1 M KOH at 1.23 V vs RHE, under dark conditions, in the frequency range of 100 kHz – 0.01 Hz. In general, the films exhibited relatively high impedance values as shown in Figure 5-19 (A). As a result, the use of equivalent circuit the experimental data was not easy, and the results were analyzed only from the semicircular radius of the Nyquist plots. All the Nyquist plots exhibit a depressed semicircle. Ti-doped photoanodes show smaller circular radii compared to the pristine

photoanode, suggesting reduced charge transfer resistance and improved charge separation in those films.

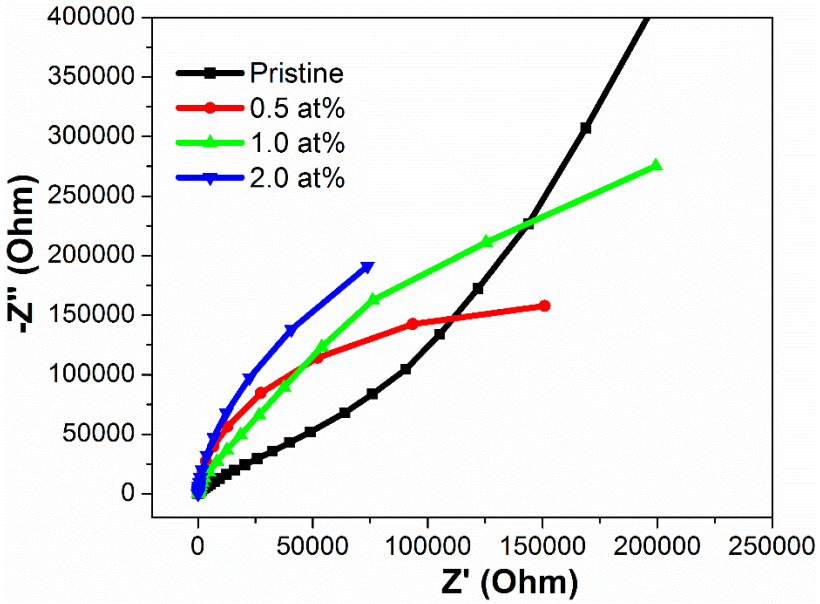

(A)

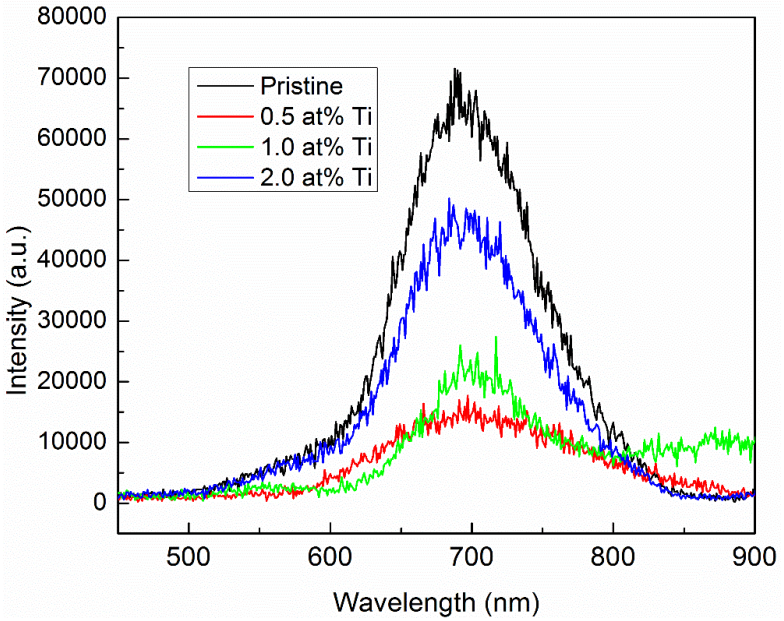

(B)

Figure 5-19: (A) Electrochemical impedance spectra (Nyquist plots) of the pristine and Ti-hematite photoanodes at 1.23 V vs RHE in the darkness. (B) Photoluminescence (PL) spectra of the pristine α-Fe_2O_3 and α-Fe_2O_3: Ti nanoparticles.

Ti dopant played an important role in promoting charge separation and transportation [5]. Consistent with current density data, the 0.5 at% doped film exhibited the smallest arc radius and hence the lowest resistance compared to other doped films.

Photoluminescence spectroscopy is a useful tool commonly used to understand the charge transfer, trapping and recombination process of the charge carriers in semiconductor materials [21]. The intensity of the PL spectrum is directly related to recombination rate of the photogenerated electron-hole pairs, with a strong PL intensity implying rapid charge recombination in the material [2, 21]. Room temperature PL analysis was also conducted to understand the state of photogenerated electron-hole pairs in the fabricated photoanodes. Figure 5-19(B)) shows the PL properties of all the fabricated films. The pristine film exhibited the highest PL intensity, suggesting high recombination losses in the pristine film, hence causing relatively poor PEC performance of the film. Incorporation of Ti induced a positive impact on the film as demonstrated by reduced PL intensity compared to the pristine one. Among the doped films, the 0.5 at% film showed the lowest intensity followed by the 1.0 at% Ti-doped one, suggesting effective charge separation and lower recombination losses in the respective thin films. Conversely, an increase in the peak intensity was observed in the 2.0 at% sample which suggested enhanced recombination of carriers as the density of excess electrons increase in hematite lattice. Accordingly, photocurrent density decreased. The PL data was found to be consistent with PEC and EIS results.

5.2B.3 Optimization of doping concentration

Because of the promising PEC performance of the spin-coated Ti-doped hematite nanostructured films, the modified films were further studied at varying concentration levels. Considering the 0.5 at% as the reference doping level, further experiments were performed at 0.1, 0.25 0.3, 0.4, 5, 10, 15 and 20 at% Ti concentrations, with samples prepared using the same synthetic procedure and

growth conditions. Photocurrent-voltage characteristic curves of the generated photocurrent density were obtained as shown in Figure 5-20 (A). A summary of the PEC characteristics of all the films at various doping level is presented in Table 5-1. It is quite clear from the figure and Table 5-1 that the photoanodes doped with 10 and 15 at% concentrations performed even better than the 0.5 at% film at 1.23 V *vs* RHE. The photocurrent remarkably increased up to ~ 1.39 mA/cm^2 at 1.23 V *vs* RHE for 10 at% and ~ 1.84 mA/cm^2 for 15 at% Ti doping concentration. A photocurrent increase of 50% was achieved (at 1.23 V *vs* RHE) with 15 at% doping level compared to 0.5 at% Ti. The comparison of the photoelectrochemical properties of spin coated samples fabricated in this study with literature in terms of photocurrent density at 1.23 V *vs* RHE was given in Table 1-1. Based on Table 1-1, in Section 1.1, the obtained results demonstrate superior photoelectrochemical performance as compared to a number of different techniques in the literature (see Table 1-1).

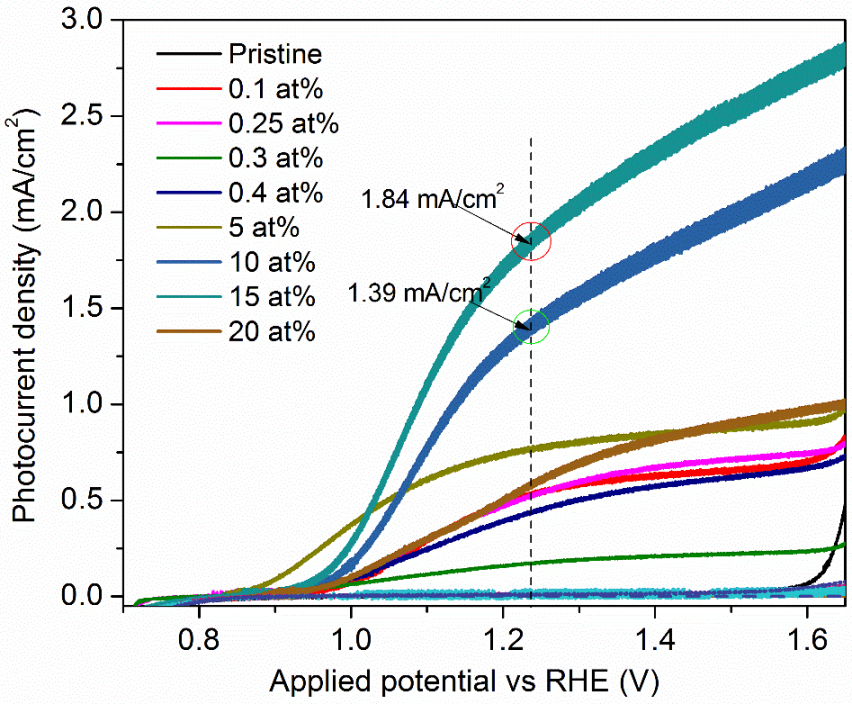

(A)

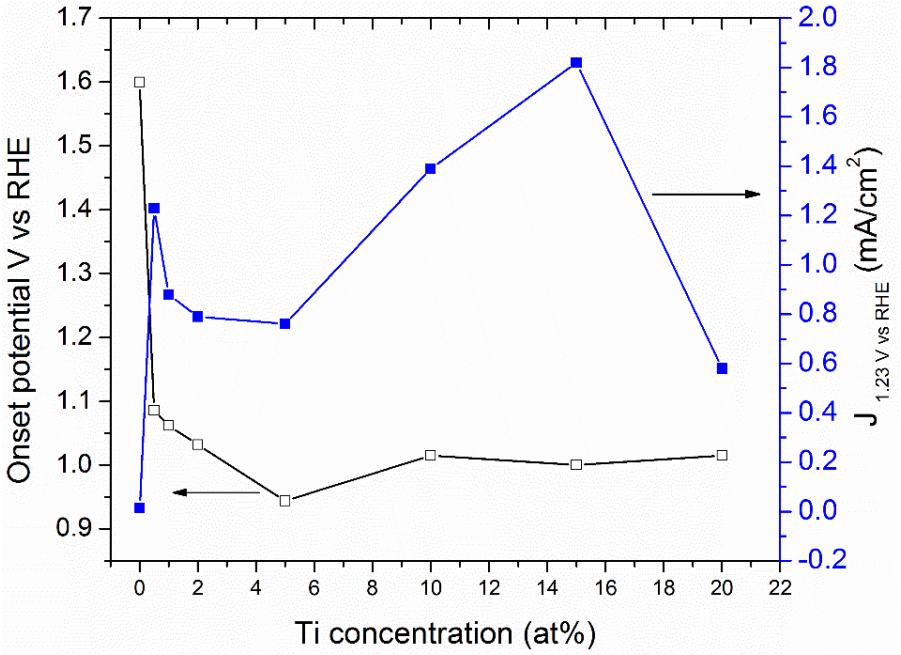

(B)

Figure 5-20: (A) Photocurrent-potential response of pristine and modified films at various Ti concentration levels and, (B) variation of onset potential and current density with Ti concentration level.

Table 5-1: Photoelectrochemical properties of pristine and Ti-hematite at different Ti concentrations.

Sample Ref. #	Ti concentration (at%)	Photocurrent density (mA/cm^2) at		Onset potential vs RHE (V)
		1.23 vs RHE (V)	1.45 vs RHE (V)	
1	0	0.01	0.01	1.600
2	0.1	0.54	0.64	1.039
3	0.25	0.54	0.72	1.035
4	0.3	0.16	0.21	1.023
5	0.4	0.44	0.61	1.019
6	0.5	1.23	1.85	1.020
7	1.0	0.89	1.29	1.026
8	2.0	0.79	1.08	1.032
9	5.0	0.74	0.85	0.945
10	10	1.39	1.87	1.015
11	15	1.84	2.44	0.995
12	20	0.58	0.85	1.015

Although the 5 at% doped film exhibited a quick onset of photocurrent (~ 0.95 V vs RHE) compared to the 10 and 15 at%, the film produced a lower current density compared to the 0.5 at% electrode. The low photocurrent in the 5 at% doped film could be ascribed to accumulation of holes at the surface of the photoanode due to sluggish oxygen evolution reaction kinetics at the surface of hematite [22, 23]. The drawback of slow kinetics has been most improved by surface modifications which catalyse hole transfer and reduce surface charge recombination, and enhancement in PEC activity has been observed [24-26]. At higher applied potentials, the 10 at% and 15 at% samples exhibited intense photocurrent density with increase of applied potential. The 15 at% film showed plateau photocurrent of ~ 2.44 mA/cm^2 at 1.45 V vs RHE (32% increase compared to the 0.5 at% film). At higher anodic potentials, electrons are swept out rapidly by the space charge layer electric field and collected by the external circuit, thereby freeing an increasing number of photogenerated holes which accumulate at the electrode surface and drive the water oxidation reaction. On the other hand, at 20 at% doping level the photocurrent decreased to ~ 0.58 mA/cm^2 at 1.23 V *vs* RHE, which is also lower compared to values obtained with 1, 2 and 5 at% doping concentrations probably due to over doping. The decrease in photocurrent at higher Ti concentration might be attributed to a decay in crystallinity of the hematite nanoparticles as a consequence of disorder and shrinkage of the crystal grains that might have impact on carrier lifetime [16].

The variation of the current density (J) at 1.23 V *vs* RHE and onset potential as a function of doping level is clearly illustrated in Figure 5-20 (B). It is quite clear that the current onset potential decreased further with an increase of doping level. However, a slight increase in the onset potential was noticed at 10 at% (compared to 5 at%), which could be ascribed to enhanced accumulation of

holes at hematite surface as the Ti concentration increases. It was noticed also that the potential dropped again at 15 at% before increasing at 20 at%. To understand the enhancement in photocurrent with Ti doping level, further experiments were performed to examine the phase composition and charge transfer properties of the films.

Figure 5-21 shows XRD patterns of the films. The results revealed new peaks at $2\theta = 21.2°$ and 38.5° (Co-kα) for the 15 and 20 at% films. These peaks have been identified as the (200) and (230) planes for pseudobrookite, Fe_2TiO_5 phase formation, which is a hybrid of α-Fe_2O_3 and TiO_2 [27, 28]. Formation of this titanate phase in Ti-hematite systems has been previously reported in the literature [29]. When doping hematite with Ti, annealing temperature higher than 500 °C might introduce Fe_2TiO_5 structure when TiO_2 is reacted with hematite, forming a heterojunction structure with hematite at the surface. The coupling of hematite with such materials facilitates charge separation and accelerates delivery of photogenerated holes at the interface, hence improved PEC performance [23, 27, 29-31].

At 20 at% concentration, the formation of a TiO_2 layer could not be ruled out as suggested by the increasing intensity of the peak at $2\theta = 38.5°$, which matches (203) plane in TiO_2 [29]. According to Deng *et al.,* at higher concentrations, excess TiO_2 may not react with Fe_2O_3 to introduce Fe_2TiO_5, and result in a thin layer of TiO_2 on the surface [29]. Formation of the TiO_2 on the surface would lead to decrease in visible light absorption due to a large bandgap (3 eV) and subsequently have negative effect on the PEC performance [29]. This information explains the changes in photocurrent and the onset potential as a result of the existence of Fe_2TiO_5 and TiO_2 on the surface at concentrations beyond 5 at%.

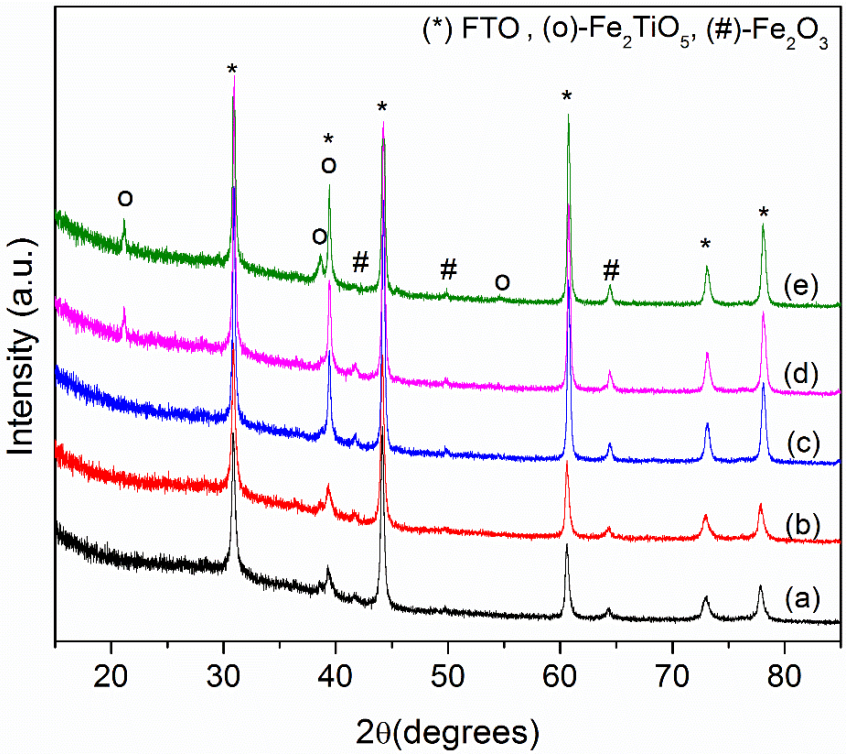

Figure 5-21: XRD patterns of the pristine (a) and Ti-hematite nanostructured films at (b): 5, (c): 10, (d): 15 and (e):20 at%.

The visible absorption properties of the films were also examined and their absorption spectra obtained as presented in Figure 5-22. In comparison with other films, the 15 at% Ti-doped sample showed improved optical absorption throughout the visible spectrum range. Interestingly, the 20 at% doped photoanode showed the lowest absorption properties compared to other samples, which strongly supports the assumption that a thin layer of TiO_2 might have formed at the surface at that particular concentration level. Inspite of the difference in the relative intensity of absorption, the absorption edge of all the films showed the same onset wavelength, suggesting no change in the bandgap with varied Ti concentrations. Figure 5-23 shows the Nyquist plots of the photoanodes measured in the darkness. The 15 at% sample exhibited a smaller semicircle arc compared to other photoanodes, evidencing the role of the presence of the Fe_2TiO_5 layer in improving charge transport resistance of hematite. On the other hand, consistent with current density data, the 20

at% samples showed the largest arc among the doped films signifying high charge transfer resistance in this film.

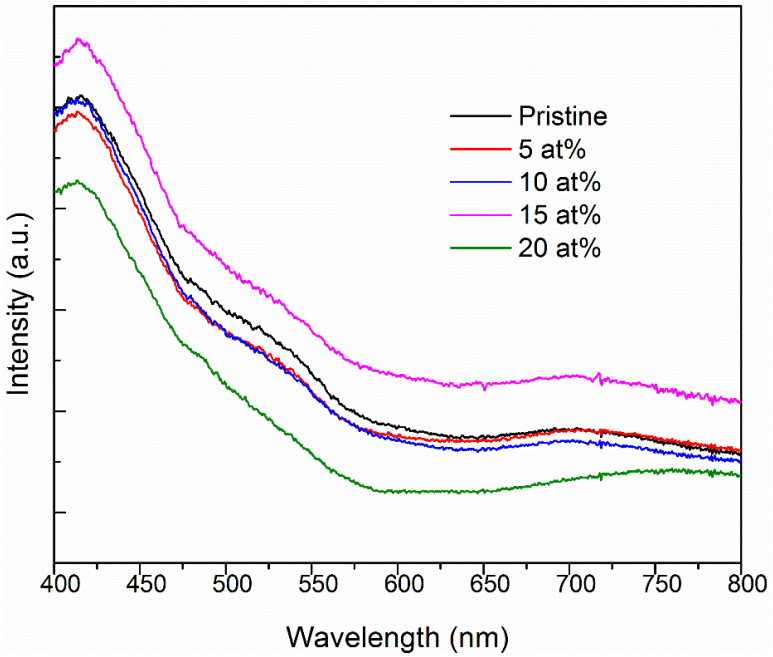

Figure 5-22: Optical absorption spectra of the pristine and highly Ti-doped films.

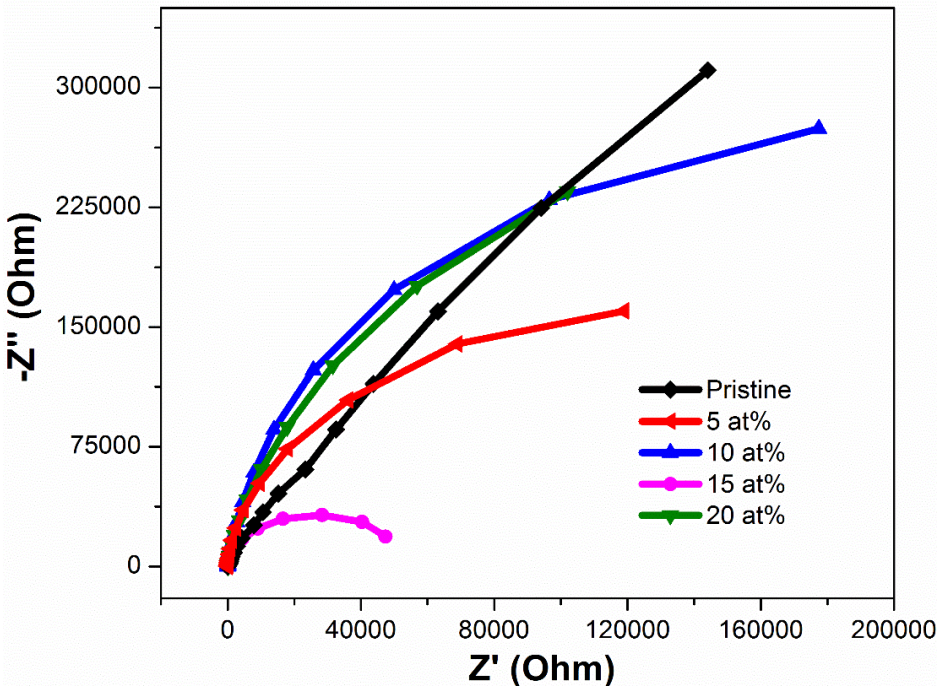

Figure 5-23: Nyquist plots of the pristine and highly doped Ti-hematite photoanodes.

Based upon the existing published data [29, 31], a schematic representation of band diagrams of the Fe_2TiO_5/α-Fe_2O_3 shown in Figure 5-24 was used to explain the enhancement in the high performance of the 15 at% doped film. Through Tauc plot analysis, the energy bandgap of Fe_2TiO_5 was measured to be around 2.0 - 2.1 eV [27, 29]. As can be seen from Figure 5-24, the top of the valence band of Fe_2TiO_5 is slightly higher than that of α-Fe_2O_3, which would favor effective transportation of photogenerated holes from α-Fe_2O_3 into Fe_2TiO_5, and reduce accumulation of photo holes on the surface of hematite and thus improve water oxidation (photocurrent density) [29, 31]. On the other hand, the bottom of the conduction band of Fe_2TiO_5 is more positive than that of α-Fe_2O_3 allowing injection of photogenerated electrons from Fe_2TiO_5 into α-Fe_2O_3 to the FTO substrate. The band alignment between the two materials would facilitate charge separation and reduce recombination of photogenerated electron-hole pairs [32]. Also, faster kinetics at the photoanode-electrolyte interface are enabled, due to a proper conduction band potential in Fe_2TiO_5, which facilitates a quick onset of photocurrent. A similar effect of the existence of Fe_2TiO_5 on PEC performance of hematite was reported by Deng *et al.* upon Ti doping by evaporating a $TiCl_4$ solution on iron precursor [29]. In addition to the aforementioned factors, the authors attributed the enhancement in photocurrent density to prolonged charge carrier lifetime due to improved charge properties of the interface between of the materials.

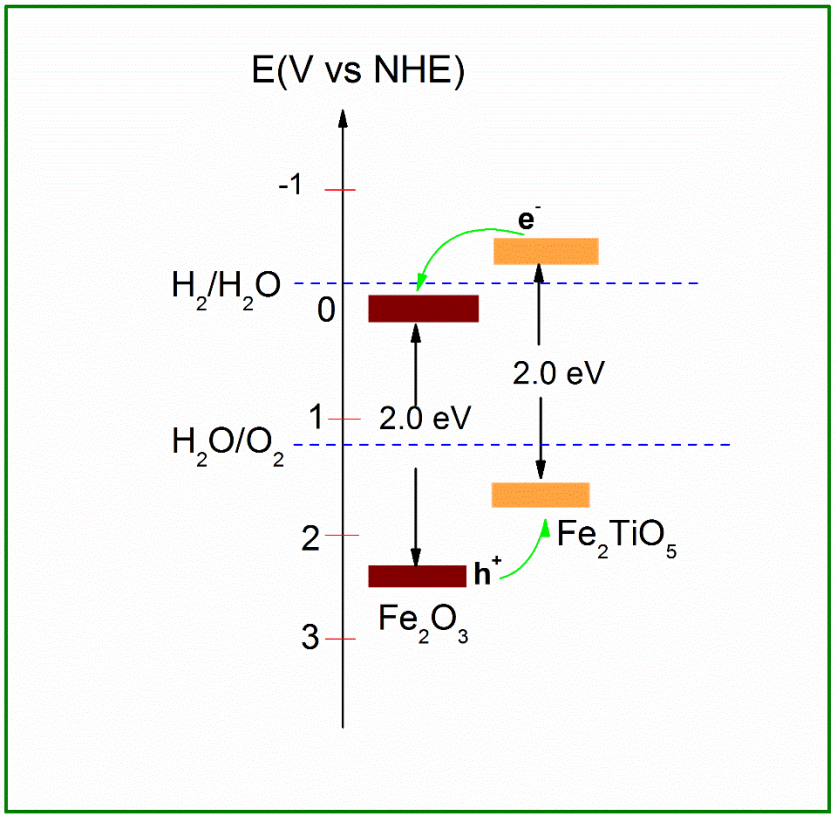

Figure 5-24: Schematic representation of the possible band level of Fe_2O_3 and Fe_2TiO_5 for water splitting (left). The green arrows represent electron (e^-) and hole (h^+) transport between the two materials. Adapted from ref. [31].

5.2B.4 Concluding remarks

Nanostructured Ti-doped hematite thin films were synthesized by spin coating for photoelectrochemical water splitting application. The results reported here present spin coating as a promising technique for Ti-doped hematite photoanodes. Photocurrent density of ~ 1.23 mA/cm^2 at 1.23 V *vs* RHE was achieved with 0.5 at% compared to pristine photoanode (~ 0.01 mA/cm^2). In addition, the photocurrent onset potential was shifted cathodically by > 400 mV. The enhancement in current density was attributed to the successful suppression of recombination of electron-hole pairs. Increasing doping concentration to 15 at% resulted in significant photocurrent

boost to 1.84 mA/cm^2 at 1.23 V *vs* RHE which is a 50 % increase compared to 0.5 at% film. XRD analysis revealed the formation of a Fe_2TiO_5 titanate phase at high doping level, which enhanced charge separation and minority carrier injection, owing to band alignment between the hematite and Fe_2TiO_5.

Reference

[1] F.L. Souza, K.P. Lopes, P.A.P. Nascente, E.R. Leite, Nanostructured hematite thin films produced by spin-coating deposition solution: Application in water splitting, Solar Energy Materials and Solar Cells, 93 (2009) 362-368.

[2] S. Shen, C.X. Kronawitter, J. Jiang, S.S. Mao, L. Guo, Surface tuning for promoted charge transfer in hematite nanorod arrays as water-splitting photoanodes, Nano Research, 5 (2012) 327-336.

[3] O. Zandi, B.M. Klahr, T.W. Hamann, Highly photoactive Ti-doped α-Fe2O3 thin film electrodes: resurrection of the dead layer, Energy & Environmental Science, 6 (2013) 634-642.

[4] S. Shinde, R. Bansode, C. Bhosale, K. Rajpure, Physical properties of hematite α-Fe2O3 thin films: application to photoelectrochemical solar cells, Journal of Semiconductors, 32 (2011) 013001.

[5] X. Xie, K. Li, W.-D. Zhang, Photoelectrochemical properties of Ti-doped hematite nanosheet arrays decorated with CdS nanoparticles, RSC Advances, 6 (2016) 74234-74240.

[6] J. Wang, B. Feng, J. Su, L. Guo, Enhanced Bulk and Interfacial Charge Transfer Dynamics for Efficient Photoelectrochemical Water Splitting: The Case of Hematite Nanorod Arrays, ACS applied materials & interfaces, 8 (2016) 23143-23150.

[7] H. Xia, W. Xiong, C.K. Lim, Q. Yao, Y. Wang, J. Xie, Hierarchical TiO2-B nanowire@α-Fe2O3 nanothorn core-branch arrays as superior electrodes for lithium-ion microbatteries, Nano Research, 7 (2014) 1797-1808.

[8] I. Cesar, K. Sivula, A. Kay, R. Zboril, M. Grätzel, Influence of feature size, film thickness, and silicon doping on the performance of nanostructured hematite photoanodes for solar water splitting, The Journal of Physical Chemistry C, 113 (2008) 772-782.

[9] E. Smith, G. Dent, Modern Raman spectroscopy-A practical approach, John Wiley & Sons Ltd, England, 2005.

[10] S.-H. Shim, T.S. Duffy, Raman spectroscopy of Fe2O3 to 62 GPa, American Mineralogist, 87 (2002) 318-326.

[11] M.S. Dresselhaus, G. Dresselhaus, A. Jorio, Group Theory-Application to the Physics of Condensed Matter, Springer2008.

[12] N. Iordanova, M. Dupuis, K.M. Rosso, Charge transport in metal oxides: a theoretical study of hematite α-Fe 2 O 3, The Journal of chemical physics, 122 (2005) 144305.

[13] X. Meng, G. Qin, W.A. Goddard III, S. Li, H. Pan, X. Wen, Y. Qin, L. Zuo, Theoretical understanding of enhanced photoelectrochemical catalytic activity of Sn-doped hematite: Anisotropic catalysis and effects of morin transition and Sn doping, The Journal of Physical Chemistry C, 117 (2013) 3779-3784.

[14] H. Pan, X. Meng, J. Cai, S. Lia, G. Qin, 4d transition-metal doped hematite for enhancing photoelectrochemical activity: theoretical prediction and experimental confirmation, RSC Adv., 5 (2015) 19353–19361.

[15] M.N. Huda, A. Walsh, Y. Yan, S.-H. Wei, M.M. Al-Jassim, Electronic, structural, and magnetic effects of 3d transition metals in hematite, J. Appl. Phys. , 107 (2010) 123712.

[16] Y.-G. Lin, Y.-K. Hsu, Y.-C. Lin, Y.-C. Chen, Electrodeposited Fe2TiO5 nanostructures for photoelectrochemical oxidation of water, Electrochimica Acta, 213 (2016) 898-903.

[17] K. Maabong, A.G.J. Machatine, B.S. Mwankemwa, A. Braun, D.K. Bora, R. Toth, M. Diale, Nanostructured hematite thin films for photoelectrochemical water splitting, Physica B: Condensed Matter, 535 (2018) 67-71.

[18] Gurudayal, S.Y. Chiam, M.H. Kumar, P.S. Bassi, H.L. Seng, J. Barber, L.H. Wong, Improving the Efficiency of Hematite Nanorods for Photoelectrochemical Water Splitting by Doping with Manganese, ACS Applied Materials & Interfaces, 6 (2014) 5852-5859.

[19] S. Chatman, C.I. Pearce, R.K. M., Charge Transport at Ti-Doped Hematite (001)-Aqueous Interfaces, Chemistry of Materials, 27 (2015) 1665−1673.

[20] Y. Liu, D.-P. Wang, Y.-X. Yu, W.-D. Zhang, Preparation and photoelectrochemical properties of functional carbon nanotubes and Ti co-doped Fe2O3 thin films, International Journal of Hydrogen Energy, 37 (2012) 9566-9575.

[21] Y.W. Phuan, E. Ibrahim, M.N. Chong, T. Zhu, B.-K. Lee, J.D. Ocon, E.S. Chan, In situ Ni-doping during cathodic electrodeposition of hematite for excellent photoelectrochemical performance of nanostructured nickel oxide-hematite p-n junction photoanode, Applied Surface Science, 392 (2017) 144-152.

[22] A.G. Tamirat, J. Rick, A.A. Dubale, W.-N. Su, B.-J. Hwang, Using hematite for photoelectrochemical water splitting: a review of current progress and challenges, Nanoscale Horiz., 1 (2016) 243-267.

[23] E. Courtin, G. Baldinozzi, M.T. Sougrati, L. Stievano, C. Sanchez, C. Laberty-Robert, New Fe2TiO5-based nanoheterostructured mesoporous photoanodes with improved visible light photoresponses, Journal of Materials Chemistry A, 2 (2014) 6567-6577.

[24] S. Shen, Toward efficient solar water splitting over hematite photoelectrodes, Journal of Materials Research, 29 (2013) 29-46.

[25] S.D. Tilley, M. Cornuz, K. Sivula, M. Grätzel, Light-induced water splitting with hematite: improved nanostructure and iridium oxide catalysis, Angewandte Chemie International Edition, 49 (2010) 6405-6408.

[26] J. Li, F. Meng, S. Suri, W. Ding, F. Huang, N. Wu, Photoelectrochemical performance enhanced by a nickel oxide–hematite p–n junction photoanode, Chemical Communications, 48 (2012) 8213-8215.

[27] P.S. Bassi, S.Y. Chiam, Gurudayal, J. Barber, L.H. Wong, Hydrothermal Grown Nanoporous Iron Based Titanate, Fe2TiO5 for Light Driven Water Splitting, ACS Applied Materials & Interfaces, 6 (2014) 22490-22495.

[28] M.V. Nikolić, D. Sekulić, N. Nikolić, M. Slankamenac, O. Aleksić, H. Danninger, E. Halwax, V. Pavlović, P. Nikolić, Structural and electrical properties of Ti doped α-Fe2O3, Science of Sintering, 45 (2013) 281-292.

[29] J. Deng, X. Lv, J. Liu, H. Zhang, K. Nie, C. Hong, J. Wang, X. Sun, J. Zhong, S.-T. Lee, Thin-Layer Fe2TiO5 on Hematite for Efficient Solar Water Oxidation, ACS Nano, 9 (2015) 5348-5356.

[30] P.S. Bassi, R.P. Antony, P.P. Boix, Y. Fang, J. Barber, L.H. Wong, Crystalline Fe2O3/Fe2TiO5 heterojunction nanorods with efficient charge separation and hole injection as photoanode for solar water oxidation, Nano Energy, 22 (2016) 310-318.

[31] S. Chen, Q.Y. Zeng, J. Bai, J.H. Li, L.S. Li, L.G. Xia, B.X. Zhou, Preparation of hematite with an ultrathin iron titanate layer via an in situ reaction and its stable, long-lived, and excellent photoelectrochemical performance, Appl. Catal. B: Environ., 218 (2017) 690-699.

[32] M. Alexander, K. Ilina, F. Alena, F.-R. Dina, B. Thomas, S. Christina, Dual absorber Fe 2 O 3 /WO 3 host-guest architectures for improved charge generation and transfer in photoelectrochemical applications, Materials Research Express, 4 (2017) 016409.

Chapter 6

Conclusions

6.1 Conclusions

The objectives of this thesis were twofold; firstly, to study the effect of anodization on the surface of hematite photoelectrode under photoelectrochemical water splitting conditions. XRD, SEM, Raman and AFM were used to assess morphology and crystallography of the prepared hematite, before and after exposure to PEC environment conditions. Secondly, to synthesize and test Ti-doped hematite photoanodes for photoelectrochemical water splitting application using cost-effective and straightforward methods. Spin coating and dip coating were used to synthesize the samples. To my knowledge, the two approaches have been scarcely investigated.

Regarding the first objective, nanostructured hematite thin films were prepared by dip coating and their surface structural properties and morphology characterized before and after exposure to PEC environment conditions, by XRD, FESEM and AFM. The thin films were exposed to constant anodic potentials of 500 and 700 mV vs the Ag/AgCl reference electrode in a PEC cell for 60s. Hematite is known for its excellent stability against photo-corrosion. However, this study indicates that the surface of hematite photoanode in contact with alkaline electrolyte under PEC conditions may be affected in a way that the surface undergoes modifications. Microscopic surface electron scanning revealed an enhanced hematite surface as the surface underwent re-organization and grain growth under PEC conditions, which indirectly improved optical absorption properties of the electrode. XRD diffractometry revealed an increase of ~ 24 % in the average crystallite size upon exposure to PEC conditions (with both anodic potentials) for just 60 s. However, no clear

correlation was found between the increase in crystallite size and applied anodic potential. FESEM and AFM analyses confirmed XRD data, revealing a noticeable increase of ~ 28 % in average particle size at the hematite surface upon anodization, of which scaled with exposure time. Moreover, the surface smoothened as the density of surface imperfections and the surface roughness decreased. It was also found that longer exposure time led to a continuous increase in particle size. The particle size increased from ~ 57 nm for the film in the pristine state to ~ 88 nm and ~ 149 nm after samples were respectively exposed to PEC environment for 1 min (shorter time) and 900 min (longer time). The UV-vis spectrometry revealed enhanced optical absorption upon doping as compared to pristine hematite. The absorption band slightly shifted to longer wavelengths, suggesting narrowing of the bandgap as the particle size increased.

Although the surface enhancement upon anodization may be beneficial in improving the optical absorption and reduction of charge recombination through reduced grain boundaries, excessive increase in particle size and probably the film thickness could simultaneously lead to increased recombination losses and hence poor photoelectrochemical effects. As the particle size increases, the minority carrier diffusion distances also increases and consequently the photogenerated electron-hole pairs may be lost through recombination. Whether this depends on the preparation method remains under investigation.

The second important achievement of this study is the remarkable performance of spin-coated Ti-doped hematite photoanodes. Ti doping in hematite is well established by now. However, since the results show dependence on the preparative procedure, optimization of techniques continues. Ti-doped hematite films prepared by dip coating showed a good photocurrent of ~ 0.72 mA/cm^2, which is 2 orders of magnitude higher than the pristine film (~ 0.3 mA/cm^2). Although it is not beneficial to compare results of the samples synthesized with different methods due to the

existence of other accentuating or compensating defects [1], it is evident that spin coating offers interesting results for Ti-doped hematite PEC performance. A significant photocurrent of ~ 1.2 mA/cm^2 at 1.23 V vs RHE was obtained with 0.5 at% Ti, which rose to 1.84 mA/cm^2 in highly doped (15 at% Ti) films. This is a significant performance compared to the pristine film (~ 0.013 mA/cm^2) and values obtained with other different strategies in literature. Furthermore, the photocurrent onset potential was shifted to lower applied potentials by > 400 mV at 0.5 at%, which dropped further by an additional 100 mV to 0.995 V vs RHE with 15 at% Ti. The enhancement in PEC performance was attributed to improved conductivity and hence successful reduction of charge recombination in hematite as a result of Ti doping. The XRD analysis revealed formation of a stable titanate oxide phase, pseudobrookite, at higher Ti doping levels which enhanced charge transport and surface kinetics in hematite. Despite the low performance of the pure hematite, the results revealed the potential of spin coating to promote solar oxidation at doped hematite photoanodes, not only for Ti elements but also with other elements. No doubt optimization of the electrode thickness and Ti dopant concentration level would allow exploration of this method in achieving efficient hematite-based electrodes for PEC water splitting systems at low cost.

References

[1] S. Chatman, C.I. Pearce, R.K. M., Charge Transport at Ti-Doped Hematite (001)-Aqueous Interfaces, Chemistry of Materials, 27 (2015) 1665−1673.

6.2 Future work

- Investigation of the effect of anodization-induced surface modifications on microstructural properties at the hematite surface, on the photocurrent production and long term stability of the hematite photoanodes

- While the methods of preparation, doping level and growth conditions vary, there is a common agreement that Ti enhances the performance of hematite photoelectrodes. However, the cause of the improvement remains unclear. Thus part of future work include;
    - ✓ Modification of the existing calculated electronic structure to include theoretical assignments of experimental electronic and vibrational states based on symmetry aspects and wave vector selection rules, taking into consideration the effect of and spin-orbit interaction at high symmetry points to establish effects of Ti doping on the electronic transitions in the band structure.
    - ✓ Lack of theoretical assignments on reported EBS makes it difficult for experimental observations to explain optical electron transfer. An electron can be scattered and trapped at band intervalleys at the centre or edges of the Brillouin zone thereby decreasing number of electrons available for solar PEC water oxidation.

Publication list

1. **Kelebogile Maabong**, Augusto G. J. Machatine, Benard Mwankenwa, Rita Toth, Artur Braun, Bora Debajeet, Mmantsae Diale “Nanostructured hematite thin films for photoelectrochemical water splitting”, *Physica B: Condensed Matter,* Vol.535, (2018), 67-71.

2. Alexander Paradzah, **Kelebogile Maabong**, Mmantsae Diale. Tjaart.Kruger "Use of interfacial layers to prolong holes lifetimes in hematite probed by ultrafast transient absorption spectroscopy," *Physica B: Condensed Matter*, Vol.535, (2018), 138-142

3. Artur Braun, **Kelebogile Maabong,** Mmantsae M. Diale, and Rita Toth, "Hydrogen production with holes: what we learn from operando studies", SPIE Newsroom, Available online: DOI: 10.1117/2.1201704.006793

4. **Kelebogile Maabong**, Augusto G. Machatine, Yelin Hu, Artur Braun, Mmantsae Diale "Influence of anodization time on surface modification on hematite photoanode upon anodization", J. Mater. Res., (2016), pp.1-8.

5. **Kelebogile Maabong**, Augusto G. Machatine, Yelin Hu, Artur Braun, Fred J. Nambala, Mmantsae Diale, "Morphology, structural and optical properties of iron oxide thin film photoanodes in photoelectrochemical cell: Effect of electrochemical oxidation", *Physica B: Condensed Matter,* Vol.480, (2016), 91-94.